Development of highly accurate density functionals for H2 dissociation on transition metals

Smeets, E.W.F.

5 Designing new SRP density functionals including non-local vdW-DF2 correlation for H_2 + Cu(111) and their transferability to H_2 + Ag(111), Au(111) and Pt(111)

This Chapter is based on:

Smeets, E. W. F.; Kroes, G.-J. Designing new SRP density functionals including non-local vdW-DF2 correlation for H_2 + Cu(111) and their transferability to H_2 + Ag(111), Au(111) and Pt(111). *Phys. Chem. Chem. Phys.* **2021**, *23*, 7875–7901

Abstract

Specific reaction parameter density functionals (SRP-DFs) that can describe molecular beam sticking experiments of hydrogen (H_2) on cold transition metal surfaces with chemical accuracy have so far been shown to be only transferable among different facets of the same metal, but not among different metals. We design new SRP-DFs that include non-local vdW-DF2 correlation for the H_2 + Cu(111) system, and evaluate their transferability to the highly activated H_2 + Ag(111) and H_2 + Au(111) systems and the non-activated H_2 + Pt(111) system. We design our functionals for the H_2 + Cu(111) system since it is the best studied system both theoretically and experimentally. Here we demonstrate that a SRP-DF fitted to reproduce molecular beam sticking experiments for H_2 + Cu(111) with chemical accuracy can also describe such experiments for H_2 + Pt(111) with chemical accuracy, and vice versa. Chemically accurate

functionals have been obtained that perform very well with respect to reported Van der Waals well geometries, and which improve the description of the metal over current generalized gradient approximation (GGA) based SRP-DFs. From a systematic comparison of our new SRP-DFs that include non-local correlation with previously developed SRP-DFs, for both activated and non-activated systems, we identify non-local correlation as a key ingredient in the construction of transferable SRP-DFs for H_2 interacting with transition metals. Our results are in excellent agreement with experiment when accurately measured observables are available. It is however clear from our analysis that, except for the H_2 + Cu(111) system, there is a need for more, more varied, and more accurately described experiments in order to further improve the design of SRP-DFs. Additionally, we confirm that, when including non-local correlation, the sticking of H_2 on Cu(111) is still well described quasi-classically.

5.1 Introduction

Hydrogen (H_2) dissociation on various noble transition metal surfaces is an example of an intensely studied activated elementary surface reaction within surface science. Chemically accurate computation of rate-controlling states is essential in order to accurately describe the complex overall processes that take place during heterogeneous catalysis under real world conditions[2–6]. Industrially H_2 dissociation is an important step in the production of methanol from CO_2 over a $Cu/ZnO/Al_2O_3$ catalyst[7–9]. Additionally H_2 dissociation is an important process in the production of syngas and ammonia[5]. Increasing the predictive power of theoretical models of heterogeneous catalysis potentially has an important financial impact on the chemical industry[10].

An important step to increasing the predictive power of theoretical models is to create density functionals (DFs) that are chemically accurate for specific systems[2,11–14], i.e. DFs that can describe reaction barrier heights to within 1 kcal/mol[6]. A next step is to investigate what ingredients of a DF that is chemically accurate for one system might make it transferable to another system without loss of accuracy. Presently, specific reaction parameter (SRP) density functional theory (DFT) is the only method that can describe the interaction of H_2 with metal surfaces with demonstrated chemical accuracy, while simultaneously being computationally cheap enough to make large comparative studies feasible. Therefore the design of accurate DFs is highly important to the field. The availability of transferable specific reaction parameter density functionals (SRP-DFs) has the potential to greatly speed up theoretical heterogeneous catalysis research. It does so by avoiding the need to design a new DF for each system of interest. The availability of transferable SRP-DFs would

greatly improve the predictive power of theory for systems for which only sparse experimental results have been published.

The fitting of SRP-DFs is meticulous work and presently[15] requires experimental data as reference data[2,11–14,16]. Transferability of a DF among systems in which one specific molecule interacts with surfaces of different metals has so far only been reported for the DF designed for CH_4 dissociation on Ni(111)[14], which could also describe the dissociation of CH_4 on Pt(111) with chemical accuracy[17], where Ni and Pt belong to the same group. So far, for SRP-DFs fitted to reproduce molecular beam adsorption experiments for H_2 interacting with transition metals transferability was shown among systems in which H_2 interacts with different faces of the same metal[18,19], but not among systems where the interaction is with surfaces of different metals[13,16,20,21].

The transferability of the SRP-DF that was fitted for the CH_4 + Ni(111) system to the CH_4 + Pt(111) system suggests that non-local correlation is an important ingredient for a transferable DF, as this SRP-DF contains non-local correlation. For this reason here we investigate the design of new SRP-DFs that include non-local correlation for H_2 + transition metal systems. In this work we present two new SRP-DFs featuring GGA exchange but using non-local correlation. These DFs were fitted to experiments on the H_2 + Cu(111) system, since theoretically[11,13,22–45] and experimentally[46–62] this is the best studied system. For this system we can have the most confidence that discrepancies between theory and experiment can be attributed to either shortcomings in DF design or the limitations of using the Born-Oppenheimer static surface (BOSS) model. It is well known that the BOSS model works well for activated H_2 dissociation on cold metals[24,28–30,63]. Additionally we evaluate the performance of a SRP-DF that was fitted to the H_2 + Pt(111) system[12] for the H_2 + Cu(111) system.

In undertaking this study we have two aims. The first is to identify features of the newly constructed SRP-DFs that increase their transferability to other systems. Since we use the BOSS model, a direct assessment of the quality of a given DF is really only possible for molecular beam sticking experiments on reasonably cold metal surfaces. Apart from the H_2 + Cu(111) system we will consider such experiments for the the H_2 + Pt(111) system[64,65] and the H_2 + Ag(111) system[55]. For the latter two systems there exists some uncertainty about the validity of the molecular beam parameters describing the experiments[20,66]. We however feel that, although there are some uncertainties in the parameters describing the experiments, nevertheless valuable insights on transferability can be derived by analysing the predicted reactivity of the SRP-DFs considered here.

Our second aim is to analyse the limits of our dynamical model to the extent

that this is possible. We hope that a detailed analysis of the H_2 + Cu(111) system's large body of experimental work[46–62] will indicate how to proceed with improving the theoretical description of this system. To this end we will analyse both associative desorption experiments[48,52] and dissociative chemisorption experiments[46,47]. Naturally, our primary motive is to achieve chemical accuracy. We have also carried out a full quantum mechanical molecular beam simulation by carrying out a large number of fully initial-state resolved quantum dynamical (QD)[67,68] calculations for the H_2 + Cu(111) system. This is important because the inclusion of a Van der Waals well in the PES might lead to discrepancies between quasi-classical trajectory (QCT)[69] and QD results compared to the good agreement that was obtained for these two methods for the H_2 + Cu(211) system[37] using the SRP48 DF[11,63], which does not employ non-local correlation.

For the H_2 + Cu(111) system it is known that the effect of surface motion cannot readily be ignored for specific observables at high surface temperature[63] (T_s). Analysing associative desorption and dissociative chemisorption experiments as linked through detailed balance[70], might allow us to disentangle the effects of surface motion and the non-adiabatic contributions of electron-hole pair (ehp) excitations, a methodology that was suggested by results of Shuai et al.[71] for the H_2 + Au(111) system. If detailed balance is applicable then an analysis of both associative desorption and dissociative chemisorption experiments should yield the same result. A detailed analysis might therefore allow us to identify which dynamical effects not included in the BOSS model may have to be included in future work. Here we will make a direct comparison to experimental effective barrier ($E_0(\nu, J)$) parameters[48]. Even though a complementary molecular beam sticking experiment is not available with the associative desorption experiment of Shuai et al.[71] on H_2 + Au(111), we extend our analysis also to this system. We note that it is also possible to simulate associative desorption directly by running trajectories starting around the transition state using Metropolis sampling of the initial conditions[72–76], and that this has also been done for H_2 and D_2 desorbing from Cu(111). However, the calculations published so far do have limitations. The early work[73,74] used a PES that is an approximate fit[40] to unconverged DFT calculations[41] using the PW91 DF[77], and the statistical accuracy of the results of the later work[76] was limited by the number of ab initio molecular dynamics (AIMD) trajectories that could be run. However, an interesting aspect of the later work[76] is that the effects of surface atom motion and electron-hole pair excitation could also be investigated.

Furthermore we will treat vibrationally and rotationally inelastic scattering for the H_2 + Cu(111) system, since the opinion has been voiced that these properties might be extra sensitive to the Van der Waals well[25], which is present

in potential energy surfaces (PESs) computed here with the use of non-local correlation.

For the H_2 + Ag(111) system the only molecular beam dissociative chemisorption experiments we are aware of are those of Hodgson and coworkers[55]. We will also make a comparison to initial-state resolved associative desorption experiments for this system[78,79], as was recently done by Jiang et al.[80] using quantum dynamics calculations on a permutation invariant polynomial (PIP) neural network potential[81] and in work done in our group[13,20]. Earlier experimental work on the H_2 + Ag(111) system suggested that H_2 prefers to physisorb on silver surfaces[82–84], and that the dissociation of H_2 on silver is endothermic[85], exhibiting a relatively low barrier for associative desorption of H_2[85–87]. For this reason some earlier experimental studies have focused on scattering at low translational energies of H_2 from Ag(111)[88–91] and Ag(110)[92]. Recent theoretical studies that addressed the effects of electron-hole pair excitation have shown very interesting effects at low translational energies with respect to inelastic scattering and dynamical steering[93–95]. The non-adiabatic energy loss during the dynamics was however shown to be small[95]. This is in agreement with work on H_2 + Cu(111), which also showed little effect of electron-hole pair excitation on sticking[23,96]. Therefore we presume the BOSS model to be accurate enough for our first aim, which is to identify the features of SRP functionals that contribute to their transferability.

Our DFT calculations using van der Waals correlation functionals[97,98] also yield results regarding the geometry and the depth of the van der Waals wells for the systems investigated, and we will compare these results to the experimental results for the systems investigated here. In many cases the experimental results come from an analysis of experiments on selective adsorption[60,62,90,91,99–105]. In these experiments, an increase or a dip is observed in a peak for a diffractive (corrugation mediated selective adsorption, CMSA[106,107]) or a rotational (rotationally mediated selective adsorption, RMSA[99]) transition if the translational energy goes through a value that coincides with the energy between two parallel translational or hindered rotational metastable states, respectively. In the transient state, the H_2 molecule is trapped in the Van der Waals well close to the surface[101,104]. Information about the resonance energies that are present can be used to reconstruct the shape of the potential, and thus the Van der Waals well geometries and well depths. The H_2 -(111) metal-surface systems investigated here exhibit little corrugation. For this reason experiments using RMSA of HD, in which rotational excitation is used to probe the bound levels of the gas-surface potential, have been particularly important for gathering information concerning van der Waals interactions in these systems. The off-center position of the center of mass of HD results in very pronounced resonances when

using the RMSA technique[62,99–102]. Experimentalists have also been able to carry out RMSA measurements using H_2 or D_2 instead of HD[90,91,103]. Van der Waals well depths can also be obtained from the temperature dependence of the Debye-Waller attenuation of peaks for (rotationally) inelastic diffraction[108,109], from potential inversion using calculations on (rotationally inelastic) diffractive scattering using the eikonal approximation[108], and from potential inversion using measurements on phonon-assisted RMSA (also called rotationally mediated focused inelastic resonances, RMFIR[110]). For all systems investigated here, studies using experiments to analyze the Van der Waals interaction have been performed, i.e., for H_2 + Cu(111)[60,62], H_2 + Ag(111)[90,91,102], H_2 + Au(111)[62], and H_2 + Pt(111)[99–101,111].

5.2 Methodology

5.2.1 Coordinate system

All calculations in this work are carried out using the BOSS model[11]. This means that the atoms of the metal slab are fixed to their ideal positions, and that we only take into account the six molecular degrees of freedom (DOF) of the impinging H_2 (D_2) molecule (see figure 5.1a). Three of the DOFs taken into account are the centre of mass (COM) coordinates X, Y and Z, where (X, Y) describes the lateral position of the molecule and Z describes the molecule-surface distance. The other DOFs are the H_2 bond length r, the polar orientation angle with respect to the surface normal θ and the azimuthal angle ϕ. The geometry of the (111) face of an fcc metal together with its high symmetry sites is shown in relation to the coordinate system used in figure 5.1b.

5.2.2 SRP DFT

We use periodic DFT calculations to construct PESs, testing DFs at the GGA, the meta-GGA (mGGA), and GGA + non-local correlation level, where in this Chapter non-local correlation refers to either vdW-DF1 non-local correlation[97] or vdW-DF2 non-local correlation[98] (see the types of DF defined in table 5.1). In many cases we test a DF that is a SRP-DF for at least one of the four systems considered. In the present context a SRP-DF is constructed by taking a weighted average of a DF that overestimates the sticking probability, and one DF that underestimates the sticking probability for the system of interest[11]. More specifically, the mixing often occurs for the exchange part of the DF, as was done for many of the previously developed SRP-DFs[12,14,17,27].

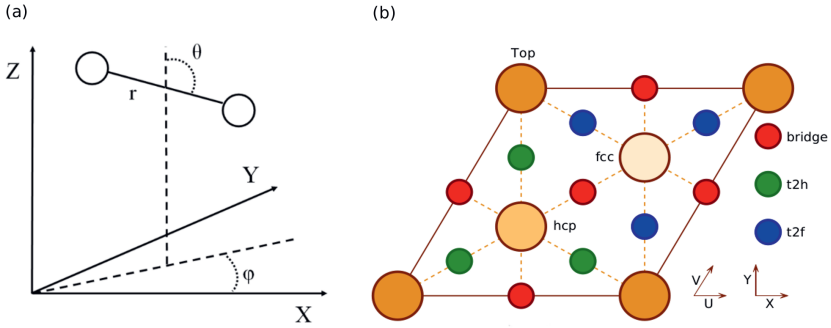

FIGURE 5.1: The COM coordinate system used for the description of the H_2 (D_2) molecule (a). The unit cell of a (111) face of a fcc metal together with the high symmetry sites as well as the relationship with the coordinate system chosen for H_2 (D_2) relative to the (111) surface (b). The origin of the COM coordinate system $(X, Y, Z) = (0, 0, 0)$ is at an atom in the top surface layer (a top site). We define the polar angle and azimuth such that $(\theta = 90°, \phi = 0°)$ corresponds to molecules parallel to the surface pointing along the X (or equivalent U) direction. The hcp and fcc hollow sites correspond to metal atoms in the second and third layer, respectively.

The SRP-DFs developed in this work are all DFs in which the exchange part is taken at the GGA level, and the exchange correlation functional takes the following form:

$$E_{XC}^{SRP}(\rho, \nabla\rho) = \underbrace{\alpha E_X^1(\rho, \nabla\rho) + (1-\alpha)E_X^2(\rho, \nabla\rho)}_{\text{mixed exchange}} + \underbrace{E_C^{local}(\rho)}_{\text{LDA correlation}} + \underbrace{E_C^{non-local}(\rho)}_{\text{Van der Waals}} \tag{5.1}$$

Here α is the SRP mixing parameter, ρ is the three dimensional electron density and $\nabla\rho$ is the gradient of the electron density. $E_X^1(\rho, \nabla\rho)$ and $E_X^2(\rho, \nabla\rho)$ are the two DFs that are to be mixed into the exchange part of the SRP-DF. The non-local correlation part here can correspond to the non-local correlation used in the vdW-DF1 or vdW-DF2 DFs[97,98]. The DFs used in this work (i.e., the B86SRP68-DF2 and SRPsol63-DF2 DFs, and the other DFs considered in this work) are shown in table 5.1. Table 5.1 also shows the type of each DF and the exchange and correlation components contained in each function (see Eq. 5.1).

Name	type	exchange	correlation
B86SRP68-DF2	vdW-DF	0.68 B86r[112] + 0.32 RPBE[113]	vdW-DF2[98]
MS-B86bl[13]	mGGA	MS-B86bl[13]	revTPSS[114]
MS-PBEl[13]	mGGA	MS-PBEl[13]	revTPSS[114]
optPBE-DF1[115]	vdW-DF	optPBE[115]	vdW-DF1[97]
PBE[116]	GGA	PBE[116]	PBE[116]
PBEα57-DF2[12]	vdW-DF	PBE$\alpha = 0.57$[117]	vdW-DF2[98]
PBEsol[118]	GGA	PBEsol[118]	PBE[116]
RPBE[113]	GGA	RPBE[113]	PBE[116]
SRP48[63]	GGA	0.52 PBE[116] + 0.48 RPBE[113]	PBE[118]
SRPsol63-DF2	vdW-DF	0.63 PBEsol[118] + 0.37 RPBE[113]	vdW-DF2[98]
vdW-DF1[97]	vdW-DF	revPBE[119]	vdW-DF1[97]
vdW-DF2[98]	vdW-DF	rPW86[120]	vdW-DF2[98]

TABLE 5.1: The exchange-correlation DFs used in this work are presented in alphabetical order. Also shown is the type of each functional as well as the constituent exchange and correlation parts. By the type "vdW-DF" we mean that GGA exchange is combined with vdW-DF1[97] of vdW-DF2[98] correlation.

5.2.3 Construction of the PESs

A continuous representation of the PESs is obtained by the interpolation of DFT results calculated on a grid using the corrugation reducing procedure (CRP)[121] (see also section 2.2 of Chapter 2). The method we use is analogous to that used by Wijzenbroek et al.[42], but we used denser grids to represent the full six dimensional molecule-surface interaction potential and the three dimensional atom-surface interaction potential to further increase the accuracy of the resulting CRP[121] PESs with respect to the underlying DFT calculations. Details are presented in appendix 5.A.

5.2.4 Quasi-classical dynamics

The QCT calculations presented in this work are carried out on six dimensional PESs and assume quasi-classical initial conditions[69]. This means that we take into account the quantum mechanical energies of the impinging H_2 and D_2 molecules in their initial rovibrational states. The method used is described more fully in ref.[122] and section 2.3.1 of Chapter 2. The equations of motion are integrated using the method of Stoer et al.[123].

When simulating a molecular beam experiment 200,000 trajectories are propagated per energy point, and when calculating initial-state resolved reaction probabilities 50,000 trajectories are propagated per energy point. All trajectories start in the gas phase, at $Z_{\text{gas}} = 8$ Å. For all QCT calculations we use a minimum time step of $dt = 0.001$ fs. Trajectories are assumed to result in reaction if r becomes bigger then some critical value r_c (2.2Å) and in scattering if Z becomes bigger then Z_{gas} which is also the starting point of all trajectories.

5.2.5 Quantum dynamics

Six dimensional quantum dynamics (QD) calculations are performed by solving the time-dependent Schrödinger equation,

$$i\hbar\frac{d\Psi(\vec{Q};t)}{dt} = \hat{H}\Psi(\vec{Q};t), \tag{5.2}$$

using the time-dependent wave packet (TDWP) method[124,125] with our in-house computer package[67,68]. Here, $\Psi(\vec{Q};t)$ denotes the nuclear wave function of H_2 at time t with $\vec{Q}$ being the position vector. Furthermore we employ the following Hamiltonian in order to take into account the six degrees of freedom of H_2:

$$\hat{H} = -\frac{\hbar^2}{2M}\nabla^2 - \frac{\hbar^2}{2\mu}\frac{\partial^2}{\partial r^2} + \frac{1}{2\mu r^2}\hat{J}^2(\theta,\phi) + V(\vec{Q}). \tag{5.3}$$

Here, M and μ are the mass and reduced mass of H_2, $\hat{J}^2(\theta,\phi)$ is the angular momentum operator and $V(\vec{Q})$ is the six dimensional PES. The scattered wave packet is analysed using the scattering matrix formalism[126], yielding fully initial-state resolved S-matrix elements for vibrationally, rotationally, and diffractionally inelastic scattering. From the S-matrix elements the corresponding state-to-state probabilities $P_{\nu J m_J \rightarrow \nu' J' m'_J nm}(E)$ for scattering at the incident energy E can be obtained[67,68]. Subsequently the sticking probability can be computed[67,68] by subtracting the sum of the scattering probabilities from one.

Further information on how we construct the initial wave packet can be found in section 2.3.2 of Chapter 2. Table 5.2 presents parameters describing all the initial wave packets used, and table 5.3 shows the rovibrational states taken into account in the molecular beam simulations of sticking with the QCT and QD methods.

5.2.6 Computation of observables

Simulating molecular beam sticking.

In order to compute molecular beam sticking probabilities the translational energy and rovibrational state distributions need to be taken into account according to the nozzle temperature, T_n. The sticking probability S_0 is computed using

$$S_0(< E >) = \sum_{\nu,J}\int P(v,\nu,J,T_n)P_{\mathrm{deg}}(E,\nu,J)dE. \tag{5.4}$$

TABLE 5.2: Input parameters for the 6D quantum simulations on the reactive scattering of H_2 on Cu(111). All wave packets were propagated until the remaining norm was less then one percent.

	H_2 + Cu(111)						
	($\nu = 1$,	0.15 eV - 0.55 eV			0.5 eV - 1.4 eV		
	$J = 0$, $m_J = 0$)	$\nu = 0$ $J \in [0, 7]$	$\nu = 0$ $J \in [8, 11]$	$\nu = 1$ $J \in [0, 7]$	$\nu = 0$ $J \in [0, 7]$	$\nu = 0$ $J \in [8, 11]$	$\nu = 1$ $J \in [0, 7]$
Z_{start} (Bohr)	-1.0	-1.0	-1.0	-1.0	-1.0	-1.0	-1.0
$N_{Z_{spec}}$	280	252	252	252	224	224	224
N_Z	240	198	198	198	192	192	192
ΔZ (Bohr)	0.1	0.1	0.1	0.1	0.1	0.1	0.1
R_{start} (Bohr)	0.8	0.8	0.8	0.8	0.8	0.8	0.8
N_R	64	56	56	56	48	48	48
ΔR (Bohr)	0.15	0.15	0.15	0.15	0.15	0.15	0.15
N_X	20	20	20	20	20	20	20
N_Y	20	20	20	20	20	20	20
$J_{\max}$	36	26 / 25	32 / 31	36 / 35	36 / 35	42 / 41	40 / 39
$m_{J\max}$	28	26 / 25	32 / 31	28 / 27	28 / 27	40 / 39	32 / 31
Complex absorbing potentials							
Z^{CAP} start [a_0]	15.2	15.2	15.2	15.2	15.2	15.2	15.2
Z^{CAP} end [a_0]	22.90	18.7	18.7	18.7	18.1	18.1	18.1
Z^{CAP} Optimum [eV]	0.03	0.1	0.1	0.1	0.3	0.3	0.3
Z^{CAP}_{spec} start [a_0]	19.8	19.8	19.8	19.8	18.8	18.8	18.8
Z^{CAP}_{spec} end [a_0]	26.90	24.1	24.1	24.1	21.3	21.3	21.3
Z^{CAP}_{spec} Optimum [eV]	0.05	0.08	0.08	0.08	0.25	0.25	0.25
R^{CAP} start [a_0]	4.55	4.55	4.55	4.55	4.55	4.55	4.55
R^{CAP} end [a_0]	10.25	9.05	9.05	9.05	7.85	7.85	7.85
R^{CAP} optimum [eV]	0.1	0.1	0.1	0.1	0.25	0.25	0.25
Propagation							
Δt [$\hbar/E_h$]	2	2	2	2	2	2	2
t_f [$\hbar/E_h$]	45000	20000	20000	20000	13000	13000	13000
Initial wave packet							
E_{min} [eV]	0.055	0.15	0.15	0.15	0.5	0.5	0.5
E_{max} [eV]	0.45	0.55	0.55	0.55	1.4	1.4	1.4
Z_0 [a_0]	17.50	17.40	17.40	17.40	16.8	16.8	16.8

	$(\nu = 0)J_{\max}$	$(\nu = 1)J_{\max}$	$(\nu = 2)J_{\max}$	$(\nu = 3)J_{\max}$	$(\nu = 4)J_{\max}$
QCT	30	30	30	30	30
QD	11	7	-	-	-

TABLE 5.3: Rovibrational states taken into account, according to their Boltzmann weight, in molecular beam simulations for the QCT and QD methods for all H_2 (D_2, only QCT) + metal systems.

Here, $< E >$ is the average translational energy. The probability for a molecule present in the beam to be in a rovibrational state described by the vibrational quantum number ν and the angular momentum quantum number J and to have a velocity between v and $v + dv$ is denoted by:

$$P(v, \nu, J, T_n)dv = P_{flux}(v; T_n)dv \times P_{int}(\nu, J, T_n). \tag{5.5}$$

The flux-weighted velocity distribution P_{flux} is a function of T_n and is determined by the width parameter α and the stream velocity v_0 according to[45]

$$P_{flux}(v; T_n)dv = Cv^3 e^{-(v-v_0)^2/\alpha^2} dv \tag{5.6}$$

with C being a normalization constant. Through Eq. 5.4 and 5.5 the reactivity of each rovibrational state is weighted according to its Boltzmann weight as follows:

$$P_{int}(\nu, J, T_n) = \frac{g_N f(\nu, J, T_n)}{\sum_{v', J' \equiv J(mod\ 2)} f(\nu', J', T_n)}, \tag{5.7}$$

with

$$f(\nu, J, T_n) = (2J + 1) \times e^{(-(E_{\nu,0} - E_{0,0})/k_B T_{vib})} \times e^{(-(E_{\nu,J} - E_{\nu,0})/k_B T_{rot})}. \tag{5.8}$$

Here, k_B is the Boltzmann constant and $E_{\nu,J}$ is the energy of the quantum state characterized by ν and J. The first and second Boltzmann factor describe vibrational and rotational state populations, respectively. Here we take into account the effect of rotational cooling during the supersonic expansion by taking the rotational temperature to be $T_{rot} = 0.8 * T_n$[52], while the vibrational temperature, T_{vib}, is taken to be equal to T_n. The factor g_N in Eq. 5.7 reflects the ortho/para ratio of hydrogen in the beam. For H_2, g_N is 1/4 (3/4) for even (odd) values of J, and for D_2, $g_N = 2/3$ (1/3) for even (odd) values of J.

In the QCT calculations presented in this work the probability distribution $P(v, \nu, J, T_n)$ is randomly sampled as described in ref[122]. All parameters describing molecular beam experiments used for the calculations presented here can be found in table 5.4. The reaction probability is then computed by dividing the number of adsorbed trajectories, N_{ads}, by the total number of calculated trajectories, N, i.e. $P_r = N_{ads}/N$.

We compute initial-state selected but degeneracy averaged reaction probabilities, $P_{\mathrm{deg}}(E, \nu, J)$, as:

$$P_{\mathrm{deg}}(E, \nu, J) = \sum_{m_J=0}^{J} (2 - \delta_{m_J 0}) \frac{P_r(E, \nu, J, m_J)}{2J + 1}, \tag{5.9}$$

where $P_r(E, \nu, J, m_J)$ is the fully initial-state resolved reaction probability, m_J is the magnetic rotational quantum number, and E is the translational energy. For the QD calculations it is not possible to directly sample $P(v, \nu, J, T_n)$. Molecular beam reaction probabilities for the QD method are instead calculated from initial-state resolved reaction probabilities in the same manner as discussed in our Chapter 4.

Comparing to experimental $E_0(\nu, J)$ parameters.

Experimentally, for H_2-metal surface reactions the initial state-selected reaction probabilities are usually obtained[46,48,52,71] from associative desorption measurements using the principle of detailed balance[70]. Experiments on H_2 associatively desorbing from metals typically measure the (unnormalized) state-resolved translational energy distributions of molecules from the surface using resonance-enhanced multi-photon ionization (REMPI)[19,46,52]. These distributions, $P_{\mathrm{des}}(E, \nu, J)$, may be related to the degeneracy averaged initial-state resolved reaction probability, using:

$$P_{\mathrm{des}}(E, \nu, J) \propto E e^{-\frac{E}{k_b T_s}} P_{\mathrm{deg}}(E, \nu, J). \tag{5.10}$$

The extracted reaction probabilities are usually fitted to a sigmoid function, e.g. the function involving the error function:

$$P_{\mathrm{deg}}(E, \nu, J) = \frac{A_{\nu,J}}{2}\left[1 + erf\left(\frac{E - E_0(\nu, J)}{W_{\nu,J}}\right)\right]. \tag{5.11}$$

Here, the $A_{\nu,J}$ values are the saturation values of the extracted degeneracy averaged reaction probabilities, and the effective barrier height ($E_0(\nu, J)$) is the incidence energy at which $P_{\mathrm{deg}}(E, \nu, J)$ first becomes equal to $\frac{1}{2}A_{\nu,J}$. Using Eq. 5.11, $E_0(\nu, J)$ also is the inflexion point of the reaction probability curve if the saturation value $A_{\nu,J}$ corresponds to the absolute saturation value. $W_{\nu,J}$ is a measure of the width of the reaction probability curve.

If the proportionality factor implicit in Eq. 5.10 would also be measured in the experiment (for instance, because the exact state-selective flux would have been measured), it should be possible to directly extract absolute values of the initial-state selected reaction probabilities from the experiment by assuming detailed balance. In this case, the directly extracted $A_{\nu,J}$ value would be the true saturation value of the reaction probability. These values could then be directly compared to computed degeneracy averaged initial-state resolved reaction probabilities (Eq. 5.9).

TABLE 5.4: Molecular beam parameters taken from experiments performed on the H_2 (D_2) + Cu(111) system and the D_2 + Pt(111) system. The parameters v_0, α, T_n represent the stream velocity of the beam, the width of the beam and the nozzle temperature at an average translational incidence energy $\langle E_i \rangle$. Parameters were taken from (the supporting information of) Refs[11,29,46,47,64,66,127,128].

T_n [K]	$\langle E_i \rangle$ [kJ/mol]	v_0 [m/s]	E_0 [eV]	α [m/s]
Seeded molecular H_2 beams, Auerbach and coworkers[46]				
1740	19.9	3923	0.160	1105
1740	28.1	4892	0.250	1105
1740	38.0	5906	0.364	945
2000	18.2	3857	0.155	995
2000	25.1	4625	0.223	1032
2000	44.1	6431	0.432	886
Seeded molecular D_2 beams, Auerbach and coworkers[46]				
2100	35.4	3925	0.322	816
2100	46.4	4595	0.441	782
2100	62.6	5377	0.829	649
2100	69.2	5658	0.860	717
2100	80.1	6132	0.849	830
Pure molecular H_2 beams, Auerbach and coworkers[46]				
1435	31.7	5417	0.307	826
1465	32.0	5446	0.310	830
1740	38.0	5906	0.364	945
1855	40.5	6139	0.394	899
2000	44.1	6431	0.432	886
2100	47.4	6674	0.465	913
2300	49.7	6590	0.454	1351
Pure molecular D_2 beams, Auerbach and coworkers[46]				
1435	32.8	4014	0.336	299
1790	37.8	4196	0.368	614
1670	38.6	4337	0.393	371
1905	41.4	4374	0.399	685
1975	43.0	4461	0.415	687
Pure molecular H_2 beams, Rendulic and coworkers[47]				
1118.07	25.1	3500	0.12794	1996
1331.89	29.9	3555	0.13200	2342
1438.82	32.3	3380	0.11932	2611
1501.19	35.7	3151	0.10371	2819
1581.35	35.5	3219	0.10816	2903
Seeded molecular D_2 beams, Juurlink and coworkers[64]				
473	10.0	2004.6	0.083	528.7
673	9.7	2127.9	0.095	297.9
673	13.9	2256.8	0.106	741.8
973	17.6	2484.9	0.129	881.7
673	24.6	3204.7	0.214	766.3
873	27.5	3302.7	0.228	906.7
873	30.1	3449.1	0.248	955.3
873	30.6	3521.1	0.259	909.4
1223	41.9	4015.0	0.337	1181.0
1223	42.8	4096.5	0.350	1151.1
1503	52.8	4039.3	0.340	1744.7
Seeded molecular D_2 beams, Groot and coworkers[128]				
300	7.5	1932.3	0.078	193.6
500	12.0	2372.5	0.117	295.1
900	21.1	3090.8	0.199	527.4
1300	30.5	3625.4	0.274	765.6
1700	35.0	3818.9	0.304	908.9
1700	43.9	4051.2	0.342	1261.8
1700	45.0	4268.9	0.380	1097.1

In practice, even if the prefactor in Eq. 5.10 is not measured in associative desorption, it is still possible to extract normalized values from a wholly experimental procedure, if measured sticking probabilities are also available. This has been done for H_2 + Cu(111)[48,52] and D_2 + Cu(111)[46,48,63]. In this method, which we call method A1, essentially the sticking probability is described in terms of the initial-state selected probabilities extracted from the associative desorption experiments, thereby obtaining the saturation values describing the latter. Method A1 is described more fully in appendix 5.B.

If no sticking experiments are available, as for the H_2 + Au(111) system also studied here, the experimentalists may chose not to normalize the extracted reaction probabilities in an absolute sense. However, the extracted reaction probabilities may still be normalized relative to one another. This was done in recent experiments on H_2 and D_2 + Au(111), in which $A_{\nu,J}$ was set to one for $(\nu = 0, J = 6)$ H_2 and for $(\nu = 0, J = 0)$ D_2, and the $A_{\nu,J}$ values for different (ν, J) states of H_2 and D_2, respectively, reflected the values of the reaction probabilities relative to these reference states[71]. We will call this method A2, where the A in A2 emphasizes that this method is also wholly experimental.

If no measured sticking probabilities are available for the system of interest, one may still choose to normalize reaction probabilities extracted from associative desorption experiments, but now with reference to theory[48,71]. We label such methods with "B" to emphasize that the normalization is done with reference to theory. In the methods we are aware of, the experimentalists define a translational energy $E_{\max}(\nu, J)$, which is the maximum translational energy for which the not yet normalized value can still be accurately extracted using Eq. 5.10[48,71]. At higher E this becomes difficult because the desorption flux becomes small due to the exponential factor in Eq. 5.10, leading to too much noise in the determined $P_{\deg}(E, \nu, J)$. Parameters can then be described in two ways (methods B1 and B2). Briefly, in method B1 the saturation parameters are determined by setting them equal to the theoretical reaction probability computed for $E = E_{\max}(\nu, J)$. The $E_{1/2}(\nu, J)$ parameters is then determined as the energy at which the computed reaction probability equals half this computed reaction probability. Method B2 aims to improve upon this. Method B1 was previously followed in experimental papers to enable comparison with theory for H_2, D_2 and HD desorbing from Cu surfaces[48], and for H_2 and D_2 desorbing from Au(111)[71]. Further details of methods B1 and B2 are presented in appendix 5.B.

Rotational quadrupole alignment parameters.

The rotational quadrupole alignment parameter, $A_0^{(2)}(E,\nu,J)$, is computed from initial-state resolved reaction probabilities as follows:[129]

$$A_0^{(2)}(E,\nu,J) = \frac{\sum_{m_J=0}^{J}(2-\delta_{m_J,0})P_r(E,\nu,J,m_J)\left(\frac{3m_J^2}{J(J+1)}-1\right)}{\sum_{m_J=0}^{J}(2-\delta_{m_J,0})P_r(E,\nu,J,m_J)}. \quad (5.12)$$

The rotational quadrupole alignment parameter is a measure of the dependence of the reaction on the alignment of H_2 relative to the surface.

Rovibrational state populations of H_2 and D_2 desorbing from Au(111).

State distributions of desorbing molecules are calculated in the following manner:[71]

$$N(\nu,J) = \int_0^{E_{\max(\nu,J)}} P_{int}(\nu,J,T_S)\sqrt{E}\, e^{(-\frac{E}{k_B T_S})}\, P_{\deg}(E,\nu,J)dE. \quad (5.13)$$

Here T_S is the surface temperature, and $E_{\max}(\nu,J)$ is the maximum kinetic energy sensitivity of the experiment[71], which is plotted as a function of J in figure 5.B.2. To make a comparison between theory and experiment possible, the experimental $P_{\deg}(E,\nu,J)$ are replaced by the error function expressions of ref.[71]. In order to make this comparison valid, we only integrate Eq. 5.13 up to $E_{\max}(\nu,J)$. The error function fits derived in ref.[71] are only valid below $E_{\max}(\nu,J)$ and can yield sticking probabilities substantially bigger than one for higher energies. Integration of Eq. 5.13 is done by taking a right Riemann sum with a dE of 0.2 meV. The $N(\nu,J)$ populations are normalized to the total $\nu=0$ population according to:.

$$N(\nu,J) = \frac{N(\nu,J)}{\sum_J N(\nu=0,J)} \quad (5.14)$$

The ratio $\nu=1:\nu=0$ can then calculated as:

$$\nu=1:\nu=0 = \frac{\sum_J N(\nu=1,J)}{\sum_J N(\nu=0,J)} \quad (5.15)$$

The upper limits to J used in Eqs 5.14 and 5.15 are discussed below.

5.2.7 Computational details

All the electronic structure calculations were carried out by performing plane wave periodic DFT calculations using a user modified version of the Vienna Ab Initio Simulation Package[130–133] (VASP). The modification of the computer package concerns an interface to VASP with the LibXC density functional library[134]. The standard VASP projector augmented wave (PAW) potentials[135] and vdW-DF correlation[97,98] as implemented in VASP[136,137] were used for all calculations at the GGA level except for the SRP48 calculations on Pt(111), for which the standard VASP ultrasoft pseudopotentials[138] and PBE correlation[116] were used. Calculations done using a mGGA use mGGA correlation (see table 5.1).

All calculations at the GGA level presented in this work have been carried out using a plane wave cutoff energy of 450 eV together with smearing of 0.2 eV using the Methfessel-Paxton method of order 1. The input parameters for calculations with a mGGA DF can be found in ref.[13] Lattice constants have been calculated using a four atom bulk unit cell and a $28 \times 28 \times 28$ Monckhorst-Pack k-point grid. All metal slabs consist of six layers of which the bottom two layers were fixed at the ideal bulk interlayer distance. Slab relaxation has been carried out using a 1×1 supercell, a $32 \times 32 \times 1$ Γ-centered k-point grid and a vacuum distance of 16 Å. PES calculations have been carried out using a 3×3 supercell, a $11 \times 11 \times 1$ Γ-centered k-point grid and a vacuum distance of 16 Å.

5.3 Results

5.3.1 Electronic structure

Description of the metal.

Table 5.5 shows calculated lattice constants for different DFs, comparing with zero-point energy corrected experimental results[139]. Table 5.6 shows the percentage change of the distance between the top two layers of the metal slab relative to the calculated bulk interlayer distance, also comparing to experimental results[57–59,140–144].

H_2 + metal surface PESs

Barrier heights and geometries for H_2 + Cu(111) for high symmetry geometries are shown in table 5.7. The energetic corrugation ξ, which is the difference

	Cu		Ag		Au		Ni		Pd		Pt			
	Å	%	Å	%	Å	%	Å	%	Å	%	Å	%	UAPE	SAPE
exp.	3.596		4.062		4.062		3.508		3.876		3.913			
SRP48[63]	3.679	2.30	4.207[20]	3.56	4.202[145]	3.44	3.531	0.65	3.985	2.81	3.998	2.17	2.48	2.48
vdW-DF1[97]	3.697	2.80	4.240	4.38	4.245	4.50	3.570	1.76	4.008	3.40	4.032	3.04	3.31	3.31
vdW-DF2[98]	3.742	4.06	4.308	6.05	4.336	6.74	3.607	2.82	4.077	5.18	4.108	4.98	4.97	4.97
B86SRP68-DF2	3.639	1.19	4.150	2.16	4.166	2.56	3.528[21]	0.57	3.944	1.75	3.979	1.68	1.65	1.65
SRPsol63-DF2	3.644	1.33	4.157	2.33	4.171	2.68	3.525	0.48	3.949	1.88	3.983	1.78	1.75	1.75
PBEα57-DF2[12]	3.656	1.66	4.176	2.80	4.198	3.34	3.534[21]	0.74	3.970	2.42	4.016[12]	2.63	2.27	2.27
optPBE-DF1[115]	3.649[42]	1.47	4.179	2.88	4.197	3.32			3.972	2.47	4.001	2.24	2.47	2.47
MS-B86bl[13]	3.583	-0.37	4.087	0.61	4.087	0.61	3.478	-0.86	3.895	0.49	3.908	-0.13	0.51	0.06
PBE[116]	3.632[139]	1.00	4.152[139]	2.21	4.154[139]	2.26	3.518[139]	0.28	3.948[139]	1.85	3.985[139]	1.84	1.57	1.57
PBEsol[118]	3.570[139]	-0.73	4.058[139]	-0.10	4.081[139]	0.46	3.463[139]	-1.29	3.882[139]	0.15	3.932[139]	0.48	0.54	-0.17

TABLE 5.5: Zero-point energy corrected experimental lattice constants[139] in Å and percentage deviations of computed values from the experimental value. The UAPE and the SAPE are the unsigned and signed average percentage differences with the experimental value, respectively.

	Cu	Ag	Au	Ni	Pd	Pt
exp.	-1.0%,[57,59] -0.7%[58]	-2.5%,[140] -0.5%[141]	1.5%[142]	-0.07%[57]	1.3%[143]	1.1%[144]
SRP48[11]	-1.3%[11]	-0.6%[20]	0.6%[145]	-1.0%[21]	0.0%	1.0%
vdW-DF1[97]	-0.2%	0.1%	1.6%	-1.1%	0.7%	1.3%
vdW-DF2[98]	0.0%	0.5%	2.1%	-1.1%	0.8%	1.5%
B86SRP68-DF2	-0.4%	-0.1%	1.3%	-1.1%[21]	0.7%	1.2%
SRPsol63-DF2	-0.4%	-0.2%	1.4%	-1.1%	0.6%	1.0%
PBEα57-DF2[12]	-0.4%	0.0%	1.5%	-0.8%[21]	0.6%	0.8%
optPBE-DF1[115]	-0.8%[42]	-0.2%	1.0%		0.2%	0.8%
MS-B86bl[13]	-1.0%	-0.5%	1.0%		0.3%	1.0%
PBE[116]	-0.3%[146]	-0.2%[146]	1.0%[146]		-0.5%[146]	0.9%[146]
PBEsol[118]	-0.4%[146]	-0.1%[146]	0.8%[146]		0.6%[146]	0.8%[146]

TABLE 5.6: Relaxations of the interlayer distance between the top two layers relative to the bulk interlayer distance in %.

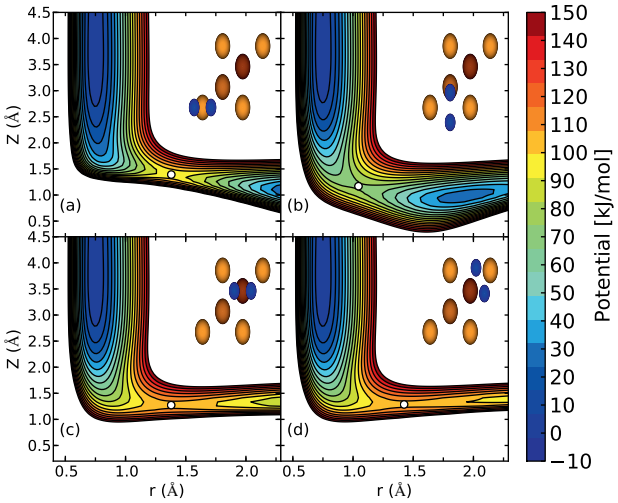

FIGURE 5.2: Elbow plots, i.e. $V(Z, r)$ resulting from the H_2 + Cu(111) PES computed using the B86SRP68-DF2 DF and interpolated using the CRP method for four high symmetry geometries in which the molecular axis is parallel to the surface ($\theta = 90°$) as depicted by the insets for (a) the top site and $\phi = 0°$, (b) the bridge site and $\phi = 90°$, (c) the fcc site and $\phi = 0°$, and (d) the t2f site and $\phi = 120°$. Barrier positions are indicated with white circles.

between the highest and the lowest barrier height, is shown as well. Elbow plots for four geometries are shown in figure 5.2 for the B86SRP68-DF2 SRP-DF.

Barrier heights and positions for H_2 + Ag(111), Au(111) and Pt(111) are shown in tables 5.8, 5.9 and 5.10 respectively. With respect to the H_2 + Pt(111) system the most striking result is that only the PBEα57-DF2[12] and MS-PBEl[13] DFs exhibit a double barrier structure for the top-to-bridge (t2b) geometry whereas the other DFs tested do not. The PBEα57-DF2[12] SRP-DF is the only DF that predicts a negative early barrier to reaction for this reaction.

We have checked the fit accuracy of our CRP[121] PES for the B86SRP68-DF2 DF for H_2 + Cu(111) using ∼4900 randomly sampled geometries. Based on all the randomly sampled points taken together our CRP[121] fit has a root mean square (rms) error of 31 meV. When only looking at the 3538 geometries that have an interaction energy of H_2 with the surface lower then 4 eV the rms error is reduced to 8 meV (∼ 0.2 kcal/mol). Our CRP[121] PES is thus highly accurate with respect to the underlying electronic structure calculations. Since the other PESs calculated for this paper have been constructed in the same manner, we presume their accuracy with respect to the electronic structure calculations to be similar, and high enough for our purposes.

	bridge			t2b			hcp			ξ
	E_b	r_b	Z_b	E_b	r_b	Z_b	E_b	r_b	Z_b	
SRP48[11,42]	0.636	1.030	1.172	0.887	1.396	1.394	1.047	1.539	1.269	0.411
B86SRP68-DF2	0.725	1.045	1.169	0.936	1.380	1.392	1.056	1.379	1.273	0.331
SRPsol63-DF2	0.712	1.045	1.167	0.925	1.379	1.392	1.038	1.373	1.270	0.326
PBEα57-DF2	0.720	1.063	1.142	0.934	1.385	1.390	1.035	1.373	1.268	0.315
optPBE-DF1[42]	0.712	1.053	1.165	0.915	1.382	1.396	1.070	1.427	1.271	0.358
MS-B86bl[13]	0.683	0.997	1.205	0.895	1.351	1.391	1.079	1.369	1.266	0.396

TABLE 5.7: Barrier heights for H_2 reacting on Cu(111) for high symmetry geometries. For the bridge site $\phi = 90°$ and $\theta = 90°$, for the t2b and hcp geometries $\phi = 0°$ and $\theta = 90°$. The high symmetry locations are shown in figure 5.1b, the t2b geometry refers to the COM of the molecule being placed on a top site, with the H-atoms pointing to the nearest bridge sites. Barrier heights are in eV, and the barrier positions in Å. Additionally the energetic corrugation, ξ, is also shown in eV.

	bridge			t2b			fcc		
	E_b	r_b	Z_b	E_b	r_b	Z_b	E_b	r_b	Z_b
SRP48[20]	1.38	1.27	1.10	1.69	1.57	1.51	1.70	1.67	1.34
B86SRP68-DF2	1.379	1.286	1.125	1.614	1.549	1.510	1.608	1.591	1.354
PBEα57-DF2	1.409	1.292	1.114	1.640	1.555	1.511	1.613	1.586	1.348
MS-PBEl	1.288	1.230	1.116	1.534	1.508	1.493	1.601	1.566	1.314

TABLE 5.8: Barrier heights for H_2 reacting on Ag(111). For the bridge site $\phi = 90°$ and $\theta = 90°$, while for the t2b and fcc sites $\phi = 0°$ and $\theta = 90°$. The high symmetry locations are shown in figure 1b, the t2b geometry refers to the COM of the molecule being placed on a top site, with the molecular bond pointing to a bridge site. Barrier heights are in eV, and the barrier positions in Å.

	bridge			t2b			t2h $\phi = 30°$			ξ
	E_b	r_b	Z_b	E_b	r_b	Z_b	E_b	r_b	Z_b	
PBE	1.245	1.187	1.096	1.237	1.504	1.468	1.637	1.685	1.549	0.392
SRP48[145]	1.407	1.180	1.089	1.382	1.493	1.470	1.783	1.689	1.552	0.376
PBEα57-DF2	1.496	1.232	1.071	1.340	1.492	1.469	1.707	1.664	1.558	0.211
B86SRP68-DF2	1.470	1.218	1.091	1.333	1.480	1.470	1.704	1.659	1.556	0.234
MS-PBEl[13]	1.432	1.144	1.127	1.301	1.433	1.466	1.701	1.578	1.538	0.269
MS-B86bl[13]	1.481	1.142	1.130	1.355	1.438	1.467	1.753	1.583	1.539	0.272

TABLE 5.9: Barrier heights for H_2 reacting on Au(111). For the bridge site $\phi = 90°$ and $\theta = 90°$, for the t2b site $\phi = 0°$ and $\theta = 90°$, and for the t2h site $\phi = 0°$ and $\theta = 30°$. The high symmetry locations are shown in figure 1b, the t2b geometry refers to the COM of the molecule being placed on a top site, with the molecular bond pointing to a bridge site. Barrier heights are in eV, and the barrier positions in Å. Additionally the energetic corrugation, ξ, is shown in eV as well.

	t2b early			t2b late			bridge			t2h $\phi = 30°$		
	E_b	r_b	Z_b	E_b	r_b	Z_b	E_b	r_b	Z_b	E_b	r_b	Z_b
SRP48	0.096	0.769	2.256				0.473	0.831	1.628	0.252	0.802	1.860
B86SRP68-DF2	0.050	0.776	2.157				0.505	0.853	1.547	0.246	0.816	1.778
PBEα57-DF2[12]	-0.008	0.769	2.202	-0.055	1.096	1.549	0.275	0.837	1.777	0.200	0.837	1.679
MS-PBEl[13]	0.145	0.766	2.205	-0.035	1.096	1.529	0.616	0.838	1.599	0.339	0.800	1.840

TABLE 5.10: Barrier heights for H_2 reacting on Pt(111). For the bridge site $\phi = 90°$ and $\theta = 90°$, for the t2b site $\phi = 0°$ and $\theta = 90°$, and for the t2h site $\phi = 0°$ and $\theta = 30°$. The high symmetry locations are shown in figure 1b, the t2b geometry refers to the COM of the molecule being placed on a top site, with the molecular bond pointing to a bridge site. Barrier heights are in eV, and the barrier positions in Å.

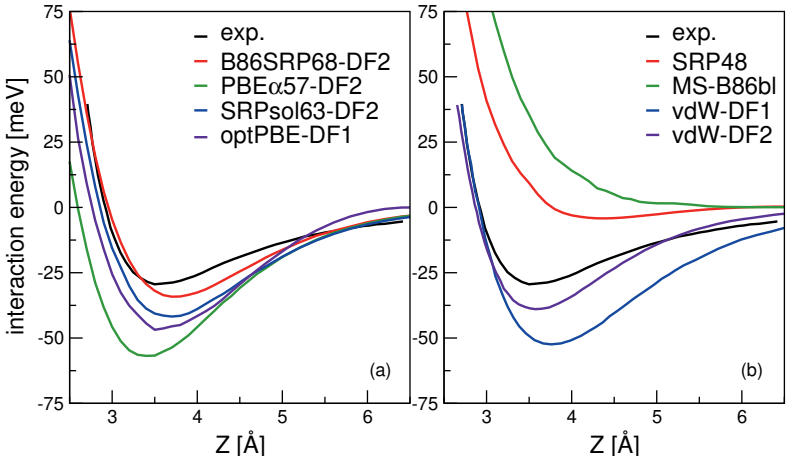

FIGURE 5.3: The computed interaction energy of H_2 parallel to the Cu(111) surface above a top site ($\phi = 0°, \theta = 90°$) is compared with experimental results[60] (black). Panel (a) shows the calculated Van der Waals well for the B86SRP68-DF2 (red), PBEα57-DF2 (green), SRPsol63-DF2 (blue) and optPBE-DF1[42] (purple) DFs, and panel (b) for the SRP48[11] (red), MS-B86bl[13] (green), vdW-DF1[97] (blue) and vdW-DF2[98] (purple) DFs.

Van der Waals wells

Figures 5.3a and b show Van der Waals potential curves for H_2 in a parallel orientation ($\phi = 0°, \theta = 90°$) above a top atom of Cu(111) for different DFs, comparing with experimental results[60]. Panel a shows calculated Van der Waals wells obtained with the non-standard DFs with non-local Van der Waals correlation investigated in this work. Panel b shows Van der Waals potential curves for SRP-DFs developed previously in our group[11,13], as well as for the two standard vdW-DF1[97] and vdW-DF2[98] DFs. Agreement with experiment is best for the B86SRP68-DF2 DF.

All Van der Waals well depths and geometries for the systems and DFs investigated in this work are tabulated in table 5.11. With respect to the Van der Waals well depths for H_2 + Ag(111), H_2 + Au(111), and H_2 + Pt(111) we find depths that are in good agreement with experimental work[62,91,100,111] for the B86SRP68-DF2 DF.

Cu(111)	Z [Å]	E_{vdW} [meV]
exp.	3.51[60], 2.71[62]	29.5[60], 22.2[62]
SRP48[11]	4.38	3.73
vdW-DF1	3.77	52.4
vdW-DF2	3.58	39.0
B86SRP68-DF2	3.74	34.3
PBEα57-DF2	3.34	56.7
SRPsol63-DF2	3.71	41.8
optPBE-DF2[42]	3.52	46.9
Ag(111)		
exp.[91]	1.98	32.5
SRP48[20]	4.42	2.3
B86SRP68-DF2	3.75	33.3
PBEα57-DF2	3.39	56.1
Au(111)		
exp.[62]	2.2	40.0
SRP48[145]	4.26	3.0
B86SRP68-DF2	3.62	41.4
PBEα57-DF2	3.30	68.7
Pt(111)		
exp.		55[100], 76[111]
SRP48	4.14	5.5
B86SRP68-DF2	3.48	48.0
PBEα57-DF2	3.24	72.4

TABLE 5.11: Van der Waals well depths and positions for Cu(111), Ag(111), Au(111) and Pt(111).

5.3.2 Molecular beam sticking probabilities

Molecular beam sticking probabilities computed with five DFs for H_2 and D_2 reacting on Cu(111) are shown in figure 5.4, comparing to experimental results of Auerbach and coworkers[46,52] and Rendulic and coworkers[47]. Figure 5.5 shows the comparison with an additional experiment for the five DFs discussed here, namely for the pure D_2 molecular beams of Auerbach and coworkers[46]. The difference between theory and experiment is assessed by determining how far the theoretical result needs to be shifted along the incidence energy axis to be superimposed on a spline interpolated curve going through the experimental results. Values of the mean absolute deviation (MAD) are calculated as the mean of the absolute number of these shifts for a particular set of molecular beam experiments From the MAD values it can be seen that all five DFs considered describe the experiments on H_2 + Cu(111) shown in figure 5.4 with chemical accuracy. Figure 5.6 shows comparisons to two additional sets of molecular beam experiments of Auerbach and coworkers[46,52] for H_2 reacting on Cu(111) for a more limited set of DFs.

For the B86SRP68-DF2 DF QD results are also shown for the experiments concerning H_2 in figures 5.4e,f and in figure 5.6. Note that in these figures the

QCT results are based on more rovibrational states than those included in the QD calculations (see table 5.3). In figure 5.7 we also explicitly compare QCT and QD results obtained while averaging over the same rovibrational states, and compare those to the QCT results shown in figures 5.4e,f and in figure 5.6. Table 5.12 displays the computed MADs for all experiments considered.

Figure 5.8 shows molecular beam sticking experiments for D_2 reacting on Ag(111). Experimental results of Hodgson and coworkers[147] are also shown. The calculated results are obtained using the pure D_2 molecular beam parameters of Auerbach and coworkers[46] obtained from experiments on Cu(111). The DFs treated in this work, as well as the MS-PBEl mGGA[13], reproduce the experiment to almost within chemical accuracy. The SRP48 DF[20,63] yields the worst and the MS-PBEl[13] the best performance.

In figure 5.9 molecular beam sticking probabilities for D_2 reacting on Pt(111) for three DFs are shown, comparing to the molecular beam experiments of Luntz et al.[65]. A comparison to the experimental results of Cao et al.[61] is shown in figure 5.10. For the comparison to the experiment of Luntz et al.[65] the molecular beam parameters of Groot et al.[128] are used, while Cao et al.[61] have actually reported their molecular beam parameters. Figure 5.9a shows that the B86SRP68-DF2 DF describes the experiment[65] with overall chemical accuracy, albeit that the energy shifts are larger than 4.2 kJ/mol at the lowest energies. However, figure 5.10a shows that the experiments of Cao et al.[61] are not described to within chemical accuracy using the B86SRP68-DF2 DF. The SRP48 and MS-PBEl DFss are not able to describe either experiment to within chemical accuracy.

The parameters describing the beams used in the experiment can be found in table 5.4.

5.3.3 Initial-state resolved reaction probabilities

Initial-state resolved reaction probabilities will be presented for H_2 reacting on both Cu(111) and Ag(111). Figure 5.11 shows fully initial-state resolved reaction probabilities for H_2 reacting on Cu(111), as obtained with the QD and QCT methods. At the level of degeneracy averaged reaction probabilities the agreement is very good (figures 5.11a,c), but the QD method predicts a slightly larger orientational dependence of the reaction probability (figure 5.11b). Figure 5.12 shows a comparison of degeneracy averaged reaction probabilities obtained using the QD and QCT method for the 20 rovibrational states included in the QD calculations. The agreement between the QD and QCT method is very good for all states, though there are some differences for the $J < 3$ rovibrational states.

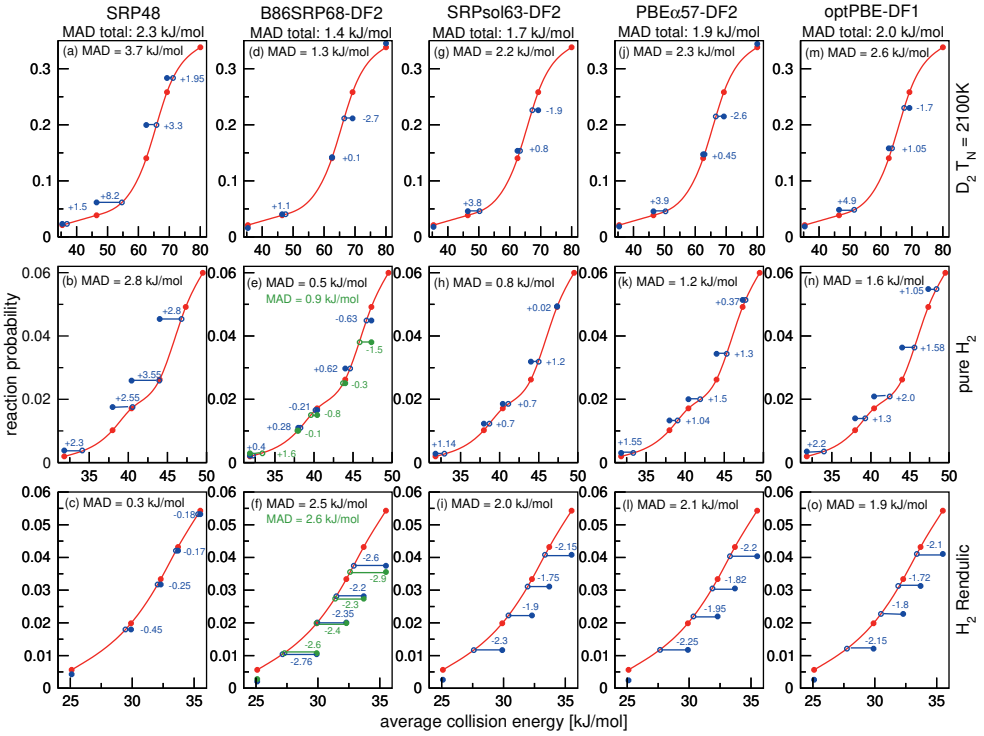

FIGURE 5.4: Molecular beam sticking probabilities for H_2 and D_2 reacting on Cu(111) for three sets of molecular beam experiments, as computed with five SRP-DFs. Experimental results are shown in red[46,47,52], QCT results are shown in blue, and QD results are shown in green in two panels (panels e and f). The values next to each data point denote the shift along the translational energy axis from the computed reaction probability to the interpolated experimental reaction probability curve in kJ/mol. The MAD values are the mean value of the absolute energy differences for each experiment.

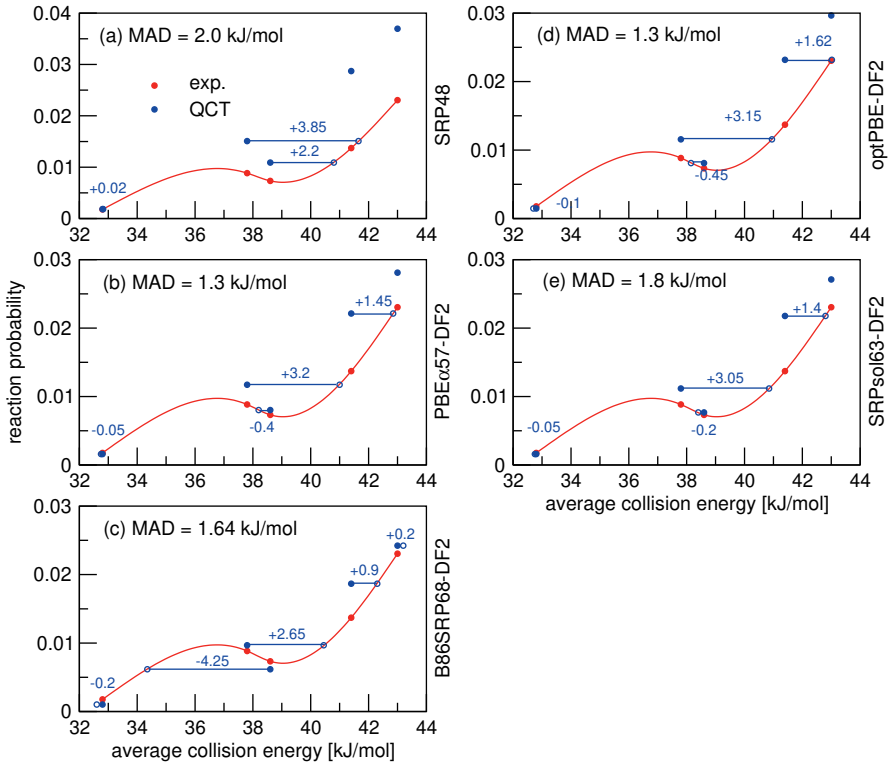

FIGURE 5.5: Molecular beam sticking probabilities for D_2 reacting on Cu(111). Experimental values are shown in red[46]. QCT results are shown in blue. The values next to each data point denote the shift along the translational energy axis from the computed reaction probability to the interpolated experimental reaction probability curve in kJ/mol.

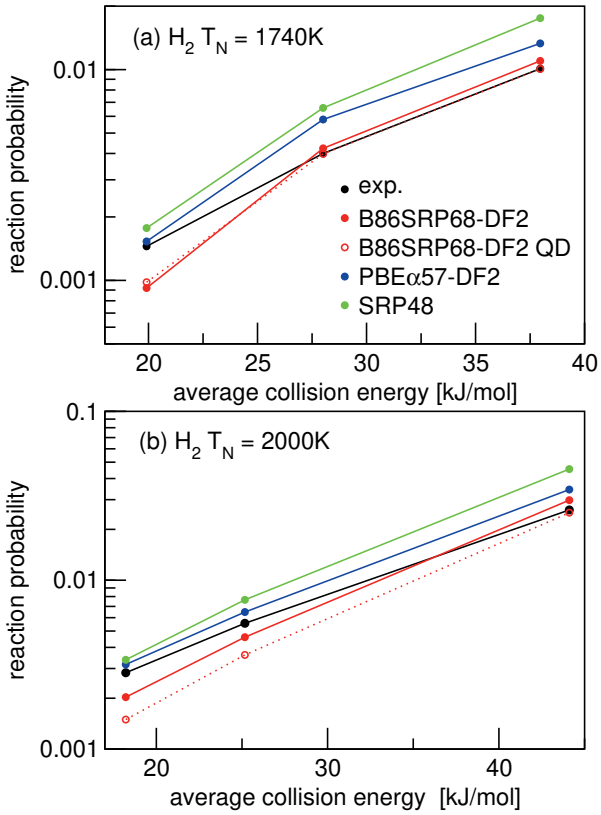

FIGURE 5.6: Molecular beam sticking probabilities for H_2 reacting on Cu(111). Experimental values are shown in black[52], computed reaction probabilities are shown for the B86SRP68-DF2 (red), PBEα57-DF2 (blue), and the SRP48 (green) DFs. The solid lines correspond to QCT calculations, the dashed lines to QD calculations.

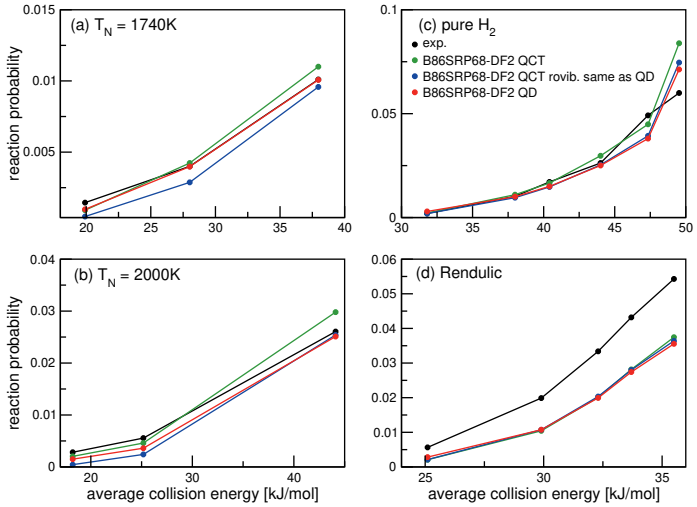

FIGURE 5.7: Molecular beam sticking probabilities for H_2 reacting on Cu(111). Experimental values are shown in black[52], B86SRP68-DF2 QCT results are shown in green, B86SRP68-DF2 QCT results based on the same rovibrational states as taken into account in the QD calculations in blue, and B86SRP68-DF2 QD results in red.

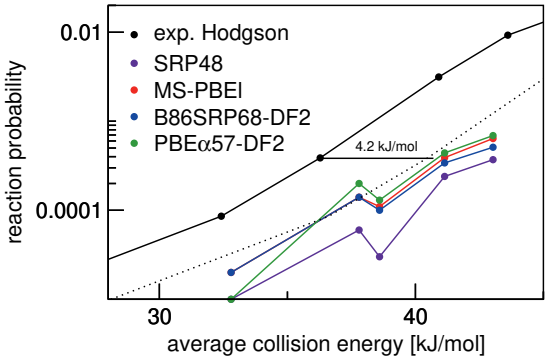

FIGURE 5.8: Molecular beam sticking probability as a function of the average incidence energy for D_2 reacting on Ag(111). Experiment is shown in black[147]. QCT results are shown for the following DFs: SRP48 (purple)[20], MS-PBEl (red)[13], B86SRP68-DF2 (blue), and PBEα57-DF2 (green). The dotted line represents the experimental curve shifted by 4.2 kJ/mol, denoting the limit to chemical accuracy.

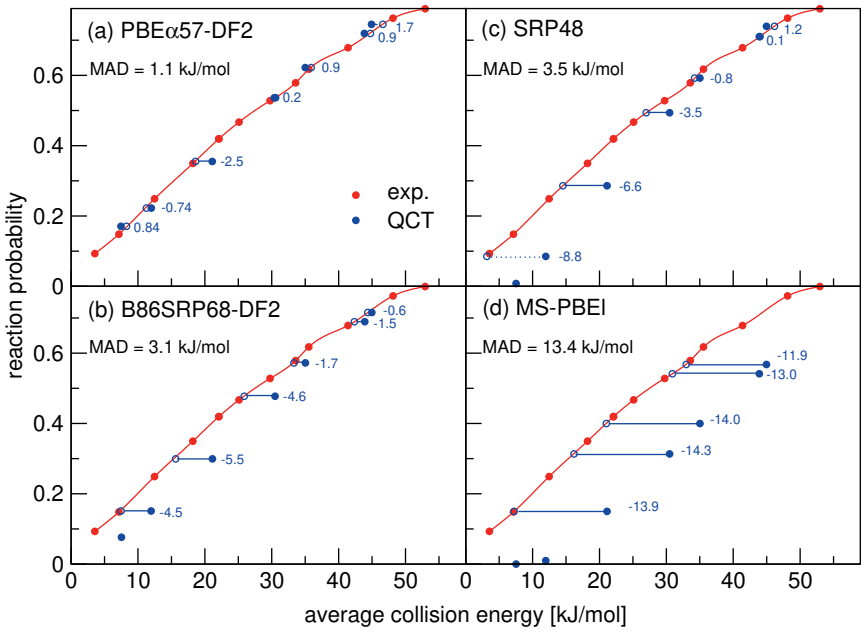

FIGURE 5.9: Molecular beam sticking probabilities for D_2 reacting on Pt(111) for (a) the PBEα57-DF2, (b) B86SRP68-DF2, (c) SRP48 and (d) MS-PBEl DFs. Experimental results are shown in red[65], QCT results in blue. The values next to each data point denote the shift along the translational energy axis from the computed reaction probability to the interpolated experimental reaction probability curve.

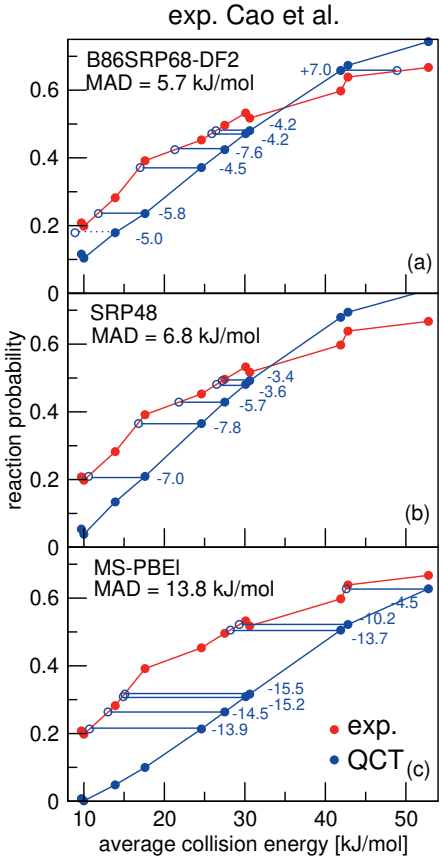

FIGURE 5.10: Molecular beam sticking probabilities for D_2 reacting on Pt(111) for the B86SRP68-DF2, SRP48 and MS-PBEl functionals. Experimental values are shown in red[61]. QCT results are shown in blue. The values next to each data point denote the shift along the translational energy axis from the computed reaction probability to the interpolated experimental reaction probability curve.

H_2 / D_2 + Cu(111)	D_2 T_N = 2100K		pure D_2		pure H_2		H_2 Rendulic[47]		H_2 T_N = 2000K		H_2 T_N = 1740K	
exp.[46]	MAD	MSD	MAD	MSD	MAD	MSD	MAD	MSD	MAD	MSD	MAD	MSD
SRP48	3.7	3.7	2.0	2.0	2.8	2.8	0.3	-0.3	1.6	1.6	2.6	2.6
B86SRP68-DF2	1.3	-0.5	1.6	-0.1	0.5	0.3	2.5	-2.5	1.9	-1.9	0.4	0.4
SRPsol63-DF2	2.2	0.9	1.2	1.1	0.8	0.8	2.0	-2.0	0.2	0.2	0.9	0.5
PBEα57-DF2[12]	2.3	0.6	1.3	1.1	1.2	1.2	2.1	-2.1	0.8	0.8	1.7	1.7
optPBE-DF2	2.6	1.4	1.3	1.1	1.6	1.6	1.9	-1.9	0.6	0.6	1.4	1.4
MS-B86bl[13]	1.7	0.5	1.2	-0.8	0.3	0.2	2.0	-2.0	2.8	-2.8	0.6	0.6

D_2 + Pt(111)	exp. Luntz[65]		exp. Cao[61]	
	MAD	MSD	MAD	MSD
PBEα57-DF2	1.1	0.19	1.9	-1.1
SRP48	3.5	-3.1	6.8	-6.8
B86SRP68-DF2	3.1	-3.1	5.7	-3.5
MS-PBE[13]	13.4	-13.4	13.8	-13.8

D_2 + Ag(111)	exp. Hodgson[55]	
	MAD	MSD
SRP48[20]	8.4	-8.4
B86SRP68-DF2	4.6	-4.6
PBEα57-DF2[12]	4.3	-4.3
MS-PBEl[13]	4.5	-4.5

TABLE 5.12: Mean absolute and mean signed deviations (MADs and MSDs, in kJ/mol) of the sticking probabilities computed with different DFs for the experimental reaction probability curves.

Figure 5.13 shows degeneracy averaged initial-state resolved reaction probabilities for H_2 and D_2 reacting on Ag(111). A comparison is made to reaction probabilities extracted from associative desorption experiments assuming detailed balance[78,79]. The agreement with experiment seems best for D_2 and when using the MS-PBEl mGGA[13]. Note, however, that the $P_{\mathrm{deg}}(E,\nu,J)$ extracted from experiments were not normalized, but simply assumed to saturate at unity, making it hard to perform an accurate comparison with experiment.

5.3.4 $\mathbf{E}_{1/2}(\nu, J)$ parameters

$\mathrm{E}_{1/2}(\nu, J)$ parameters calculated for H_2 (D_2) + Cu(111) using method A1 and method B1 are shown in figure 5.14 and figure 5.15, respectively, also comparing with experiment[48]. Using method B1, the DFs that include non-local correlation qualitatively reproduce the rotational hindering observed experimentally for ($\nu = 0$), i.e. the increase of $E_{1/2}(\nu, J)$ parameters with increasing J for low J before decreasing with increasing J. A third degree polynomial has been fitted to the calculated $\mathrm{E}_{1/2}(\nu, J)$ parameters, which describes the dependence of the $\mathrm{E}_{1/2}(\nu, J)$ parameters on J. The polynomials are shown, without the energy axis offset resulting from the fit to a third degree polynomial, in figure 5.16.

$\mathrm{E}_{1/2}(\nu, J)$ parameters calculated for H_2 (D_2) + Au(111) using method B2 are shown in figure 5.17, also comparing to experiment[71].

Accompanying MAD and mean signed deviations (MSD) values of the computed $\mathrm{E}_{1/2}(\nu, J)$ parameters from the experimental values are presented in table 5.13 for both H_2 (D_2) + Cu(111) and H_2 (D_2) + Au(111).

5.3.5 Rotational quadrupole alignment parameters Cu(111)

In figure 5.18 we compare calculated rotational quadrupole alignment parameters using the QCT method to experimental ones for D_2 desorbing from Cu(111)[50]. Note that a positive $A_0^{(2)}(\nu, J)$ indicates a preference for parallel reaction, a negative value a preference for perpendicular reaction, and zero means the reaction proceeds independent of D_2 orientation. We observe only a monotonous increase of the rotational quadrupole alignment parameters with decreasing translational energy, indicating that at translational energies close to the reaction threshold molecules prefer to react in a parallel orientation.

5.3.6 Inelastic scattering of H_2 from Cu(111)

Vibrationally inelastic scattering probabilities, $P(\nu = 0, J \rightarrow \nu = 1, J = 3)$ for H_2 scattering from Cu(111) are shown in figure 5.19 for scattering from the initial $J = 1, 3$ and 5 states. Results were obtained using the QD method. The

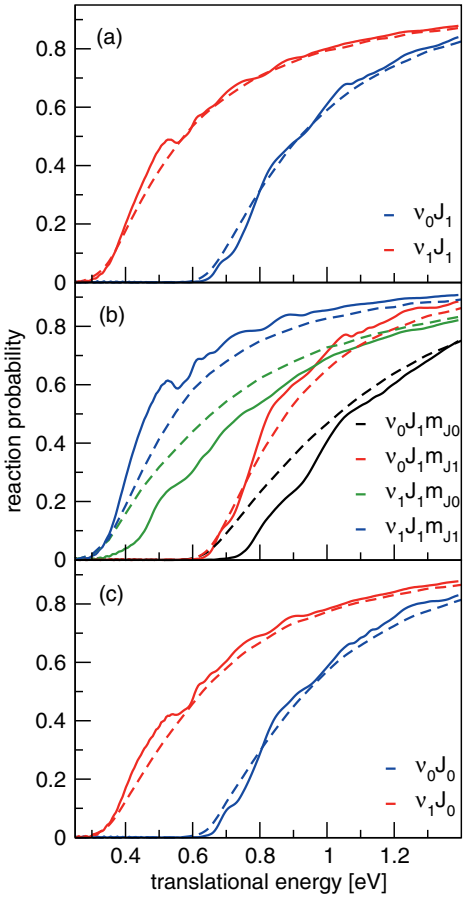

FIGURE 5.11: Reaction probabilities computed for H_2 + Cu(111) with QD calculations (solid lines) and QCT calculations (dashed lines) for normal incidence using the B86SRP68-DF2 DF. Degeneracy averaged reaction probabilities computed for $J = 1$ for both the ground state and the first vibrationally excited state (a). Fully initial-state resolved reaction probabilities are shown for the $m_J = 0$ and 1 states belonging to $J = 1$ for both the ground vibrational and the first excited vibrationally state (b). Reaction probabilities computed for the $J = 0$ state for both the ground vibrational and the first excited vibrational state (c).

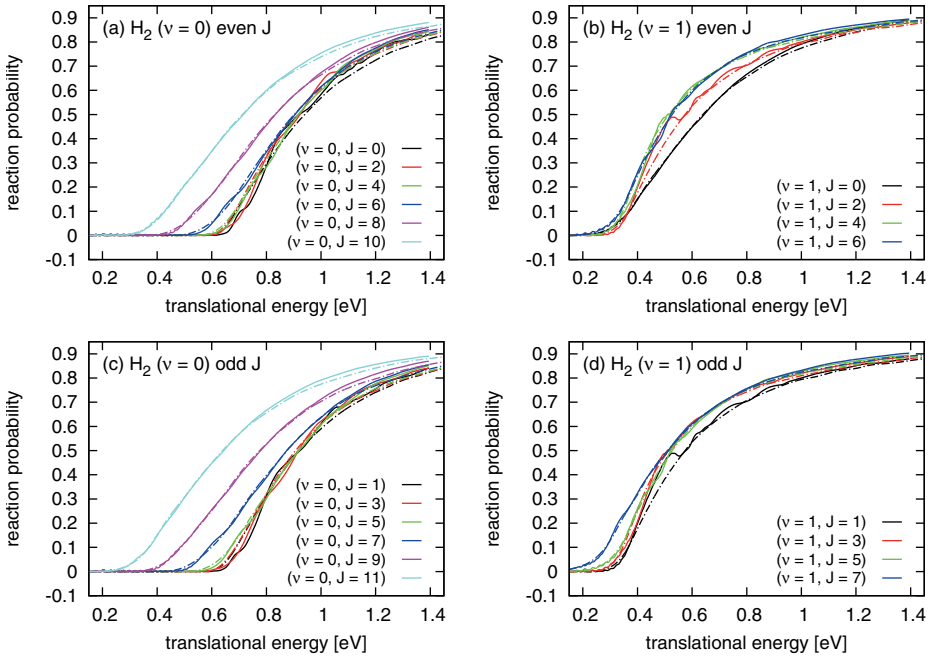

FIGURE 5.12: Degeneracy averaged reaction probabilities for H_2 reacting on Cu(111), obtained using the B86SRP68-DF2 functional. Solid lined correspond to QD results, dot-dashed lines correspond to QCT results.

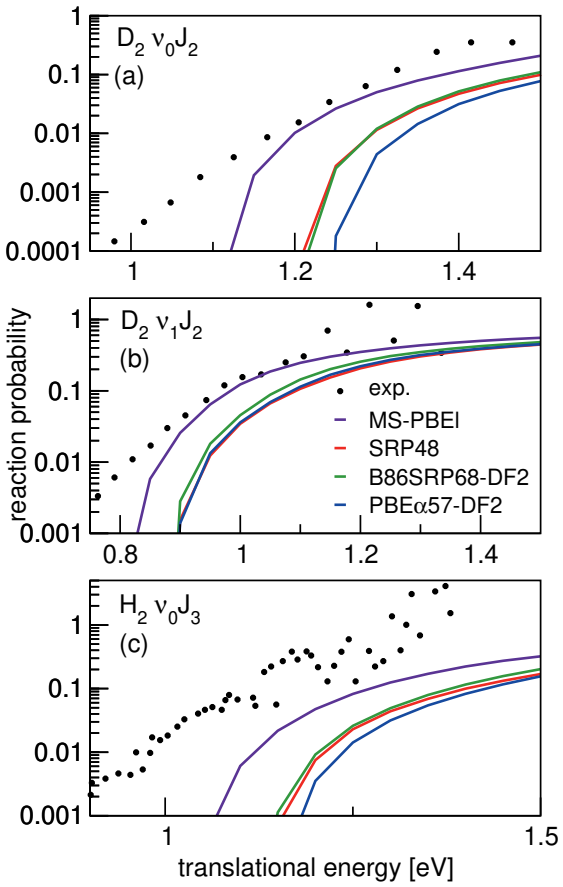

FIGURE 5.13: Initial-state selected reaction probabilities $P_{deg}(E, \nu, J)$ computed for H_2 (D_2) + Ag(111) using the MS-PBEl (purple), SRP48[20] (red), B86SRP68-DF2 (green) and the PBEα57-DF2 (blue) DFs are shown as a function of translational energy, comparing with values extracted from associative desorption experiments[78,79]. Results are shown for D_2 ($\nu = 0, J = 2$) (a), D_2 ($\nu = 1, J = 2$) (b), and H_2 ($\nu = 0, J = 3$) (c).

Cu(111) Method A1	MAD (eV) H_2			MSD (eV) H_2			MAD (eV) D_2			MSD (eV) D_2		
	total	$\nu=0$	$\nu=1$	total	$\nu=0$	$\nu=1$	total	$\nu=0$	$\nu=1$	total	$\nu=0$	$\nu=1$
SRP48[11]	0.0434	0.0522	0.0301	0.0373	0.0522	0.0151	0.0254	0.0243	0.0272	-0.0066	-0.0008	-0.0152
MS-B86bl[13]	0.0274	0.0165	0.0438	-0.0149	0.0044	-0.0438	0.0551	0.0440	0.0717	-0.0551	-0.0440	-0.0717
B86SRP68-DF2	0.0209	0.0142	0.0308	-0.0176	-0.0089	-0.0308	0.0663	0.0640	0.0698	-0.0663	-0.0640	-0.0698
B86SRP68-DF2 QD	0.0231	0.0183	0.0303	-0.0222	-0.0169	-0.0303						
Dai et al.[38] QD		0.0091			0.0017							
PBEα57-DF2	0.0140	0.0117	0.0174	0.0040	0.0054	0.0018	0.0573	0.0615	0.0509	-0.0573	-0.0616	-0.0509
SRPsol63-DF2	0.0153	0.0136	0.0177	-0.0025	0.0064	-0.0158	0.0510	0.0487	0.0545	-0.0511	-0.0487	-0.0545
optPBE-DF1[42]	0.0146	0.0147	0.0143	0.0054	0.0111	-0.0032	0.0480	0.0481	0.0478	-0.0480	-0.0615	-0.0478

Cu(111) Method B1	MAD (eV) H_2			MSD (eV) H_2			MAD (eV) D_2			MSD (eV) D_2		
	total	$\nu=0$	$\nu=1$	total	$\nu=0$	$\nu=1$	total	$\nu=0$	$\nu=1$	total	$\nu=0$	$\nu=1$
SRP48[11]	0.0409	0.0317	0.0549	-0.0409	-0.0317	-0.0549	0.0336	0.0252	0.0336	-0.0332	-0.0246	-0.0460
MS-B86bl[13]	0.0826	0.0664	0.1067	-0.0826	-0.0664	-0.1068	0.0712	0.0567	0.0929	-0.0712	-0.0567	-0.0929
B86SRP68-DF2	0.0843	0.0756	0.0974	-0.0843	-0.0756	-0.0974	0.0785	0.0709	0.0898	-0.0785	-0.0709	-0.0897
B86SRP68-DF2 QD	0.0846	0.0812	0.0897	-0.0845	-0.0813	-0.0897						
Dai et al.[38] QD		0.0703			-0.0703							
PBEα57-DF2	0.0676	0.0647	0.0718	-0.0676	-0.0648	-0.0718	0.0674	0.0642	0.0723	-0.0674	-0.0642	-0.0723
SRPsol63-DF2	0.0738	0.0660	0.0855	-0.0738	-0.0660	-0.0855	0.0682	0.0613	0.0785	-0.0682	-0.0613	-0.0785
optPBE-DF1[42]	0.0688	0.0635	0.0768	-0.0688	-0.0635	-0.0767	0.0642	0.0583	0.0729	-0.0642	-0.0583	-0.0729

Au(111) Method B1	MAD (eV) H_2			MSD (eV) H_2			MAD (eV) D_2			MSD (eV) D_2		
	total	$\nu=0$	$\nu=1$	total	$\nu=0$	$\nu=1$	total	$\nu=0$	$\nu=1$	total	$\nu=0$	$\nu=1$
PBE	0.1025	0.1333	0.0718	0.1025	0.1333	0.0718	0.0955	0.1178	0.0734	0.0955	0.1176	0.0733
SRP48[145]	0.0309	0.0468	0.0151	0.0158	0.0468	-0.0151	0.0229	0.0325	0.0133	0.0094	0.0321	-0.0131
PBEα57-DF2	0.0189	0.0241	0.0136	0.0026	0.0177	-0.0125	0.0187	0.0246	0.0127	0.0125	0.0246	0.0005
B86SRP68-DF2	0.0270	0.0457	0.0083	0.0217	0.0457	-0.0022	0.0190	0.0275	0.0105	0.0113	0.0275	-0.0050
optPBE-DF1[145]	0.0260	0.0225	0.0259	-0.0044	0.0206	-0.0296	0.0212	0.0116	0.0309	-0.0143	0.0023	-0.0307
MS-PBEl[13]	0.0329	0.0393	0.0264	0.0028	0.0320	-0.0264	0.0270	0.0116	0.0105	0.0212	0.0435	-0.0009

Au(111) Method B2	MAD (eV) H_2			MSD (eV) H_2			MAD (eV) D_2			MSD (eV) D_2		
	total	$\nu=0$	$\nu=1$	total	$\nu=0$	$\nu=1$	total	$\nu=0$	$\nu=1$	total	$\nu=0$	$\nu=1$
PBE	0.0464	0.0471	0.0457	-0.0463	-0.0470	-0.0457	0.0579	0.0551	0.0607	-0.0579	-0.0551	-0.0607
SRP48[145]	0.0891	0.0774	0.1008	-0.0891	-0.0774	-0.1008	0.0948	0.0856	0.1041	-0.0948	-0.0856	-0.1041
PBEα57-DF2	0.1050	0.1143	0.0958	-0.1050	-0.1143	-0.0958	0.0957	0.0905	0.1009	-0.0957	-0.0905	-0.1009
B86SRP68-DF2	0.0854	0.0797	0.0911	-0.0854	-0.0797	-0.0911	0.0955	0.0888	0.1015	-0.0951	-0.0888	-0.1015
optPBE-DF1[145]	0.0959	0.0860	0.1058	-0.0959	-0.0860	-0.1058	0.1037	0.0952	0.1123	-0.1037	-0.0952	-0.1123
MS-PBEl[13]	0.1057	0.1043	0.1072	-0.1057	-0.1043	-0.1072	0.0918	0.0836	0.1000	-0.0835	-0.0551	-0.1120

TABLE 5.13: Mean absolute and mean signed deviations of the theoretical $E_{1/2}(\nu, J)$ parameters from the experimental $E_0(\nu, J)$ values for H_2 (D_2) + Cu(111)[48] and H_2 (D_2) + Au(111)[71].

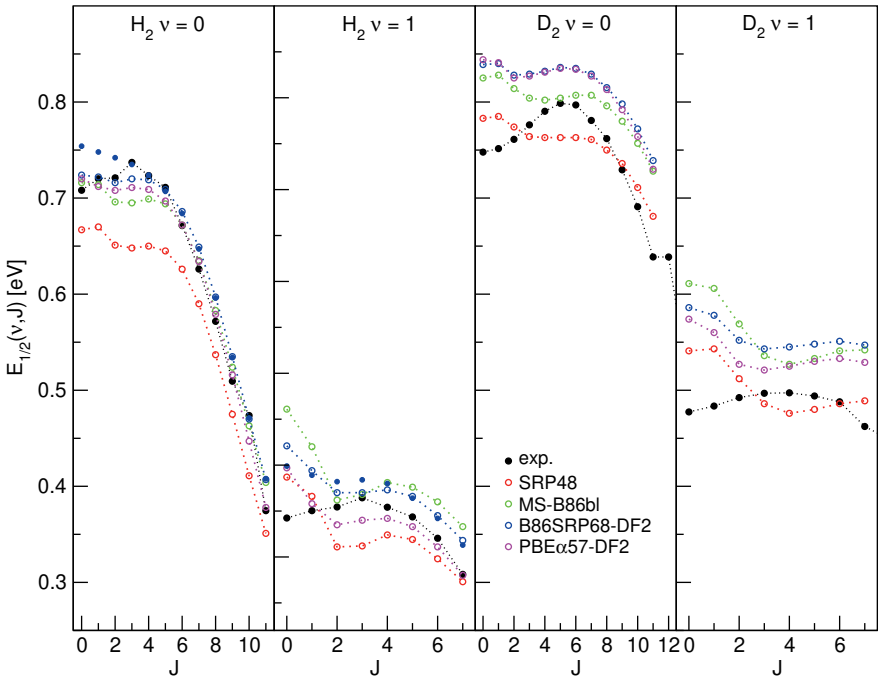

FIGURE 5.14: $E_{1/2}(\nu, J)$ parameters as a function of J obtained using method A1 for H_2 and D_2 reacting on Cu(111). Red circles represent the SRP48 values[63], green circles the MS-B86bl values[13], blue circles represent the B86SRP68-DF2 values with the solid blue circles corresponding to QD calculations, magenta circles represent the PBEα57-DF2 values, and solid black circles represent experimental results[48].

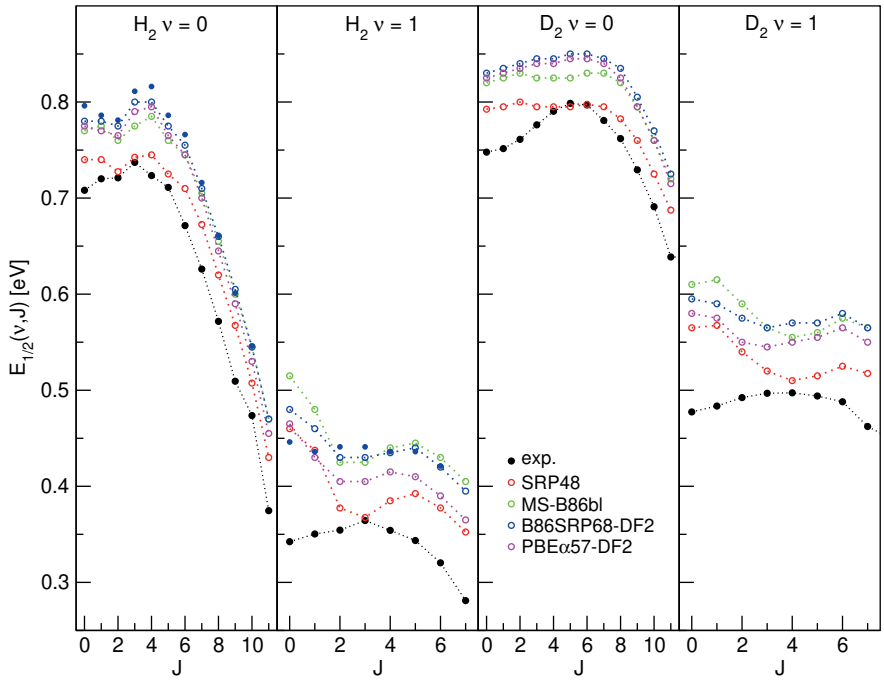

FIGURE 5.15: $E_{1/2}(\nu, J)$ parameters as a function of J obtained using method B1 for H_2 and D_2 reacting on Cu(111). Red circles represent the SRP48 values[63], green circles the MS-B86bl values[13], blue circles the B86SRP68-DF2 values with the solid blue circles corresponding to QD calculations, magenta circles represent the PBEα57-DF2 values, and solid black circles represent experimental results[48].

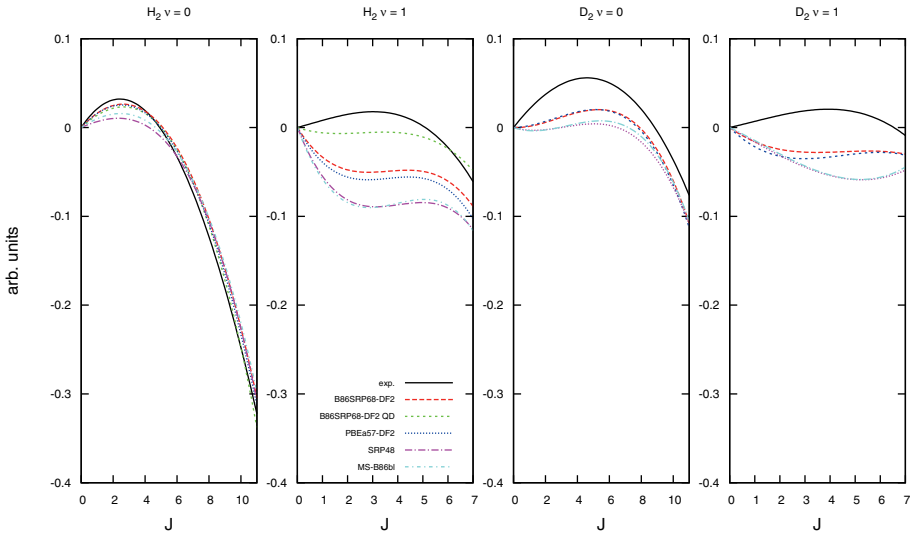

FIGURE 5.16: The trend in the J-dependence of the $E_{1/2}(\nu, J)$ parameters calculated using procedure B1 as a function of J for the H_2 (D_2) + Cu(111) system. Here the trend is represented by third degree polynomial fits of the calculated and experimental[48] results, plotted here without the y-axis offset for easy comparison.

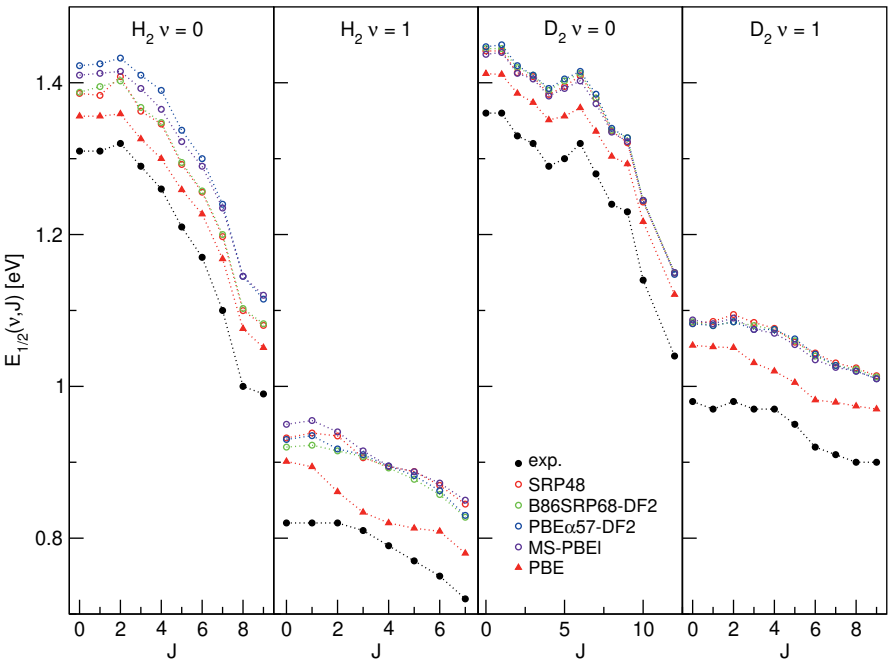

FIGURE 5.17: $E_{1/2}(\nu, J)$ parameters as a function of J obtained using method B2 for H_2 and D_2 reacting on Au(111), experimental values are shown in black[71]. Red circles represent the SRP48 values[145], green circles the B86SRP68-DF2 values, blue circles the PBEα57-DF2[12] values, purple circles the MS-PBEl[13] values and red triangles the PBE values[145].

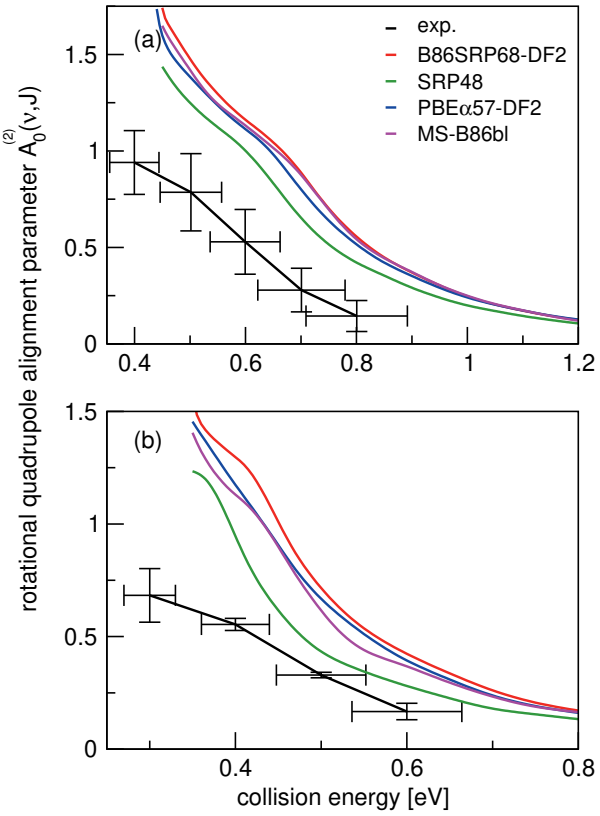

FIGURE 5.18: Panel (a) shows rotational quadrupole alignment parameter, $A_0^{(2)}(\nu = 0, J = 11)$, and panel (b) shows the rotational quadrupole alignment parameter $A_0^{(2)}(\nu = 1, J = 6)$ for D_2 reacting with Cu(111). Experimental results are shown in black[50]. Theoretical results obtained using the QCT method are shown for the B86SRP68-DF2 (red), SRP48[11] (green), PBEα57-DF2[12] (blue), and the MS-B86bl[13] (magenta) DFs.

	H_2	D_2
exp.[71]	0.552	0.424
SRP48	0.250	0.473
B86SRP68-DF2	0.249	0.522

TABLE 5.14: The ratio of $\nu = 1 : \nu = 0$ molecules desorbing from Au(111) as measured in experiments[71] and computed with the SRP48 and B86SRP68-DF2 DFs.

onset of the vibrational inelastic scattering probabilities is correlated with the onset of reactivity for each particular state. The DFs yield similar results for the initial $(\nu = 0, J = 5)$ rovibrational state, except that the SRP48 DF yields smaller vibrational excitation probabilities for $E > 0.8$eV (panel c). For the $(\nu = 0, J = 1)$ and $(\nu = 0, J = 3)$ initial rovibrational states the differences are larger (panels a and b).

Figure 5.20 shows the ratio of rotationally elastic and inelastic scattering probabilities $P(\nu = 1, J = 0 \rightarrow \nu = 1, J = 2)/P(\nu = 1, J = 0 \rightarrow \nu = 1, J = 0)$ computed with two DFs and comparing with experiment[55]. Note that both curves need to be shifted by 40 meV in order to overlap with the onset of the experimental curves measured for a surface temperature of 300 K[55].

5.3.7 Rovibrational state populations of H_2 and D_2 desorbing from Au(111)

Figure 5.21 shows rovibrational state populations of H_2 and D_2 desorbing from Au(111). Here we plot $ln[N/g_N(2J+1)]$ versus the rotational energy, with N being the total population for each (ν, J) state (see Eq. 5.13) and $g_N(2J+1)$ being the statistical weight for rotational level J[71]. For D_2, $g_N = 2$ for even J and 1 for odd J; for H_2, $g_N = 1$ for even J and 3 for odd J. In such a plot a Boltzmann distribution will appear as a straight line[71]. Here we integrate Eq. 5.13 up to $E_{\max}(\nu, J)$.

Figure 5.22 shows the rovibrational state populations of H_2 desorbing from Au(111) as reported in by Shuai et al.[71] together with the values we calculate using Eq. 5.13 with an upper integration limit of 5 eV to be in line with the procedure used by Shuai et al.[71] as outlined in a private communication[148].

Table 5.14 shows the ratio of the fluxes of molecules desorbing in the first excited and in the vibrational ground state for both H_2 and D_2 desorbing from Au(111). The ratios are calculated using Eq. 5.15 and are solely based on the rovibrational states for which results are shown in figure 5.21. Again, here we integrate Eq. 5.13 up to $E_{\max}(\nu, J)$.

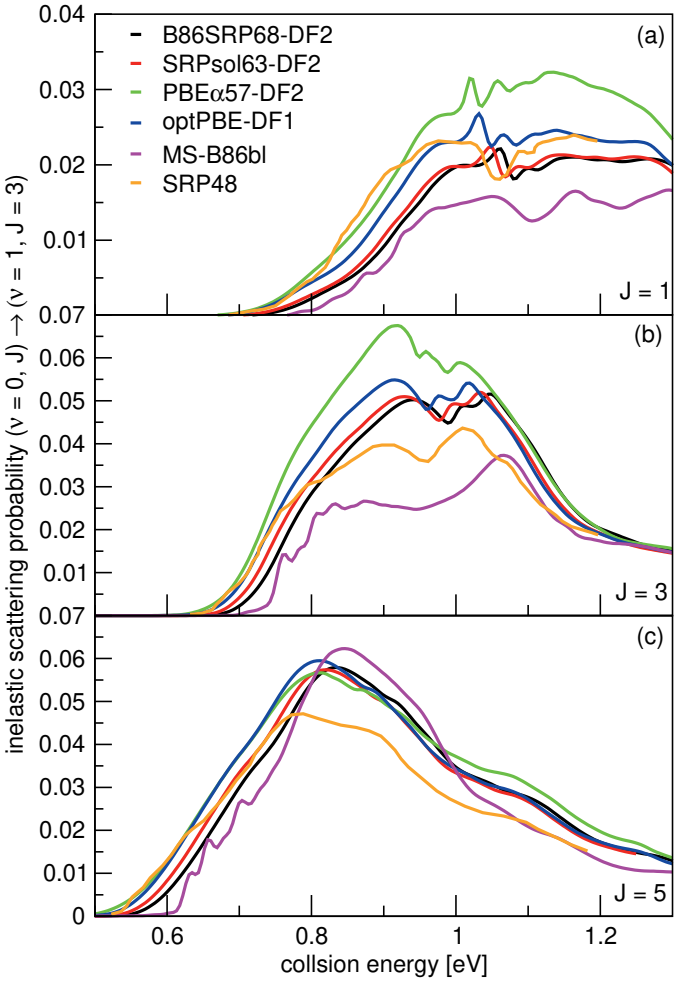

FIGURE 5.19: Vibrationally inelastic scattering probabilities for $P(\nu = 0, J \to \nu = 1, J = 3)$. Shown are results for $J = 1$ (a), $J = 3$ (b), and $J = 5$ (c). QD results for the following DFs are shown: B86SRP68-DF2 (black), SRPsol63-DF2 (red), PBEα57-DF2 (green), optPBE-DF1 (blue), MS-B86bl (magenta), and SRP48[25] (orange).

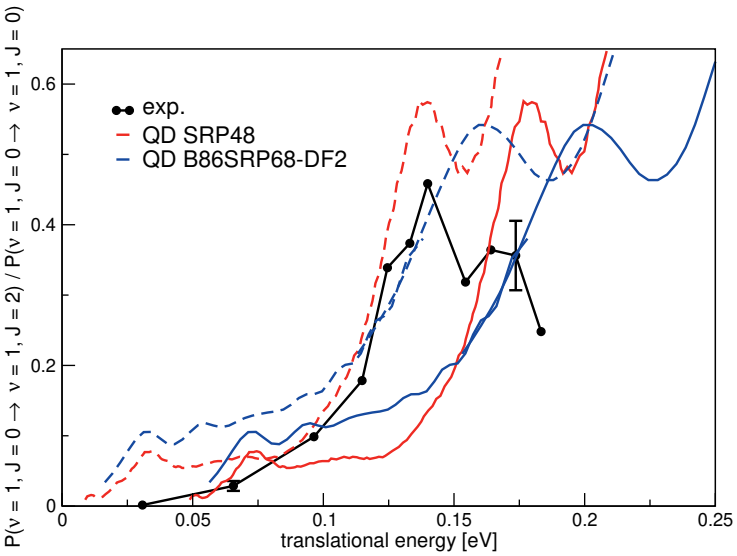

FIGURE 5.20: A comparison of the ratios of theoretical and experimental rotationally inelastic scattering probabilities $P(\nu = 1, J = 0 \rightarrow \nu = 1, J = 2)/P(\nu = 1, J = 0 \rightarrow \nu = 1, J = 0)$ for H_2 impinging on Cu(111). Experimental results are shown in black[55] with the error bars representing maximum deviations in repeated measurements constituting estimated standard deviations. QD results for the SRP48 DF are shown in red[11] and QD results for the B86SRP68-DF2 DF are shown in blue. Dashed lines constitute the calculated ratio's of rotationally inelastic scattering shifted by 40 meV.

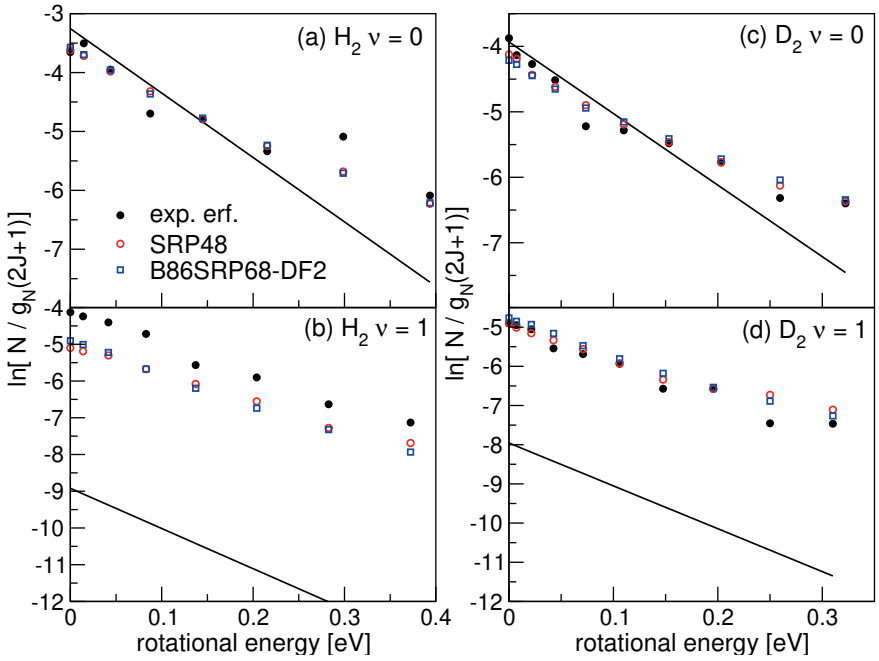

FIGURE 5.21: Rovibrational state populations of H_2 and D_2 desorbing from Au(111) are shown versus the rotational energy. Experimental results are shown in black[71], theoretical results are shown in red for the SRP48 DF[145] and in blue for the B86SRP68-DF2 DF. The straight lines represent Boltzmann distributions for the surface temperature of the experiment.

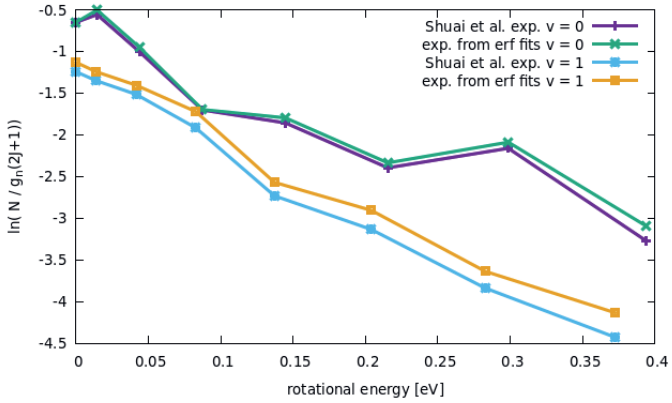

FIGURE 5.22: Rovibrational state populations of H_2 desorbing from Au(111) are plotted against the data for H_2 shown in figure 2 of ref.[71]. Here the calculated normalized experimental results based on the error function fits have been obtained by performing the integration in Eq. 18 until 5 eV to be consistent with the procedure used in ref.[71]. Additionally, the calculated curves have been shifted such that the calculated value for $(\nu = 0, J = 0)$ matches with the $(\nu = 0, J = 0)$ result reported in ref.[71], and the calculated results for $(\nu = 1)$ have been shifted by the same amount $(+3.0)$.

5.4 Discussion

Our aim has been to develop new SRP-DFs that include non-local correlation for the H_2 + Cu(111) system, and afterwards assess the transferability of these DFs to other systems. The reason for taking this approach, instead of fitting the DF to best reproduce experiments on all systems shown in the results section, is that numerous experimental results are available for the reaction of H_2 and D_2 on Cu(111)[46–56]. For the non-copper systems discussed in this work experimental results are sparse[18,71], and there is discussion about the validity of the available parameters describing the molecular beams used in the experiments on H_2 (D_2) + Ag(111) and Pt(111)[20,61,65,66].

The good agreement between different molecular beam dissociative chemisorption experiments[46,47,52] on the reaction of H_2 (D_2) + Cu(111), and their resultant constraints for a to be developed SRP-DF, provides an opportunity to design the best performing SRP-DF for this system yet reported. The DF that best describes sticking probabilities obtained from dissociative chemisorption molecular beam experiments for H_2 (D_2) + Cu(111), will be considered the best performing DF. We choose this definition since our calculations are carried out using the BOSS model. From the literature it is known that the BOSS model

works rather well for activated H_2 dissociation on cold metals[24,28–30,63,149].

Comparisons to experimental results obtained from associative desorption experiments will not be included in the assessment of the quality of the newly constructed SRP-DFs for two reasons. The first reason is that associative desorption experiments are carried out at high surface temperatures. Since we have carried out calculations using the BOSS model we neglect surface temperature effects. The second reason is that in obtaining state-specific information from associative desorption experiments requires the assumption of detailed balance, which is strictly speaking not applicable if an electronically non-adiabatic process is involved and energy exchange with the surface is allowed. Since neither process can be ruled out we feel it safer to base our judgement on the sticking experiments. We still discuss the valuable experimental results on associative desorption since they do provide insight into the reaction dynamics. However, as we will discuss, it is fraught with difficulty to make a direct quantitative comparison between calculations on dissociative chemisorption and associative desorption experiments without improving our dynamical model by incorporating phonons and ehp excitations, which is challenging to do[150–152]. Recently, this has been done for H_2 + Cu(111)[76] using ab initio molecular dynamics with electronic friction (AIMDEF) calculations employing the PBE[116] DF. It is hard to draw firm conclusions from this work on the effect of electron-hole pair excitation as the statistical accuracy of the AIMDEF calculations is limited through the small number of AIMDEF trajectories. Other recent work employed the orbital dependent friction model (ODF)[23]. However the effects of incorporating ODF in the reaction dynamics of H_2 are small and require additional experiments for theoretical predictions to be verified[23] and for proving that ODF should be better.

5.4.1 Metal properties

Using a GGA DF for a theoretical description of gas surface dynamics is in most cases a compromise between a good description of the metal slab and a good description of the interaction of a molecule with the metal slab[153]. Table 5.5 shows the calculated lattice constants for all DFs investigated in this work. Highly accurate results are only achieved using PBEsol[118] and our previously developed mGGA MS-B86bl[13]. All our candidate SRP-DFs yield improved results over the vdW-DF1[97], vdW-DF2[98], and SRP48[11] DFs. We generally see a large improvement in the calculated lattice constant if a DF has at least one component with a μ value closer to the second gradient expansion $\mu = \frac{10}{81}$, as used in the PBEsol[118], MS-B86bl[13], SRPsol63-DF2 and the B86SRP68-DF2 DFs.

When looking at the relaxations of the interlayer distance of the two top most layers relative to the bulk interlayer distance (table 5.6) no clear trend can be discerned. The best performing DF is again MS-B86bl[13]. We do note that the SRP48 DF appears to produce top interlayer distances that on the whole are closer to the experimental values than DFs obtained combining GGA exchange DFs with vdW-DF2 non-local correlation. The reason for this is unclear.

5.4.2 Static PES properties

The experimental Van der Waals well depth that has been measured for H_2 + Cu(111)[60] can provide us with a constraint when fitting a new SRP-DF. The new SRP-DFs we present here are B86SRP68-DF2 and SRPsol63-DF2 (table 5.1). The two original Van der Waals DFs, namely vdW-DF1[97] and vdW-DF2[98], yield wells that are too deep, especially for vdW-DF1[97], as also found in earlier work[154] (figure 5.3b, see also table 5.11). The two previous SRP-DFs for this system produce a very tiny (SRP48[11]) or no (MS-B86bl[13]) Van der Waals well at all (figure 5.3b). Of the four DFs considered in figure 5.3b, the vdW-DF2[98] DF produces the best results. Other exploratory calculations carried out by us showed that using vdW-DF1[97] correlation yields Van der Waals wells that are much to deep and too close to the surface, although they are not shown here. The better performance of vdW-DF2 correlation is most likely due to the large-N asymptote correction used in this DF[98].

Figure 5.3a shows the same Van der Waals well depth for the SRP-DFs that include vdW-DF2 correlation, and one SRP-DF that includes vdW-DF1 correlation. These four DFs are all chemically accurate with respect to the reactivity of H_2 on Cu(111), as can be seen from the MAD values in figure 5.4. The PBEα57-DF2 DF has originally been fitted to reproduce experiments for H_2 (D_2) + Pt(111)[12], and the optPBE-DF1[115] DF has previously been shown to be chemically accurate H_2 (D_2) + Cu(111)[42]. The exchange part of the optPBE-DF1 DF was optimized to reduce intermediate range effects to avoid double counting when combining it with non-local vdW-DF1 correlation[115]. It is clear that the choice of exchange functional greatly impacts the depth and position of the Van der Waals well. The difference between the depths of the deepest and the shallowest Van der Waals well obtained with the non-standard DFs using vdW-DF2 non-local correlation[98] (figure 5.3a, 23.4 meV) is greater than the difference between the depths of the vdW-DF1 and vdW-DF2 wells (figure 5.3b, 13.4 meV, see also table 5.11). It can also be seen that going from PBEα57-DF2 to SRPsol63-DF2 the calculated Van der Waals well more closely

resembles experiment[60]. The closest agreement with experiment is achieved using the B86SRP68-DF2 DF.

All Van der Waals wells computed by us are tabulated in table 5.11, also comparing with experimental Van der Waals wells that have been reported for H_2 + Cu(111)[60,62], H_2 + Ag(111)[91], H_2 + Au(111)[62] and H_2 + Pt(111)[100,111]. With respect to the Cu(111) well depth the experimental results are in reasonable agreement with each other. However, the position reported by Harten et al.[62] is somewhat closer to the surface. This difference in the Z dependence of the Van der Waals well can be attributed to ambiguities in the bound state level assignments from the Feshbach resonances in the earlier experiment[105], and it has been remarked that the results obtained later[60] are in fact also consistent with the earlier measurements[105]. Additionally we suspect that the reported Van der Waals wells for H_2 + Ag(111)[91] and H_2 + Au(111)[62] might possibly be too close to the surface[105] for the same reason. This drawback of using the RMSA technique[99] might be alleviated by redoing the potential inversion on the basis of the original data on Feshbach resonances with more advanced theoretical models[155], e.g., using an analysis in which the molecule-surface potential is not laterally averaged. In yet a different approach, instead of using the RMSA approach[99] Poelsema et al.[111] presented a combined thermal energy atom scattering/thermal desorption spectroscopy (TEAS/TDS) study of the H_2 + Pt(111) system, obtaining Van der Waals well geometries that were subsequently accurately reproduced by theory[12]. For the H_2 + metal(111) systems studied here it would certainly be advantageous if additional experimental data were to become available addressing the Van der Waals interaction, using either a sophisticated analysis of results for RMSA studies or through combined TEAS/TDS studies. New experiments would allow for a better comparison between theory and experiment with respect to the predictions obtained by the inclusion of non-local correlation in DFT calculations on the systems addressed here.

5.4.3 Molecular beam sticking

Molecular beam sticking of H_2 (D_2) + Cu(111): QCT results

The fitting of the candidate SRP-DFs was done by reproducing six different sets of molecular beam experiments[46,47,52] for which the molecular beam parameters were taken from (the supporting information of) Refs[11,29]. Figure 5.4 compares results of three sets of molecular beam sticking probabilities, S_0, with results computed with the SRP48[11], B86SRP68-DF2, SRPsol63-DF2, PBEα57-DF2[12] and optPBE-DF1[42,118] DFs using the QCT method. We focus on these three sets of molecular beam experiments because for these enough experimental

data points are available to perform a cubic spline interpolation. The quality of the DFs is assessed by computing MAD values, i.e. the mean distance along the incidence energy axis from the computed S_0 data point to the interpolated experimental data point with the same S_0 value.

It is clear from the total MAD values that all DFs evaluated in figure 5.4 are chemically accurate with respect to the three sets of molecular beam experiments for H_2 (D_2) + Cu(111) shown in figure 5.4, and that the agreement between theory and experiment is good for all molecular beam conditions. The theoretical results shown here were obtained using the BOSS model. The experiments of Michelsen et al.[46] and Rettner et al.[54] considered here employed a low surface temperature of 120K, the experiment of Berger et al.[47] was reportedly done on a 'cold' surface, and from the literature it is known that the BOSS model works well for activated H_2 dissociation on cold metals[24,27–30]. Another advantage of fitting a SRP-DF to these sets of molecular beam experiments is that they cover both H_2 and D_2 for very different experimental conditions with respect to the nozzle temperature, the average collision energy, and the width of the velocity distributions[11].

The B86SRP68-DF2 DF exhibits a MAD of 1.4 kJ/mol for the experiments shown in figure 5.4, which is the lowest value obtained with the five DFs discussed. Of the DFs that include non-local correlation the B86SRP68-DF2 DF also performs best with respect to the calculated lattice constants, as can be seen in table 5.5. In addition it performs best with respect to the shape and depth of the Van der Waals well. We therefore select the B86SRP68-DF2 DF as the new, and most accurate, SRP-DF for the H_2 + Cu(111) system. From this point onward we will mainly focus on the results obtained with the newly selected B86SRP68-DF2 DF and the PBEα57-DF2[12] DF, and on how the performance of these two DFs compares to that of the original SRP48[11] DF and of our previously developed mGGA DFs[13].

One additional comparison to experiment is made in figure 5.5, concerning pure D_2 molecular beams[46]. This comparison highlights a limitation of assessing the quality of a candidate SRP-DF by computing the mean distance along the incidence energy axis from the computed S_0 value to interpolated experimental values. In this experiment the average translational energy does not monotonically increase with increasing nozzle temperature. Due to the high sensitivity of the sticking probability to the width of the velocity distribution of the molecular beam, the sticking probability also does not monotonically increase with the average translational energy. In figure 5.5 the application of our quality assessment strategy leads, in some cases, to large deviations with respect to the interpolated experimental results (note, however, that only for one data point and for one DF chemical accuracy was not achieved, see figure

5.5c). Our quality assessment strategy works best if the reactivity increases monotonically with increasing average translational energy.

Molecular beam sticking in H_2 + Cu(111): QD results

Due to the computational expense of calculating molecular beam sticking probabilities using the QD method we only carried out QD molecular beam simulations for H_2 + Cu(111) for the B86SRP68-DF2 DF (figures 5.4e,f and 5.6). We have used the same methodology to carry out QD molecular beam simulations as in Chapter 4. Overall, for the four experiments considered with both methods, the MAD value obtained with the the B86SRP68-DF2 DF increases from a QCT value of 1.3 kJ/mol to 1.6 kJ/mol for QD. In the QCT calculations more rovibrational states are taken into account compared to the QD calculations (see table 5.3). In figure 5.7 we explicitly compare QD and QCT results calculated from the same set of rovibrational states, and compare those results to the QCT results shown in figures 5.4e,f and 5.6. Overall the agreement between QD and QCT sticking probabilities is very good when both are calculated from the same set of initial rovibrational states. There are however small differences when looking at narrow low average translational energy molecular beams (see e.g. figure 5.7a).

Figures 5.7a,b show that for narrow low average translational energy molecular beams[52] the QD method predicts slightly larger sticking probabilities than the QCT sticking probabilities calculated from the same set of rovibrational states. This small gap between QD and QCT sticking probabilities based on the same set of initial rovibrational states is slightly bigger then what was obtained for H_2 + Cu(211) when using the SRP48 DF[37]. This suggests that quantum effects might play a role in the dynamics. It is possible that the slightly higher sticking probability predicted by QD is due to the underlying reaction probability curves for specific included rovibrational states showing more structure than for H_2 + Cu(211)[37]. Since the molecular beam sticking probabilities are very small in figures 5.7a,b, they could also be very sensitive to noise in the underlying reaction probability curves. We shall further discuss the differences between fully initial-state resolved QD and QCT reaction probabilities in section 5.4.6.

Figures 5.7c,d show very good agreement between QD and QCT results, also for the QCT results that were based on more initial rovibrational states. Only for the highest nozzle temperature points in figure 5.7c (see table 5.4) taking into account more initial rovibrational states in the QD than those listed in table 5.3 might be advisable. This is also the reason that QD now predicts a somewhat lower sticking probability than QCT in figure 5.4e. The

QD and QCT results based on the same set of initial rovibrational states in figure 5.7c,d are however in good agreement at these high nozzle temperature points, indicating that for all but the lowest average translational energies H_2 + Cu(111) is well described quasi-classically.

Note that for a nozzle temperature of 2000 K we take into account all rovibrational states that have a Boltzmann weight > 0.001. Highly excited rovibrational states, either with high ν, high J, or both, yield high reaction probabilities at low translational energies, therefor the effect of not taking into account these rovibrational states might be larger than expected from their Boltzmann weight. It is however computationally very expensive to take into account all initial rovibrational states that have a Boltzmann weight > 0.001 at a nozzle temperature of 2300K in the QD calculations, i.e. the nozzle temperature for the point in figures 5.7c where the QCT results and the QCT results based on the same, smaller, set of initial rovibrational states as the QD calculations diverge most. Doing this would nearly double the amount of wave packet calculations, and these additional calculations would also require larger basis sets.

Molecular beam sticking in D_2 + Pt(111)

Figure 5.9 shows a comparison of calculations on D_2 + Pt(111) to the molecular beam experiments of Luntz et al.[65]. The PBEα57-DF2 DF was originally fitted[12] in order to reproduce these experiments. In figure 5.9b we see that the B86SRP68-DF2 DF can also describe these experiments with overall chemical accuracy (MAD = 3.1 kJ/mol), although the agreement with experiment at low incidence energies is just shy of being chemically accurate, which would adversely affect the extraction of the minimum barrier height for this system. The SRP48 DF also describes the experiments with overall chemical accuracy, but at low E the agreement with experiment is really poor (figure 5.9c). The MS-PBEl DF does not agree with experiments to within overall chemical accuracy (figure 5.9d).

The discrepancy between theory and experiment at low incidence energies for the SRP48 and B86SRP68-DF2 DFs most likely arises because these DFs exhibit a too high early barrier to reaction at the top site minimum barrier geometry (see table 5.10). These two DFs also do not possess the double barrier structure for the t2b site that the PBEα57-DF2 DF predicts. The MS-PBEl functional does predict a double barrier structure for the t2b site. The early t2b barrier predicted by the MS-PBEl DF is however very high when compared to results obtained with the other DFs, which is most likely the root cause of its poor performance for this system.

The molecular beam experiments of Cao et al.[61] are not as well described by the B86SRP68-DF2 DF, as can be seen in figure 5.10. However we note that the increase of the MAD value in going from figure 5.9a to figure 5.10a is similar in size to what was reported for the PBEα57-DF2 DF[66] (see table 5.12). Earlier work from our group has shown that the experimental results of Luntz et al.[65] and Cao et al.[64] are in good agreement with each other for the lower incidence energies but somewhat diverge for the higher incidence energies[66]. The possible origins of the discrepancy between these two sets of experimental data are discussed in ref.[66]. There it was surmised that at high average incidence energies the reaction probabilities of Cao et al.[64] are most likely somewhat underestimated compared to the results of Luntz et al.[65] because the average incidence energies themselves are somewhat underestimated in the experiment of Cao et al.[61].

Molecular beam sticking in D_2 + Ag(111)

We now make a comparison to molecular beam experiments on D_2 + Ag(111)[147]. Even though silver is only one row below copper in the periodic table, the SRP48 DF that was fitted to reproduce experiments on Cu(111) was not able to describe experiments on Ag(111) with chemical accuracy[20]. Figure 5.8 shows the computed S_0 for D_2 + Ag(111). Hodgson and coworkers[147] have reported translational energy distributions that were symmetric in the energy domain. In our view, and as discussed in previous work from our group[20], the symmetric translational energy distributions are somewhat unphysical. Therefore we opted to use the molecular beam parameters of pure D_2 reacting on Cu(111) reported by Auerbach and coworkers[46], which likewise describe beams that are narrow in translational energy. Here we see that the PBEα57-DF2 and B86SRP68-DF2 DF are similar in accuracy to our previously developed MS-PBEl mGGA DF[13], and that these three DFs predict a reactivity just shy of chemical accuracy when compared to the molecular beam experiment of Hodgson and coworkers (see table 5.12). Note that the PBEα57-DF2 DF seems to perform worse than the other three DFs at the lowest translational energy. All three SRP-DFs yield an overall performance that is better than that of SRP48.

Although we are not yet able to describe the molecular beam experiment with chemical accuracy, the improvement of the DFs that include non-local correlation over the SRP48 DF again suggests that non-local correlation is an important ingredient for constructing SRP-DFs describing H_2 + metal systems that incorporate GGA exchange. The MS-PBEl mGGA[13] does not include non-local correlation but performs similarly well as the GGA based SRP-DFs

that do include non-local correlation. As will be shown in Chapter 6, further improvement is possible by adding non-local correlation to the MS-PBEl DF.

5.4.4 Associative desorption

Comparing to experimental $\mathbf{E}_0(\nu, J)$ parameters

When comparing to experimental $E_0(\nu, J)$ parameters by calculating $E_{1/2}(\nu, J)$ parameters from calculated degeneracy averaged reaction probabilities we effectively try to model an associative desorption experiment as an initial-state resolved dissociative chemisorption experiment. Additionally our QCT results are obtained using the BOSS model, while the associative desorption experiments necessitate high surface temperatures. The J dependence of the calculated $E_{1/2}(\nu, J)$ parameters is a measure of how accurate the reactivity of the individual rovibrational states is described relative to each other. The trend is here to be understood as the dependence of the $E_0(\nu, J)$ parameters on J, which we can visualize using a third degree polynomial fit to the calculated results (see e.g. figure 5.16).

In this work we have not included MDEF calculations in which the effect of ehp excitations is modeled as a classical friction force. In our previous work[37] the MDEF method shifted the $E_{1/2}(\nu, J)$ parameters to slightly higher values since, again, we model an associative desorption experiment using a dissociative chemisorption calculations. Including the effect of ehp excitations in the dynamics here then has a similar effect in both cases, and shifts the $E_{1/2}(\nu, J)$ parameters to slightly higher energies. However, as mentioned in our previous work[37], if ehp excitations are important then assuming detailed balance to extract degeneracy averaged reaction probability curves is, strictly speaking, not correct. More specifically, we would expect that if we applied electronic friction to the simulation of an associative desorption experiment in the manner discussed here, the predicted translational energy distributions would shift to higher energies as opposed to lower energies as expected in a direct simulation of associative desorption. In other words: extracting $E_{1/2}(\nu, J)$ parameters from dissociative chemisorption calculations applying electronic friction would shift our $E_{1/2}(\nu, J)$ parameters to higher energies instead of the expected lower energies, because the effective barrier for dissociative chemisorption would go up. However, we note that the MDEF calculations in our previous work[37] only shifted the trend in $E_{1/2}(\nu, J)$ parameters to slightly higher values on the energy axis and did not influence the observed trend in their J-dependence. This is in accordance with very recent direct simulations of associative desorption of H_2 from Cu(111)[76] using AIMD and AIMDEF calculations and the PBE DF,

which find little effect of ehp excitations modeled at the local density friction approximation (LDFA)[156] level.

In section 5.4.9 we will further discuss how a combined analysis of dissociative chemisorption and associative desorption experiments might be used in the future to determine a possible fingerprint of non-adiabatic effects.

$E_{1/2}(\nu, J)$ parameters Cu(111) The comparison of the measured $E_0(\nu, J)$ parameter values with the $E_{1/2}(\nu, J)$ parameters computed using method B1 is shown in figure 5.15. The $E_{\max}(\nu, J)$ parameters needed in this method (see Eq. 5.16) were taken from Tables S4 and S6 of Ref.[48]. The comparison of the experimental $E_0(\nu, J)$ parameters with theoretical $E_{1/2}(\nu, J)$ parameters extracted using method A1 is presented in figure 5.14. In this method we used A = 0.325 for H_2 and A = 0.513 for D_2, as obtained in Ref[48].

Table 5.13 presents MAD and MSD values obtained with both methods. The following conclusions can be drawn: for almost all DFs method A1 (based fully on experiments) yields the lowest MAD and MSD values. The only exception occurs for H_2 + Cu(111) when using the SRP48 DF, for which method B1 gives a lower MAD value (41 meV), although the difference with method A1 (43 meV) is quite small. From this point of view, method A1 works better.

The use of method A1 for H_2 would seem to yield conclusions that are more consistent with the conclusions from the comparisons of the sticking probabilities. Specifically, the mGGA DF and the DFs containing non-local van der Waals correlation all perform better than SRP48 DF for H_2. Nonetheless, SRP48 performs best for D_2, regardless of whether method A1 or B1 is used. We also note that the better behavior of the other DFs in procedure A1 is to some extent suspect due to the rather low A value employed for H_2 (0.325). This A value is much lower than the A value extracted for D_2 in method A1 (0.513). This may well be a simple artifact resulting from the method followed: the A value determined for D_2 is likely to be more accurate because the sticking experiments were done for a kinetic energy up to 0.83 eV[46], whereas the sticking experiments for H_2 only went up to about 0.5 eV[52]. This suggest that the A-value for D_2 (figure 5.B.1c) is much more accurate than for H_2 (figure 5.B.1a), and it is not clear why the A value for H_2 should differ much from it. Furthermore, the A value established for H_2 in method A1 is much lower than the A-values established for H_2 in method B1 (see also figure 5.B.1a and 5.B.1c), while for D_2 the A values extracted with the two methods resemble each other, and the A values extracted with method B1 for H_2, much more (see figure 5.B.1b, 5.B.1c and 5.B.1d).

Finally, we note at this stage that the $E_{1/2}(\nu, J)$ parameters computed using method A1 do, in general, not reproduce the subtle trend found experimentally

that the $E_0(\nu, J)$ parameters first increase somewhat with J (see figure 5.14) (attributed to rotational hindering[46,48,52]).

The $E_{1/2}(\nu, J)$ parameters calculated using method B1 (especially the ones calculated with DFs incorporating non-local Van der Waals correlation) better reproduce this subtle rotational hindering effect (figure 5.15). The reasonable performance of method B1 is also clear from figure 5.16, which presents a third degree polynomial fit to the $E_{1/2}(\nu, J)$ parameters as a function of J obtained using the B1 method. The polynomial fits are shown without the energy axis offset. DFs that include non-local correlation reproduce the subtle rotational hindering effect, DFs that do not include non-local correlation do not or hardly show rotational hindering. Additionally, for H_2, the agreement with the experimental dependence of the $E_0(\nu, J)$ parameters on J improves when using the QD method for vibrationally exited molecules.

That DFs including non-local correlation better reproduce the subtle rotational hindering effect with the use of method B1 is wholly due to the rovibrational state dependence of the $E_{\max}(\nu, J)$ parameters. The extracted degeneracy averaged reaction probabilities in fact monotonically increase with increasing J (figure 5.12), and this is true for all DFs used in this work. Reproducing rotational hindering based on these degeracy averaged reaction probability curves is therefore not possible when selecting the same A value for all rovibrational states, as done with method A1.

The $E_{1/2}(\nu, J)$ parameters calculated using both method A1 and B1 do reproduce the clear trend (figures 5.14 and 5.15) that at high J the $E_0(\nu, J)$ parameters decrease with J (attributed to energy transfer from rotation to the reaction coordinate as the rotational constant decreases when the molecule stretches to reach the dissociation barrier[26,37,129]).

We are aware of one single PES that does reproduce the rotational hindering effect as observed in the experiment, namely the LEPS PES[40] used by Dai et al.[38] for six-dimensional QD calculations. As discussed in appendix 5.C, we have investigated whether the rotational hindering observed by Dai et al.[38] could be due to their QD calculations being unconverged. We find that this is not the case, but that the observed difference with our calculations using the best SRP-DF (B86SRP68-DF2) only arises for $J < 3$, suggesting that the rotational hindering effect is very subtle (see figure 5.C.1). Further research is needed to check whether the difference between the calculations could be due to the LEPS fit[40] being inaccurate, the underlying electronic structure calculations being unconverged[40,41], or both. See appendix 5.C for further details.

Reported density functional molecular dynamics (DFMD) calculations that include surface motion have shown that at low translational energies surface temperature effects somewhat increase the reactivity of D_2 reacting on

Cu(111)[24,63]. Increased reactivity at low translational energies might lower calculated $E_{1/2}(\nu, J)$ parameters for both methods A1 and B1. We have extracted $E_{1/2}(\nu, J)$ parameters using both methods A1 and B1 from Nattino et al.[63]. The results are shown in figure 5.23. The reported data was obtained using the SRP48 DF[63]. There were only three rovibrational states for which a data point was available at a translational energy higher than the maximum kinetic energy sensitivity of the experiment[48]. To validate the obtained $E_{1/2}(\nu, J)$ parameters we have also extracted $E_{1/2}(\nu, J)$ parameters using the same methodology for the reported logistics function fits to BOSS direct dynamics data[63]. The good agreement for both methods A1 and B1 between our SRP48 $E_{1/2}(\nu, J)$ parameters and those obtained from logistics function fits to BOSS direct dynamics data validates this comparison. For both the A1 and B1 method the single point for $(\nu = 0, J = 11)$ suggests that a small decrease can be expected from allowing the surface to move, for the $(\nu = 1, J = 6)$ point this is not so clear. There is however a dramatic decrease of the $E_{1/2}(\nu, J)$ parameter for $(\nu = 1, J = 4)$. This is a clear indication that, at least for low J, taking into account surface motion leads to lower $E_{1/2}(\nu, J)$ parameters, and this might thus be partly responsible for the observed rotational hindering. The decrease of the $E_{1/2}(\nu = 1, J = 4)$ value with the introduction of surface motion is less pronounced when using the A1 method.

Note however that the $E_0(\nu, J)$ parameters are extremely sensitive to the quality of the logistics function fits. The agreement between our SRP48 $E_{1/2}(\nu, J)$ parameters and those obtained from logistics function fits to BOSS direct dynamics for which no data point existed at a translational energy higher then the maximum kinetic energy sensitivity to which the experiment was sensitive was not so good.

The above observations warrant the following tentative conclusions: within the BOSS approximation, the mGGA DF and the DFs containing non-local correlation perform best for sticking. However, assuming method B1 to be best, the SRP48 performs best for associative desorption. For associative desorption and again within the BOSS approximation, the two different methods (A1 and B1) for extracting the $E_{1/2}(\nu, J)$ parameters describing the reaction probabilities extracted from associative desorption experiments yield rather different results. It follows that, at this stage, the associative desorption experiments are not as useful as the sticking experiments for assessing the accuracy of theory. Hopefully this can be changed in future by taking into account surface atom motion and ehp excitation in the theory, and by computing associative desorption fluxes directly from theory, as was recently done using the PBE DF by Galparsoro et al.[76].

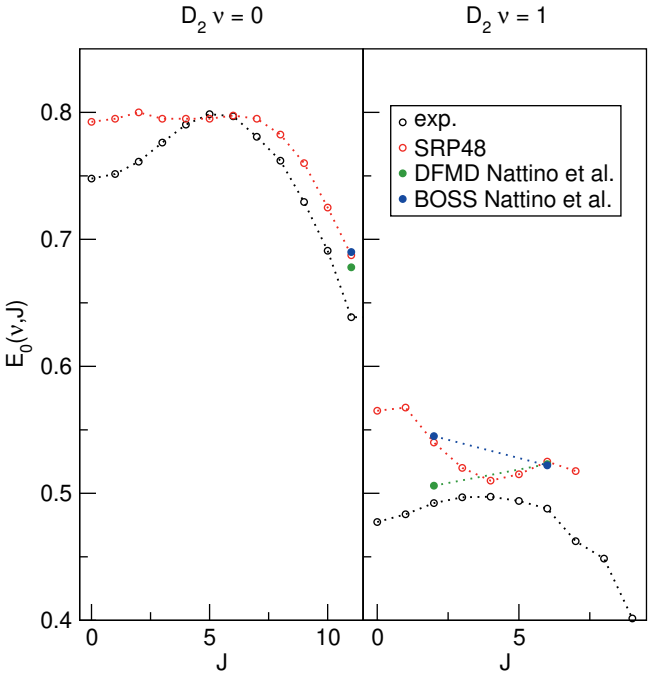

FIGURE 5.23: $E_{1/2}(\nu, J)$ parameters as a function of J for D_2 reacting on Cu(111). Closed symbols pertain to $E_{1/2}(\nu, J)$ parameters calculated using the A1 method, open symbols refer to the B1 method. Experimental results are shown in black[48], SRP48 results calculated in this work are shown in red. DFMD (green) and BOSS (blue) results obtained using the SRP48 DF have been extracted from ref.[63]

$E_{1/2}(\nu, J)$ parameters Au(111) The comparison of the measured $E_0(\nu, J)$ values with the $E_{1/2}(\nu, J)$ parameters computed using method B2 is shown in figure 5.17. The $E_{\max}(\nu, J)$ parameters needed in this method (see Eq. 5.16) have been obtained from a private communication[148], and have been plotted in figure 5.B.2 against the $E_0(\nu, J)$ parameters extracted from the measurements[71]. We note that the $E_{\max}(\nu, J)$ parameters typically equal $E_0(\nu, J) + \frac{1}{3}W$ for the $\nu = 0$ states and $E_0(\nu, J) + \frac{2}{3}W$ for the $\nu = 1$ states, where $W = 0.31$ eV for $\nu = 0$ and 0.29 eV for $\nu = 1$[71] (see figure 5.B.2). This means that method B1 will yield unreliable values for the $E_{1/2}(\nu, J)$ parameters. It also means that method B2 relies heavily on extrapolation in the method to determine the A values by anchoring the measured reaction probabilities to the reaction probabilities computed at $E_{\max}(\nu, J)$. One should therefore exercise extreme caution when comparing the theory to experiment.

Table 5.13 shows the MAD end MSD values obtained with method B2 for H_2 + Au(111). The following tentative conclusions can be drawn: the $E_{1/2}(\nu, J)$ parameters computed with the mGGA DF tested here and with all DFs employing Van der Waals correlation substantially overestimate the measured $E_0(\nu, J)$ parameters, with MAD values of approximately 0.1 eV for H_2. The PBE DF would appear to perform best, with a MAD value of 46 meV for H_2. This conclusions agrees with the observation that PBE reaction probabilities[145] allowed better fits of the measured time-of-flight spectra of H_2 and D_2 desorbing from Au(111)[71] than the SRP48 reaction probabilities.

A caveat here is that the experiment was performed with a surface temperature of 1063K, while all calculations were performed using the BOSS model. Allowing surface motion during the dynamics would lead to broadening of the sticking probability curves[24,30,157,158]. A higher sticking probability at lower translational energies could potentially lower the theoretical $E_{1/2}(\nu, J)$ parameters. Additionally, we have performed our calculations on an unreconstructed Au(111) surface because the surface unit cell of reconstructed Au(111) is at present too big to map out a full PES using DFT calculations. Earlier work in our group indicated that the barriers to H_2 dissociation are somewhat higher on the reconstructed Au(111) surface and that using an unreconstructed surface might lead to the underestimation of dynamical barrier heights by about 50 meV ($\sim$1 kcal/mol)[145], which would lead to slightly higher $E_{1/2}(\nu, J)$ parameters and therefore to increased disagreement with the measured values.

We are not able to resolve the contradiction posed by Shuai et al.[71] that the vibrational efficacies computed with the SRP48 DF are in good agreement with experiment (as may be derived from figure 5.17) but that the ratio of desorbed molecules in the vibrational ground state versus the vibrationally excited state is not (see table 5.14). The good reproduction of the J dependence of the

$E_0(\nu, J)$ parameters by theory (figure 5.17) suggests that the reactivity of the individual rovibrational states relative to each other is accurately described by theory as long as states are considered with the same vibrational level. Previously reported experiments implied that the recombination of H_2 on Au(111) is coupled to the electronic degrees of freedom of the metal[159–162]. In line with Shuai et al.[71] we think that non-adiabatic effects together with surface motion effects and surface reconstruction represent the most likely causes for the lower translational energy distributions of the desorbing H_2 ($\nu = 0$) molecules compared to theory. If molecular beam dissociative chemisorption experiments on a reasonably cold surface would become available for this system (like for H_2 + Ag(111)) this would allow for a more direct comparison to experiment of QCT and MDEF calculations. Molecular beam adsorption experiments would also allow us to check if the absolute reactivity predicted by the DFs shown here is in agreement with experiment. Therefore, at present, we cannot corroborate or refute the conclusion reached by Shuai et al.[71], namely that the experimentally observed lower translational energy distributions compared to theoretical predictions (see figure 1 of Shuai et al.[71]) is most likely due to ehp excitations in the desorption dynamics.

Rovibrational state populations of H_2 and D_2 desorbing from Au(111).

Figure 5.21 shows the rovibrational state populations of H_2 and D_2 desorbing from Au(111). Note that we have consistently applied the normalization procedure outlined by Eq. 5.14 to the objects shown in figure 5.21. In the case of ($\nu = 0$) the populations deviate from the slope set by the Boltzmann distributions at the surface temperature of 1063 K indicating that rotationally excited molecules are more likely to adsorb[71]. The populations of vibrationally excited molecules also lie on gentler slope than implied by the Boltzmann distribution and are consistenly higher than would be obtained with the Boltzmann distribution indicating that vibrationally excited molecules are more likely to adsorb. Both these observations are in line with the Polanyi rules for a late barrier system like H_2 + Au(111)[163,164].

Figure 5.22 shows the state distributions of molecules desorbing from Au(111) as reported by Shuai et al.[71] in their figure 2 together with experimental results calculated by us using Eq. 5.13, an upper integration limit of 5 eV, and our normalization procedure, which were the boundary conditions and integration parameters suggested to us by Shuai *et al.*[71,148] As can be seen from figure 5.22 our "experimental results" calculated using Eq. 5.13 and the error function fits reported in Ref.[71] are in good agreement with the experimental results reported by Shuai et al.[71], i.e. the calculated curves have the correct shape and

can be mostly superimposed on one another, provided that they are shifted by a constant value as explained in the caption of figure 5.22. However, we are not able to reproduce the results of Shuai et al.[71] with the normalization strategy they employed[71]. Also when we shift the SRP48 ($\nu = 0$) and ($\nu = 1$) curves by the same value we cannot exactly superimpose our results on their computed SRP48 results for both vibrational states simultaneously. It is not clear to us how this discrepancy arises.

The relative populations for the ($\nu = 0$) and ($\nu = 1$) rovibrational states is not affected by this discrepancy. The difference between our work and Shuai et al.[71] with respect to the $\nu = 1 : \nu = 0$ ratios arises because we use $E_{\max}(\nu, J)$ as the upper integration limit in Eq. 5.13. Shuai et al.[71] have used 5 eV as the upper integration limit[148]. The only reason we choose $E_{\max}(\nu, J)$ as the upper integration boundary is because the reported error function fits are only reliable below $E_{\max}(\nu, J)$, for some rovibrational states the error function fits can yield sticking probabilities much larger than unity for high kinetic energies. The ratios we calculate are shown in table 5.14. We note that when we use the upper integration limit of 5 eV, we reproduce the $\nu = 1 : \nu = 0$ ratios reported by Shuai et al.[71]. In our view only integrating up to $E_{\max}(\nu, J)$ is a more fair way of calculating the $N(\nu, J)$ populations, though on the scale of figure 5.21 the difference between integrating to $E_{\max}(\nu, J)$ or 5 eV would not be visible. Note that the overwhelming majority of the area under the Gaussian fits to the time-of-flight curves, as reported in tables S1-4 of Ref.[71], lies well below $E_{\max}(\nu, J)$. Note also that we calculate the $\nu = 1 : \nu = 0$ ratios only using the rovibrational states shown in figure 5.21, which is the same set of rovibrational states used by Shuai et al.[71].

In figure 5.21 the difference between the desorbing populations computed with the SRP48 and B86SRP68-DF2 DFs is minimal. The agreement between theory and experiment is best for D_2, although the qualitative agreement between theory and experiment is reasonable for both H_2 and D_2. It can be seen in table 5.14 that there is only a reasonable agreement for D_2 with respect to the $\nu = 1 : \nu = 0$ population ratios. The theoretical $\nu = 1 : \nu = 0$ population ratio for H_2 is however too low, a result similar to what was reported by Shuai et al.[71]. The difference between theory and experiment can perhaps be explained by the experimental time-of-flight distributions being much broader than the theoretical ones, see figure 1 of Ref.[71] Taking into account surface motion in the theoretical calculations might well improve the agreement with experiment with respect to both the rovibrational state distributions of desorbing molecules as well as the $\nu = 1 : \nu = 0$ population ratio.

Initial-state resolved reaction probabilities for D_2 + Ag(111).

In the case of molecular beam sticking results for D_2 + Ag(111) the MS-PBEl functional performed similarly well as the GGA-exchange based SRP-DFs that include non-local correlation even though the barriers obtained with the DFs including vdW-DF2 correlation are higher (see table 5.8). This is most likely due to the slightly earlier barriers to reaction predicted by the MS-PBEl DF, leading to less promotion of reaction by vibrationally excited H_2[13] as obtained with the DFs including vdW-DF2 correlation, as expected from the Polanyi rules[163,164]. From this argument it follows that although the molecular beam sticking probabilities are similar the reactivity of individual rovibrational states should be different.

In figure 5.13 we see that, especially for D_2, the MS-PBEl mGGA DF has the best agreement with the initial-state selected reaction probabilities extracted from the associative desorption experiments. The good performance of the MS-PBEl DF for $\nu = 0$ and $\nu = 1$ can be explained by the slightly lower and earlier barriers, as discussed in our previous work[13]. The DFs that include non-local correlation do not show such a large improvement over the SRP48 DF, while they do for sticking.

Without new experimental work for this system, especially molecular beam experiments covering a wide range of translational energies and nozzle temperatures, it will be difficult to further improve the theoretical description of this system. Additional experiments (e.g. a molecular beam sticking experiment on D_2 seeded in H_2 and going up to a translational energy of 0.8 eV as done for H_2 + Cu(111)[46]) would also allow us to assess more accurately if the dynamics predicted by the MS-PBEl mGGA or the dynamics predicted by the GGA based SRP-DFs that do and do not include non-local correlation are more in line with experimental observations.

Rotational quadrupole alignment parameters: H_2 + Cu(111).

In figure 5.18 we compare calculated rotational quadrupole alignment parameters for D_2 to experimental ones measured for D_2 desorbing from Cu(111)[50]. We observe only a monotonic increase of the rotational quadrupole alignment parameters with decreasing translational energy, indicating that at translational energies close to the reaction threshold molecules prefer to react in a parallel orientation. This is in line with what has been reported in the literature for H_2 and D_2 associatively desorbing from Cu(111)[27,50] and Cu(100)[19,26], and can be explained by invoking a static effect of orientational hindering in which rotating molecules scatter when their initial orientation does not conform to

the lowest barrier geometry[26]. With increasing translational energy the rotational quadrupole alignment parameter approaches zero since all molecules, irrespective of their orientation, will have enough energy to react[50]. The experimental trend is reproduced by all DFs shown in figure 5.18a and b, though the calculated values are higher than the experimental values. The theoretical results presented here have been obtained within the BOSS approximation. Nattino et al.[27] have shown that incorporating surface motion in the dynamics using the DFMD technique leads to better agreement with experiment, for D_2 + Cu(111).

Note that the B86SRP68-DF2, PBEα57-DF2[12] and MS-B86bl[13] DFs are in good agreement with each other for both the $(\nu = 0, J = 11)$ state (figure 5.18a) and the $(\nu = 1, J = 6)$ state (figure 5.18b), but that these three DFs predict slightly higher rotational quadrupole alignment parameters than the SRP48 DF[27]. Given that the SRP48 rotational quadrupole alignment parameters were decreased, but still somewhat too large when surface atom motion was introduced[27], the present results suggest that the SRP48 DF yields the best description of this observable.

5.4.5 Inelastic scattering of H_2 from Cu(111)

In this section we will discuss inelastic scattering results for H_2, obtained with QD. We start with the vibrationally inelastic scattering results for H_2 shown in figure 5.19. We specifically show QD results since the previously voiced expectation that vibrationally inelastic scattering should be well described using the QCT method for translational energies above the lowest barrier to reaction[165] has been shown not to hold[25]. Here we discuss the inelastic scattering probability $P(\nu = 0, J \rightarrow \nu = 1, J = 3)$ for three different initial J states. Panels a and b suggest that for $(J = 1)$ and $(J = 3)$ and for the DFs that use non-local correlation the vibrationally inelastic scattering probability is correlated with the depth of the Van der Waals well (see table 5.11). A deeper Van der Waals well is correlated with higher vibrationally inelastic scattering probabilities. Figure 5.19c shows that for $(J = 5)$ all DFs yield vibrational excitation probabilities in reasonable agreement with each other. Bringing TOF spectra for vibrational excitation from $(\nu = 0, J)$ to $(\nu = 1, J = 3)$ in better agreement with experimental results would require a substantial increase of the vibrational excitation probabilities computed with the SRP48 DF (by a factor of 2-3)[25,165], which is obtained with non of the DFs tested. We conclude that better agreement with experiment probably requires a different dynamical model, as suggested also by earlier work[25,165].

From the computed ratio of rotationally inelastic scattering probabilities $P(\nu = 1, J = 0 \rightarrow \nu = 1, J = 2)/P(\nu = 1, J = 0 \rightarrow \nu = 1, J = 0)$ shown in figure 5.20 it is clear that the B86SRP68-DF2 DF performs not as well as the SRP48 DF[11]. The shifted SRP48 curve follows the experiment more closely. Both curves need to be shifted by 40 meV in order to better overlap with the experiment performed using a surface temperature of 300 K[55]. The overlap with experiment of the shifted curves only holds until 0.14 eV, but the experimentalists noted that at higher energies the measurements became more difficult[55]. It is rather surprising that both computed ratios need to be shifted by roughly the same amount in order to overlap with experiment, since the SRP48 DF overestimates the initial sticking probability in molecular beam experiment while the B86SRP68-DF2 DF does not. From the literature it is also known that including surface motion during the dynamics might lead to broadening, and an earlier onset, of inelastic scattering probabilities[24,30]. We speculate that allowing surface motion and ehp excitation during the dynamics might obviate the need for the shift in order to superimpose the calculated curves with experiment.

5.4.6 QD vs. QCT for H_2 + Cu(111)

In figure 5.11 initial state-resolved reaction probabilities are shown calculated using the B86SRP68-DF2 DF. Here the $(J = 0)$ and $(J = 1)$ state for both the vibrational ground state and the first vibrationally excited state are shown because the differences between the QD and QCT method are most prevalent for the low lying rotational states. The QD reaction probability curves show more structure than was shown for H_2 + Cu(211)[37] in Chapter 4, but the agreement between the QD and QCT method for degeneracy averaged reaction probabilities (figure 5.11a and c) is still very good. From the comparison between QD and QCT degeneracy averaged reaction probabilities shown in figure 5.12 it can be seen that the differences between the QD and QCT method get smaller with increasing J for $J > 3$, though small differences remain even for high J states.

The biggest difference between the QD and QCT method are observed in figure 5.11b. Here we show fully initial-state resolved reaction probabilities, thereby distinguishing between 'cartwheeling' molecules rotating in a plane parallel to the surface normal ($m_J = 0$) and 'helicoptering' molecules rotating in a plane perpendicular to the surface normal. In line with our previous work presented in Chapter 4, we observe that QD predicts a slightly larger preference for molecules reacting parallel to the surface. The rovibrational states shown in figure 5.11 are the same rovibrational states shown in figure 4.2 of Chapter

4, in which the agreement for degeneracy averaged reaction probabilities was nearly perfect.

In recent experimental work Kaufmann et al.[48] have reported a previously unobserved "slow reaction channel" for H_2 associatively desorbing from Cu(111) and Cu(211). In this channel, the reaction could be facilitated by trapping on the surface and distortion of the surface due to thermal motion forming a reactive site[48]. Even though our PES now contains a Van der Waals well that might facilitate trapping during the reaction dynamics, we do not yet see evidence of the recently reported slow reaction channel for H_2 + Cu(111)[48]. The translational energy range used in our calculations overlaps with the translational energies at which the slow channel reactivity was observed[48]. We can therefore rule out quantum effects (like tunneling, see Chapter 4) during the dynamics as the origin of this slow reaction channel for H_2 + Cu(111), as we did before for H_2 + Cu(211)[37]. We therefore propose, as done earlier for H_2 + Cu(211)[37], that the slow reaction channel reported by Kaufmann et al.[48] originates from the very high surface temperature of 923K used in the associative desorption experiments. Presently it is not possible to take surface motion explicitly into account in QD calculations, and it is challenging to do so in QCT calculations[150–152]. Galparsoro et al.[76] likewise did not yet find evidence for the slow reaction channel in their AIMD calculations.

5.4.7 Overall description of systems

When looking at the H_2 + Ag(111) and H_2 + Au(111) systems considered in this work together, one stark realization is that further development of chemically accurate DFs for H_2 reacting on transition metal surfaces is still heavily stymied by a lack of experimental data. This is bad news as presently semi-empirical DFT seems to be the only path to extracting chemically accurate information on barriers to reaction. Relying on non-empirical constraints on DF design is not yet feasible, as illustrated by the poor performance of the SCAN[166] DF for H_2 + Cu(111)[13] (see figure 3.11 of Chapter 3). Additionally, taking another step upwards on Jacob's ladder from a GGA or mGGA towards hybrid DFs is computationally very expensive, if not prohibitively so[167]. Furthermore, recent quantum Monte-Carlo (QMC) calculations on H_2 + Cu(111)[15] underestimate the barrier height for this system by more than 1 kcal/mol while dynamics results on O_2 + Al(111) based on a PES obtained with density functional embedded correlated wave function theory showed promising chemically accurate results with respect to the obtained sticking probability[168]. Furthermore, it would be expensive to extend this electronic structure method to sticking of molecules on transition metal surfaces.

For both the activated and non-activated reactions of H_2 on transitions metals there is now only a single well studied system, namely H_2 + Cu(111) (and maybe H_2 + Pt(111)[66]). What we mean by well studied is that there should be different kinds of well described experiments. For example, a combination of an associative desorption experiment and a dissociative chemisorption experiment should be available, or sticking probabilities for normal and off-normal incidence. It is also critical that the experimental conditions are described accurately.[16,20,21,65,66,145]

Without new and detailed experiments on, at least, the related H_2 + Pd(111) and H_2 + Ag(111) or H_2 + Au(111) systems it is not possible to grasp the overarching trends in reactivity imposed by the position of these metals in the periodic table. In many aspects we are dancing in the dark with respect to DF design. The consequence of this is that, presently, theory can only provide models with limited predictive power.

H_2 (D_2) + Cu(111)

The H_2 + Cu(111) system is the best described system of the ones treated here. Low surface temperature molecular beam sticking experiments are very accurately described using the BOSS model. The associative desorption experiments are however less well described by the new SRP-DFs that have been designed to reproduce low surface temperature molecular beam experiments with calculations using the BOSS model. $E_{1/2}(\nu, J)$ parameters obtained from reported DFMD data[63] suggest that, at least for this system, better agreement with experiment can be attained by including the surface degrees of freedom in the dynamics. It also appears that the agreement with $E_0(\nu, J)$ parameters measured in an associative desorption experiment is also increased for vibrationally excited molecules when using the QD method.

The large amount of published experimental studies[46–62,169,170] and theoretical work[11,13,19,22–45,157,171,172] have allowed us to get the best description of this system so far. We can however not yet point to one DF that is clearly the best DF for this system. Currently two DFs compete for being the best DF for this system, namely B86SRP68-DF2 and MS-B86bl[13]. The latter has a beter description of the metal and might therefor be better when looking at diffraction probabilities. The MS-B86bl DF however misses any description of Van der Waals forces. In all our simulations for the H_2 + Cu(111) system the B86SRP68-DF2 and MS-B86bl DFs perform similarly well. With the information available now one might argue that the MS-B86bl DF is the best DF for this system since its description of the metal is much better than provided by the B86SRP68-DF2 DF, and because the effect of including non-local correlation

is only apparent when calculating $E_{1/2}(\nu, J)$ parameters for this system. The MS-B86bl DF is however not transferable to weakly activated systems like H_2 + Pt(111). In our view, the DFs that are more generally applicable, i.e. the B86SRP68-DF2 and PBEα57-DF2 DFs, are currently the best DFs. A good next step could be to use non-local correlation together with the MS-B86bl DF, as discussed in Chapter 6.

D_2 + Ag(111)

For the D_2 + Ag(111) system it is more difficult to assess the quality of our theoretical description due to the lack of well defined molecular beam parameters[20]. DFs that use GGA-exchange and non-local correlation, and the MS-PBEl DF predict roughly similar molecular beam sticking probabilities. The comparison to the initial-state resolved reaction probabilities suggests that the MS-PBEl DF performs best due to its slightly lower and earlier barriers[13]. Since the MS-PBEl DF has a better description of the metal, a better description of the initial-state resolved reaction probabilities, and performs similar to the other candidate SRP-DFs concerning molecular beam sticking, one might argue that the MS-PBEl DF is currently the best DF for this system. As said before, the best DF should also exhibit transferability. Therefore we suggest, with some hesitation, that the B86SRP68-DF2 DF is the best DF at the moment for the H_2 + Ag(111) system. However, as will become clear in Chapter 6, the sticking in D_2 + Ag(111) can be described with chemical accuracy using the MS-PBEl-rVV10 DF. More and better defined experiments will allow us to refine our description of this system.

H_2 (D_2) + Au(111)

With respect to the H_2 + Au(111) system we cannot with certainty assess the quality of any of the DFs tested here. Based on the good reproduction of the experimental trend in $E_{1/2}(\nu, J)$ parameters and the reasonable agreement between theory and experiment with respect to the state distributions of desorbing molecules, we can infer that the reactivity of the rovibrational states relative to each other is described reasonably well. We cannot say anything about the accuracy of the barriers without additional experiments or improvements in our dynamical model that will allow us to disentangle the effects of surface temperature, surface reconstruction and ehp excitations (see section 5.4.9).

Shuai et al.[71] suggested that the PBE DF is better then the SRP48 DF because calculated time-of-flight distributions correlated slightly less worse with experimental observations for the PBE DF. This assertion implicitly assumes the validity of detailed balance for this system. The main conclusion of the

experimentalists was however that the bad agreement between theory and experiment points toward strong non-adiabatic effects, which, if true, would invalidate the assumption of detailed balance[71].

D_2 + Pt(111)

Ghassemi et al.[12] have previously designed a SRP-DF for the D_2 + Pt(111) system. Although the B86SRP68-DF2 DF could describe the experiments of Luntz et al.[65] to within chemical accuracy, the description of the experiments of Cao et al.[61] was not as good. As was the case for the H_2 + Ag(111) system there is some discussion about molecular beam parameters describing different experiments, but the experiments are in reasonably good agreement with each other[66]. Overall this system is best described by the PBEα57-DF2 DF that was specifically designed for this system[12].

5.4.8 Transferability

So far SRP-DFs fitted to reproduce molecular beam sticking experiments on H_2 and D_2 dissociating on noble metal surfaces where shown to be transferable among systems in which H_2 interacts with different crystal faces of the same metal[18,19], but not among systems in which H_2 interacts with surfaces of different metals[20,21]. Here we show examples in which a SRP-DF that was fitted to reproduce molecular beam sticking experiments on the activated late barrier system of H_2 reacting on Cu(111) can also describe the non-activated early barrier system of D_2 reacting on Pt(111) with chemical accuracy, and vice versa. Transferability to a different substrate of a SRP-DF fitted to reproduce gas-surface experiments has so far only been reported for CH_4 dissociation on Ni(111)[14] to CH_4 dissociation on Pt(111)[17].

The SRP48 DF for H_2 + Cu(111) is not transferable to the H_2 + Ag(111) system[20] or to the H_2 + Pt(111) system. We have previously shown that a SRP-DF based on the mGGA that does not include non-local correlation (MS-PBEl[13]) greatly improves the transferability from H_2 + Cu(111) to H_2 + Ag(111)[13], but figure 5.9 shows that this DF is not transferable to the weakly activated H_2 + Pt(111) system.

The only group of DFs that might be considered transferable between both highly activated and weakly activated systems are DFs that include non-local correlation. We demonstrated that a SRP-DF fitted to H_2 + Pt(111), PBEα57-DF2[12], can describe H_2 + Cu(111) with overall chemical accuracy and that a new SRP-DF fitted to H_2 + Cu(111), B86SRP68-DF2, can describe the D_2 + Pt(111) experiments of Luntz et al.[65] with chemical accuracy. We speculate that the transferability between the Cu(111) and Pt(111) systems might be

improved by taking into account relativistic corrections in our DFT calculations beyond those already included in the PAW potentials[135], which at this accuracy level might be important[173,174].

Both the B86SRP68-DF2 and PBEα57-DF2 DFs more or less predict the same reactivity for the H_2 + Ag(111) system. It is not possible however to call the DFs transferable to this system, yet. The lack of well described dissociative chemisorption experiments for this system does not yet allow us to make a broad statement about the accuracy of the theoretical description of this system. At present our description appears to be just shy of chemical accuracy.

5.4.9 Adiabatic description of S_0 and $E_{1/2}(\nu, J)$, a possible fingerprint for ehp excitations

The assumption of detailed balance entails that associative desorption is the inverse of dissociative chemisorption. In an adiabatic picture there is just one reason for a possible divergence of the obtained reaction probabilities. This is based on surface temperature, which is usually much higher in the associative desorption experiments than in the sticking experiments. This might lead to a breakdown of the detailed balance assumption that is usually involved when modeling associative desorption experiments with calculations on dissociative chemisorption. We note that it might be possible to model the associative desorption experiment directly[76,175–177], thereby negating the need to invoke the principle of detailed balance and investigate if associative desorption is indeed the inverse of dissociative chemisorption.

Including ehp excitations in dissociative chemisorption calculations would lower the reactivity thereby increasing the effective barrier[23]. Including ehp excitations in hypothetical associative desorption calculations, where molecules would start at the transition state and then desorb, would probably shift the translational energy distributions of desorbing molecules to lower energies and lead to lower effective barriers. When accounting for the effect of surface temperature, the difference in predicted reactivity as embodied by the $E_{1/2}(\nu, J)$ parameters obtained by including ehp excitations in associative desorption and dissociative chemisorption calculations, and their differences with results from adiabatic calculations, might then be taken to be a fingerprints for the effect of ehp excitation.

For the H_2 + Cu(111) system we know from DFMD calculations[63] and other approaches[24,30,157,158] that the effect of surface motion on the reactivity in dissociative chemisorption is small, even for high surface temperatures. Figure 5.23 shows some evidence that the broadening of reaction probability curves might affect the calculated $E_{1/2}(\nu, J)$ parameters for low J. However, in an

adiabatic picture, assuming detailed balance there should be no difference between calculations on dissociative adsorption and associative desorption.

We believe that this suggests a reason for only the SRP48 DF being chemically accurate for H_2 + Cu(111) for both dissociative chemisorption and associative desorption, since it overestimates the former and underestimates the latter predicted reactivity. The new SRP-DFs that are very accurate for dissociative chemisorption on cold surfaces, for which the BOSS model is valid[24,28–30,63,149], must underestimate the reactivity obtained from associative desorption by at least the extent to which surface temperature would increase the reactivity in dissociative chemisorption. Any remaining discrepancy can be safely attributed to the effect of ehp excitations.

The analysis of the H_2 + Au(111) system is more complicated due to the lack of dissociative chemisorption experiments and the current inability to take into account surface reconstruction (and thereby surface motion). Without at least either a dissociative chemisorption experiment or calculations using a reconstructed surface using the BOSS model, it is not yet possible to disentangle the contributions of the surface temperature, surface reconstruction and ehp excitations to the reactivity. Additionally, more detailed associative desorption and dissociative chemisorption experiments for the H_2 + Ag(111) system would allow for a systematic investigation into the effect of ehp excitations on reactivity for highly activated late barrier reactions.

5.5 Conclusions

We have constructed new SRP-DFs that include non-local correlation for the H_2 (D_2) + Cu(111) system and assessed the transferability of these DFs to the H_2 (D_2) + Ag(111), H_2 (D_2) + Au(111) and H_2 (D_2) + Pt(111) systems. All newly tested and developed DFs are based on GGA-exchange and use non-local correlation to describe dissociative chemisorption of H_2 (D_2) on Cu(111) within chemical accuracy, and, to the extent that it can be assessed, improve the transferability to the other systems discussed in this work over the previously reported SRP48 and MS-B86bl SRP-DFs.

The new SRP-DFs improve the description of the metal over the previously available SRP-DFs based on mixing GGA exchange while using semi-local correlation, especially concerning calculated lattice constants. In general, the new SRP-DFs with non-local correlation exhibit higher and later barriers to reaction in combination with a slightly lower energetic corrugation. We also find that vdW-DF2 non-local correlation performs better than vdW-DF1 correlation for all tested combinations with different exchange functionals, except when the exchange part of a functional was specifically optimized for use with vdW-DF1

correlation. The B86SRP68-DF2 functional best reproduces the measured Van der Waals well depths for H_2 + Cu(111), H_2 + Ag(111) and H_2 + Au(111).

SRP-DFs that include non-local correlation, namely B86SRP68-DF2 and PBEα57-DF2, are transferable from the highly activated late barrier H_2 + Cu(111) system to the weakly activated earlier barrier H_2 + Pt(111) system and vice versa. This feat could not be demonstrated with GGA and mGGA SRP-DFs that do not include non-local correlation. Assessing the transferability of the tested and developed SRP-DFs to H_2 + Ag(111) and H_2 + Au(111) is difficult due to the lack of well characterized molecular beam experiments. The SRP-DFs for H_2 + Cu(111) that include non-local correlation predict similar results for molecular beam sticking of D_2 + Ag(111), which are just shy of chemical accuracy. However it should be noted that there is some discussion about the validity of the beam parameters describing this particular molecular beam experiment.

A detailed analysis of associative desorption experiments on Cu(111) suggest that accurate calculation of $E_{1/2}(\nu, J)$ parameters requires an improvement of our dynamical model. Describing the surface degrees of freedom might close the gap between the excellent description of dissociative chemisorption and the good description of associative desorption, for molecules in the vibrational ground state. Any discrepancy in predicted reactivity between simulated associative desorption and dissociative chemisorption remaining after taking into account the effect of surface atom motion can then most likely be attributed to the neglect of ehp excitation. Lack of additional experiments for the H_2 + Au(111) system, specifically a well described dissociative chemisorption experiment, presently keeps us from disentangling the effects of surface reconstruction, surface temperature and ehp excitation for this system.

We have carried out a full molecular beam simulation for the H_2 + Cu(111) system using the QD method and the B86SRP68-DF2 DF for sticking in this system, which is the best performing DF for this system, and which includes non-local correlation. Overall H_2 + Cu(111) is very well described quasi-classically when looking at molecular beam sticking probabilities or degeneracy averaged initial state-selected reaction probabilities. At the level of molecular beam sticking, and degeneracy averaged reaction probabilities, the differences between the QD and QCT method are very small. The QD method predicts slightly higher reaction probabilities for molecular beam sticking for very narrow low average translational energy molecular beams when comparing to QCT results based on the same set of initial rovibrational states. When looking at initial-state resolved reaction probabilities the QD method predicts a somewhat larger orientational dependence of the reaction, in favor of molecules reacting in a parallel orientation. With respect to vibrationally and rotationally inelastic

scattering of H_2 from Cu(111) the B86SRP68-DF2 DF performs almost as well as the previous best SRP-DF for this system, namely the SRP48 DF.

5.A Appendix: CRP interpolation of PESs

In principle we use the following grids: $r \in \{0.4, 0.5, 0.6, 0.65, 0.7, 0.75, 0.8, 0.85, 1.0, 1.25, 1.5, 1.75, 2.0, 2.3\}$ Å and $Z \in \{0.25, 0.5, 0.75, 1.0, 1.25, 1.5, 1.75.2.0, 2.25, 2.5, 2.75, 3.0, 3.25, 3.5, 3.75, 4.0, 4.25, 4.5, 4.75, 5.0, 5.5, 6.0, 7.0\}$ Å for the 29 two dimensional cuts of the six dimensional molecular PES are used. For the atomic PES a grid denoted by $Z \in [-1.2 : 9]$ Å with $dZ = 0.075$ Å for $Z \leq 2$ Å and $dZ = 0.15$ Å for $Z > 2$ Å for all but the reference site was used. For the atomic reference site a dZ of 0.025 Å was used for $Z < 2$ Å. Note that in the case of the atomic PES hard to converge geometries can be discarded and additional points can be added at random Z to improve the quality of the resulting CRP PES.

5.B Appendix: Methods for determining parameters describing initial-state selected reaction probabilities from associative desorption experiments

5.B.1 Method A1

In method A1, it is assumed that the effective barrier heights ($E_0(\nu, J)$) can be kept the same in the description of the sticking and the associative desorption experiments, even though these are done at quite different temperatures[46,52]. The surface temperature dependence of $P_{\mathrm{deg}}(E, \nu, J)$ is taken into account by choosing the $W_{\nu,J}$ parameters larger in the description of the associative desorption experiments (done at high T_s, typically $>$ 900 K) than in the sticking experiments (done at low T_s, usually lower than room temperature), on the basis of experiments[53,56]. Next, the $A_{\nu,J}$ parameters are determined assuming that they do not depend on T_s, by requiring that the measured sticking probabilities can be computed according to Eqs. 5.4-5.9. In this procedure, the A parameters are typically taken either independent of the initial rovibrational state, or dependent only on ν to obtain a fitting procedure with a properly constrained number of degrees of freedom. In the latter case, one might use information regarding the relative values of the $A_{\nu,J}$ parameters extracted from the experiments. Procedure A1 was followed to extract initial-state resolved reaction probabilities in experiments on H_2 and D_2 desorbing from Cu(111)[46,48,52].

A comparison between theory and experiment can then be made in terms of $E_{1/2}(\nu, J)$ parameter values extracted from theory, which represent the incidence energy at which the computed reaction probability becomes equal to half the experimental saturation value $A_{\nu,J}$[11], and the experimental values of $E_0(\nu, J)$. Procedure A1 is illustrated in figure 5.B.1a for H_2 + Cu(111) and in figure 5.B.1c for D_2 + Cu(111). To be specific, here $E_{1/2}(\nu, J)$ would be taken as the incidence energy E for which the computed reaction probability $P_{\mathrm{deg}}(E, \nu, J)$ would first become equal to $\frac{0.325}{2}$ for H_2. A disadvantage of procedure A1 is that assuming that $E_{1/2}(\nu, J)$ parameters can be compared with $E_0(\nu, J)$ parameters presumes, in a way, that the saturation value of the computed sticking probability curve is the same as that of the measured one, which needs not be the case. This is one of the reasons that, in comparisons between theory and experiment, the procedure followed usually does not involve simply fitting computed reaction probabilities to Eq. 5.11 and then comparing the computed parameters of Eq. 5.11 directly to the experimental values. Using Eq. 5.11 to fit experimental reaction probabilities is at best a procedure to represent these probabilities over the range of energies from which they can be extracted with reasonable accuracy using Eq. 5.10. The error function fit form is not the most accurate expression to fit reaction probability curves for D_2 + Cu(111)[63], and comparison to theory suggests that using this expression does not yield an accurate extrapolation procedure to energies that exceed the energy range that can be used for the experimental extraction procedure (Eq. 5.10). We also note that the characteristic energies $E_{1/2}(\nu, J)$ will not usually be inflexion points of the theoretical reaction probability curves.

5.B.2 Method B1

In method B1, the experimental sticking probability curve is normalized by equating the reaction probability at $E_{\mathrm{max}}(\nu, J)$ to the computed value:[48,71]

$$A^{\mathrm{B1}}_{\nu,J} = P^{\mathrm{exp}}_{\mathrm{deg}}(E_{\mathrm{max}}(\nu, J)) \equiv P^{\mathrm{th}}_{\mathrm{deg}}(E_{\mathrm{max}}(\nu, J)) \tag{5.16}$$

In procedure B1, the thus extracted reaction probability is simply set equal to $A_{\nu,J}$. Theory is then compared with experiment by extracting the theoretical characteristic energy $E_{1/2}(\nu, J)$ using:

$$P^{\mathrm{th}}_{\mathrm{deg}}(E_{1/2}(\nu, J)) = \frac{1}{2} A^{\mathrm{B1}}_{\nu,J} \tag{5.17}$$

Method B1 is illustrated in figure 5.B.1b for H_2 + Cu(111), and in figure 5.B.1d for D_2 + Cu(111). Even though $E_{\mathrm{max}}(\nu, J)$ will usually not be big

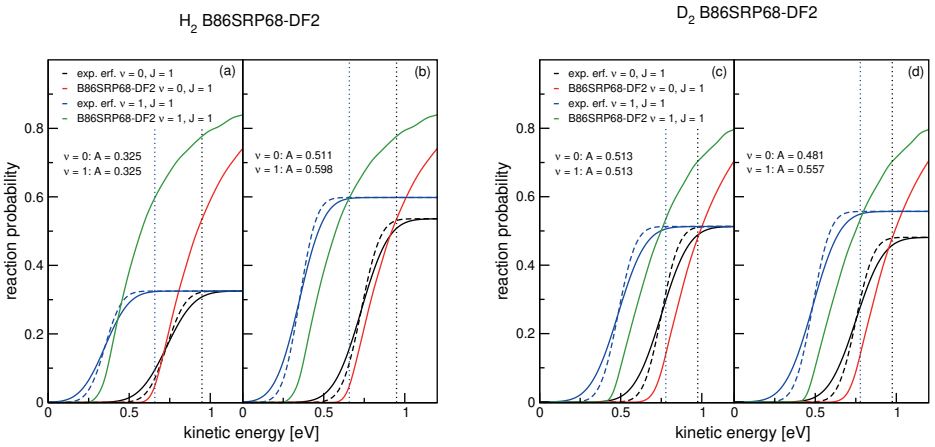

FIGURE 5.B.1: Reaction probability curves as a function of kinetic energy for H_2 + Cu(111) (a,b) and D_2 + Cu(111) (c,d). Experimental results[48] and QCT results obtained using the B86SRP68-DF2 SRP-DF are shown. Results for the $(\nu = 0, J = 1)$ rovibrational state are shown with experimental results in black and theoretical results in red, and for the $(\nu = 1, J = 1)$ rovibrational state are shown with experimental results in blue and theoretical results in green. Vertical dashed lines in the same color as the experimental results show $E_{\max}(\nu, J)$ for the corresponding state. Panels a and c illustrate method A1 to obtain $E_{1/2}(\nu, J)$ parameters and panels b and d method B1 (see text of appendix 5.B) . The solid experimental lines use the measured $W(\nu, J)$ parameters[48] while the dashed experimental lines use the scaled $W(\nu, J)$ parameters as detailed in the supporting information of Ref.[48]

enough for $P_{\text{deg}}(E_{\max}(\nu, J), \nu, J)$ to essentially equal the absolute A value at high translational energy, the approximate $E_{1/2}(\nu, J)$ extracted in this way will be rather accurate as long as $P_{\text{deg}}(E_{\max}(\nu, J), \nu, J) \geq 0.9$A, in which case $E_{1/2}(\nu, J)$ will be underestimated by no more than 0.09 $W_{\nu,J}$, with $W_{\nu,J}$ typically being 0.2 eV for H_2 + Cu(111)[48] and 0.3 eV for H_2 + Au(111)[71]. This condition is met if $E_{\max}(\nu, J) > E_0(\nu, J) + 0.9\ W_{\nu,J}$. Figure 5.B.2 shows that this is not the case for H_2 (D_2) + Au(111).

5.B.3 Method B2

As already mentioned for H_2 + Au(111), we found that $E_{\max}(\nu, J)$ was typically not large enough to extract $E_{1/2}(\nu, J)$ parameters accurately using method B1. For H_2 + Au(111) we therefore use what we call method B2, which, to our knowledge, has not been used before. In this case we determine $P_{\text{deg}}^{\text{exp}}(E_{\max}(\nu, J))$ from theory, but we then also use the measured $E_0(\nu, J)$ and $W_{\nu,J}$ value to

determine the $A_{\nu,J}$ value at which the experimental reaction probability curve extracted in this way should saturate according to the fit (Eq. 11). Then the characteristic theoretical $E_{1/2}(\nu, J)$ value is obtained by requiring that $P_{\mathrm{deg}}(E_{1/2}(\nu, J), \nu, J) = 0.5A^{\mathrm{B2}}_{\nu,J}$. This effectively means that we take the $A_{\nu,J}$ resulting from method B1 ($A^{\mathrm{B1}}_{\nu,J}$) and scale it accordingly:

$$A^{\mathrm{B2}}_{\nu,J} = \frac{A^{\mathrm{B1}}_{\nu,J}}{0.5 + 0.5erf\left(\frac{E_{\max}(\nu,J) - E_0(\nu,J)}{W_{\nu,J}}\right)} \tag{5.18}$$

Saturation values extracted using method B1 and B2 are compared to the experimental saturation values[71] for H_2 + Au(111) in figure 5.B.3a and for D_2 + Au(111) in figure 5.B.3b. Here, we should remember that the experimental saturation values are not on an absolute scale (they were determined using method A2). As shown in figure 5.B.3, the $A(\nu, J)$ parameters determined using method B1 and B2 do not vary much with ν and J, as expected from theory. In this, the $A(\nu, J)$ parameters obtained with methods B1 and B2 show a far less eratic dependence on J than the experimental values as obtained with method A2 (see figure 5.B.3). Also, as expected, they tend not to exceed unity.

5.C Appendix: The rotational hindering effect as obtained with the Dai-Zhang LEPS PES

We are aware of one single PES that does reproduce the rotational hindering effect as observed in the experiment, namely the LEPS PES[40] used by Dai et al.[38] for six-dimensional QD calculations. Dai et al.[38] reported a rotational hindering effect that is much stronger than we observe in all our data sets. We suspected that strong rotational hindering might be due to (i) the use of an unconverged basis set or a too large time step used in the original QD calculations[38], or to (ii) an inaccurate LEPS PES fit, or a combination of the two. We have recalculated the results reported by Dai et al.[38] which they present in their figure 1a[38] using the same LEPS potential[40] but with the QD input parameters of table 5.2 that are known to yield converged results. Our results are shown in figure 5.C.1b. Our converged TDWP calculations yield reaction probabilities that are somewhat lower than those reported by Dai et al.[38], but our results for the ground state do however agree very well with those published by Somers et al.[178] who used the same potential.

$E_{1/2}(\nu, J)$ parameters calculated using method A1 and B1 and using the QD method for the B86SRP68-DF2 functional and the LEPS PES used by Dai et al.[38] are shown in comparison to experimental results for ($\nu = 0$) in

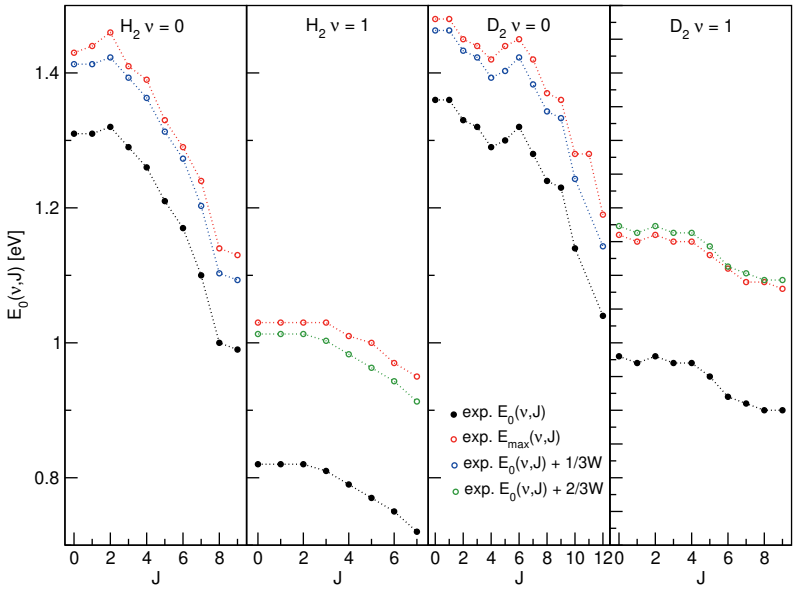

FIGURE 5.B.2: Measured[71] $E_0(\nu, J)$ parameters (black) and $E_{\max}(\nu, J)$ parameters (red) for H_2 (D_2) + Au(111) as a function of J. $E_0(\nu, J)$ parameters + $\frac{1}{3}$ W for ($\nu = 0$) (blue) and $E_0(\nu, J)$ parameters + $\frac{2}{3}$ W for ($\nu = 1$) (green) are shown as well.

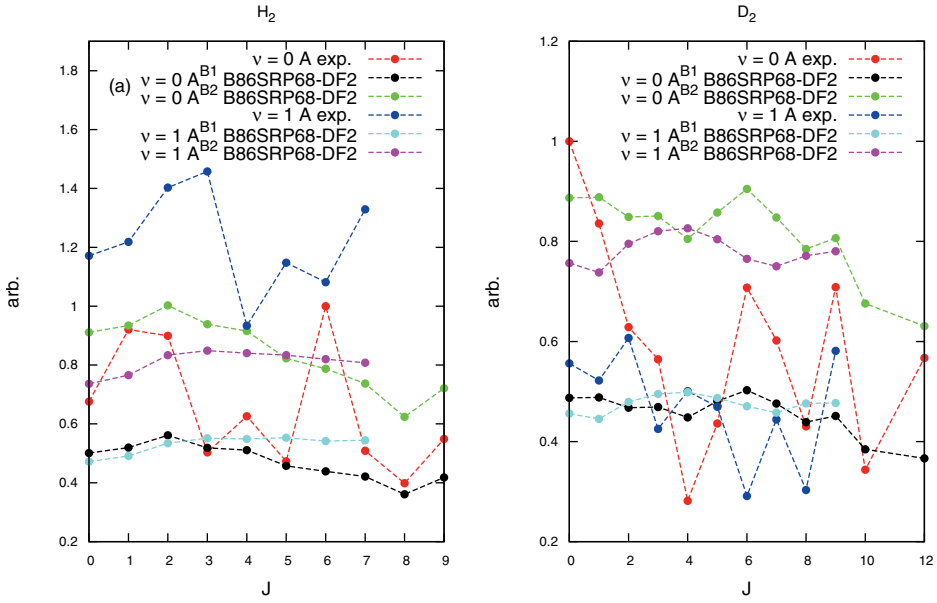

FIGURE 5.B.3: Comparison between the tabulated experimental[71] $A(\nu, J)$ values, red for $(\nu = 0)$ and blue for $(\nu = 1)$, the calculated $A^{\mathrm{B1}}(\nu, J)$ values computed using the B86SRP68-DF2 functional, black for $(\nu = 0)$ and cyan for $(\nu = 1)$, and the calculated $A^{\mathrm{B2}}(\nu, J)$ values computed using the B86SRP68-DF2 functional, green for $(\nu = 0)$ and magenta for $(\nu = 1)$, for H_2 (a) and D_2 (b) + Au(111) as a function of J. The experimentally measured values were obtained using method A2.

figure 5.C.1c. The calculated $E_{1/2}(\nu, J)$ parameters for the B86SRP68-DF2 functional and the LEPS PES are in remarkably good agreement for $J \geq 3$ for both method A1 and B1. It is clear that the B86SRP68-DF2 functional somewhat underestimates the subtle rotational hindering effect when using procedure B1. Our converged QD calculations reproduce the original finding[38] that using the LEPS PES yields the rotational hindering trend. However, the results obtained for the LEPS PES used by Dai et al.[38] somewhat overestimate the observed rotational hindering effect when using either procedure A1 or B1. This leaves the accuracy of the PES as a possible culprit of the discrepancies observed between the results of our PESs and the results for the LEPS PES. We are unable to check the fit accuracy of the LEPS PES compared to the underlying electronic structure calculations[41], which however are known to be unconverged[40,41]. We have however checked the fit accuracy of our CRP[121] PES for the B86SRP68-DF2 functional and found that our CRP[121] PES is highly accurate with respect to the underlying electronic structure calculations.

Since we do not observe the strong rotational hindering reported by Dai et al.[38] in any of the calculations we attempted for the reaction of H_2 with Cu(111) with our DFs, we believe that the large rotational hindering effect yielded by this particular LEPS PES must originate from inaccuracies still present in the LEPS fit or the underlying electronic structure calculations being unconverged. The good agreement between the results obtained using the LEPS PES[40] and our best SRP-DF for this system for $J \geq 3$ suggests that the observed rotational hindering is a very subtle effect.

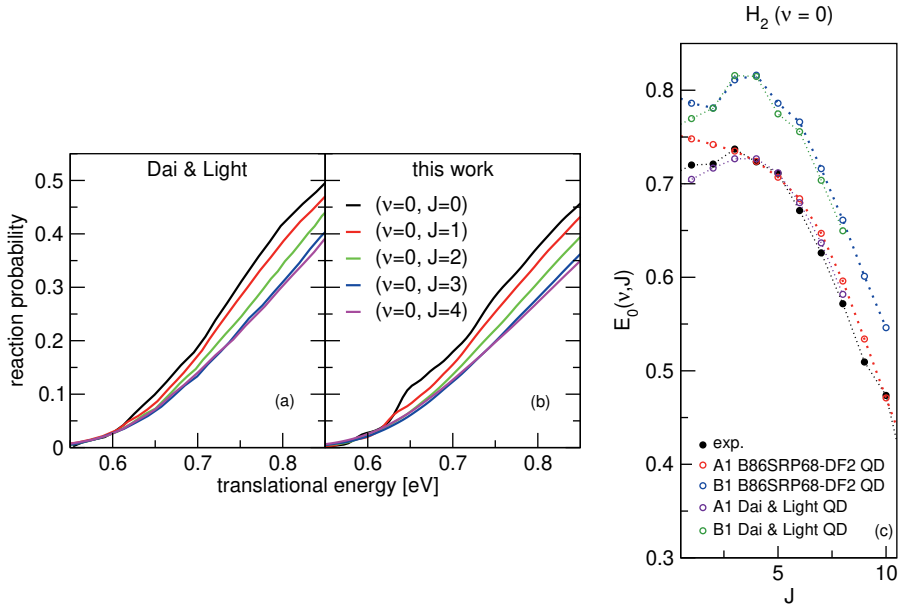

FIGURE 5.C.1: Panel a and b show degeneracy averaged reaction probabilities for $(\nu = 0, J \in [0, 4])$ for H_2 + Cu(111). The results in panel a are the original results of Dai et al.[38], panel b shows our results obtained using the same potential. $E_{1/2}(\nu, J)$ parameters calculated using the QD method are shown in panel c, with experimental results shown in black[48], and B86SRP68-DF2 results in red and blue. The $E_{1/2}(\nu, J)$ parameters for the LEPS PES used by Dai et al.[38] (purple, green) have been obtained from our QD calculations using the same LEPS PES[40].

References

(1) Smeets, E. W. F.; Kroes, G.-J. Designing new SRP density functionals including non-local vdW-DF2 correlation for H_2 + Cu(111) and their transferability to H_2 + Ag(111), Au(111) and Pt(111). *Phys. Chem. Chem. Phys.* **2021**, *23*, 7875–7901.

(2) Kroes, G.-J. Toward a database of chemically accurate barrier heights for reactions of molecules with metal surfaces. *J. Phys. Chem lett.* **2015**, *6*, 4106–4114.

(3) Wolcott, C. A.; Medford, A. J.; Studt, F.; Campbell, C. T. Degree of rate control approach to computational catalyst screening. *J. Catal.* **2015**, *330*, 197–207.

(4) Sabbe, M. K.; Reyniers, M.-F.; Reuter, K. First-principles kinetic modeling in heterogeneous catalysis: an industrial perspective on best-practice, gaps and needs. *Catal. Sci. Technol.* **2012**, *2*, 2010–2024.

(5) Ertl, G. Reactions at surfaces: from atoms to complexity (Nobel lecture). *Angew. Chem. Int. Ed.* **2008**, *47*, 3524–3535.

(6) Kroes, G.-J. Frontiers in surface scattering simulations. *Science* **2008**, *321*, 794–797.

(7) Waugh, K. Methanol synthesis. *Catal. Today* **1992**, *15*, 51–75.

(8) Grabow, L.; Mavrikakis, M. Mechanism of methanol synthesis on Cu through CO_2 and CO hydrogenation. *Acs Catalysis* **2011**, *1*, 365–384.

(9) Behrens, M.; Studt, F.; Kasatkin, I.; Kühl, S.; Hävecker, M.; Abild-Pedersen, F.; Zander, S.; Girgsdies, F.; Kurr, P.; Kniep, B.-L., et al. The active site of methanol synthesis over $Cu/ZnO/Al_2O_3$ industrial catalysts. *Science* **2012**, *336*, 893–897.

(10) Park, G. B.; Kitsopoulos, T. N.; Borodin, D.; Golibrzuch, K.; Neugebohren, J.; Auerbach, D. J.; Campbell, C. T.; Wodtke, A. M. The kinetics of elementary thermal reactions in heterogeneous catalysis. *Nature Rev. Chem.* **2019**, *3*, 723–732.

(11) Díaz, C.; Pijper, E.; Olsen, R.; Busnengo, H.; Auerbach, D.; Kroes, G. Chemically accurate simulation of a prototypical surface reaction: H_2 dissociation on Cu(111). *Science* **2009**, *326*, 832–834.

(12) Ghassemi, E. N.; Wijzenbroek, M.; Somers, M. F.; Kroes, G.-J. Chemically accurate simulation of dissociative chemisorption of D_2 on Pt(111). *Chem. Phys. Lett.* **2017**, *683*, 329–335.

(13) Smeets, E. W. F.; Voss, J.; Kroes, G.-J. Specific reaction parameter density functional based on the meta-generalized gradient approximation: application to H_2 + Cu(111) and H_2 + Ag(111). *J. Phys. Chem. A* **2019**, *123*, 5395–5406.

(14) Nattino, F.; Migliorini, D.; Kroes, G.-J.; Dombrowski, E.; High, E. A.; Killelea, D. R.; Utz, A. L. Chemically accurate simulation of a polyatomic molecule-metal surface reaction. *J. Phys. Chem. Lett.* **2016**, *7*, 2402–2406.

(15) Doblhoff-Dier, K.; Meyer, J.; Hoggan, P. E.; Kroes, G.-J. Quantum Monte Carlo calculations on a benchmark molecule-metal surface reaction: H_2 + Cu(111). *J. Chem. Theory Comput.* **2017**, *13*, 3208–3219.

(16) Boereboom, J.; Wijzenbroek, M.; Somers, M.; Kroes, G. Towards a specific reaction parameter density functional for reactive scattering of H_2 from Pd(111). *J. Chem. Phys.* **2013**, *139*, 244707.

(17) Migliorini, D.; Chadwick, H.; Nattino, F.; Gutiérrez-González, A.; Dombrowski, E.; High, E. A.; Guo, H.; Utz, A. L.; Jackson, B.; Beck, R. D., et al. Surface reaction barriometry: methane dissociation on flat and stepped transition-metal surfaces. *J. Phys. Chem. Lett.* **2017**, *8*, 4177–4182.

(18) Ghassemi, E. N.; Smeets, E. W. F.; Somers, M. F.; Kroes, G.-J.; Groot, I. M.; Juurlink, L. B.; Füchsel, G. Transferability of the specific reaction parameter density functional for H_2 + Pt(111) to H_2 + Pt(211). *J. Phys. Chem. C* **2019**, *123*, 2973–2986.

(19) Sementa, L.; Wijzenbroek, M.; Van Kolck, B.; Somers, M.; Al-Halabi, A.; Busnengo, H. F.; Olsen, R.; Kroes, G.-J.; Rutkowski, M.; Thewes, C., et al. Reactive scattering of H_2 from Cu(100): comparison of dynamics calculations based on the specific reaction parameter approach to density functional theory with experiment. *J. Chem. Phys.* **2013**, *138*, 044708.

(20) Nour Ghassemi, E.; Somers, M.; Kroes, G.-J. Test of the transferability of the specific reaction parameter functional for H_2+ Cu(111) to D_2 + Ag(111). *J. Phys. Chem. C* **2018**, *122*, 22939–22952.

(21) Tchakoua, T.; Smeets, E. W. F.; Somers, M.; Kroes, G.-J. Toward a specific reaction parameter density functional for H_2 + Ni(111): comparison of theory with molecular beam sticking experiments. *J. Phys. Chem. C* **2019**, *123*, 20420–20433.

(22) Šljivančanin, Ž.; Hammer, B. H_2 dissociation at defected Cu: preference for reaction at vacancy and kink sites. *Phys. Rev. B* **2002**, *65*, 085414.

(23) Spiering, P.; Meyer, J. Testing electronic friction models: vibrational de-excitation in scattering of H_2 and D_2 from Cu(111). *J. Phys. Chem. Lett.* **2018**, *9*, 1803–1808.

(24) Spiering, P.; Wijzenbroek, M.; Somers, M. An improved static corrugation model. *J. Chem. Phys.* **2018**, *149*, 234702.

(25) Kroes, G.-J.; Juaristi, J.; Alducin, M. Vibrational excitation of H_2 scattering from Cu(111): effects of surface temperature and of allowing energy exchange with the surface. *J. Phys. Chem. C* **2017**, *121*, 13617–13633.

(26) Somers, M.; McCormack, D.; Kroes, G.-J.; Olsen, R.; Baerends, E.; Mowrey, R. Signatures of site-specific reaction of H_2 on Cu(100). *J. Chem. Phys.* **2002**, *117*, 6673–6687.

(27) Nattino, F.; Díaz, C.; Jackson, B.; Kroes, G.-J. Effect of surface motion on the rotational quadrupole alignment parameter of D_2 reacting on Cu(111). *Phys. Rev. Lett.* **2012**, *108*, 236104.

(28) Kroes, G.-J.; Díaz, C. Quantum and classical dynamics of reactive scattering of H_2 from metal surfaces. *Chem. Soc. Rev.* **2016**, *45*, 3658–3700.

(29) Díaz, C.; Olsen, R. A.; Auerbach, D. J.; Kroes, G.-J. Six-dimensional dynamics study of reactive and non reactive scattering of H_2 from Cu(111) using a chemically accurate potential energy surface. *Phys. Chem. Chem. Phys.* **2010**, *12*, 6499–519.

(30) Wijzenbroek, M.; Somers, M. F. Static surface temperature effects on the dissociation of H_2 and D_2 on Cu(111). *J. Chem. Phys.* **2012**, *137*, 054703.

(31) McCormack, D. A.; Kroes, G.-.-J.; Olsen, R. A.; Groeneveld, J. A.; van Stralen, J. N.; Baerends, E. J.; Mowrey, R. C. Quantum dynamics of the dissociation of H_2 on Cu(100): dependence of the site-reactivity on initial rovibrational state. *Faraday Discuss.* **2000**, *117*, 109–132.

(32) McCormack, D. A.; Kroes, G.-J.; Olsen, R. A.; Groeneveld, J. A.; van Stralen, J. N.; Baerends, E. J.; Mowrey, R. C. Molecular knife throwing: aiming for dissociation at specific surface sites through state-selection. *Chem. Phys. Lett.* **2000**, *328*, 317–324.

(33) Chen, J.; Zhou, X.; Jiang, B. Eley Rideal recombination of hydrogen atoms on Cu(111): quantitative role of electronic excitation in cross sections and product distributions. *J. Chem. Phys.* **2019**, *150*, 061101.

(34) Darling, G.; Holloway, S. Rotational motion and the dissociation of H_2 on Cu(111). *J. Chem. Phys.* **1994**, *101*, 3268–3281.

(35) Sakong, S.; Groß, A. Dissociative adsorption of hydrogen on strained Cu surfaces. *Surf. Sci.* **2003**, *525*, 107–118.

(36) Kroes, G.-J.; Pijper, E.; Salin, A. Dissociative chemisorption of H_2 on the Cu(110) surface: A quantum and quasiclassical dynamical study. *J. Chem. Phys.* **2007**, *127*, 164722.

(37) Smeets, E. W. F.; Füchsel, G.; Kroes, G.-J. Quantum dynamics of dissociative chemisorption of H_2 on the Stepped Cu(211) Surface. *J. Phys. Chem. C* **2019**, *123*, 23049–23063.

(38) Dai, J.; Light, J. C. The steric effect in a full dimensional quantum dynamics simulation for the dissociative adsorption of H_2 on Cu(111). *J. Chem. Phys.* **1998**, *108*, 7816–7820.

(39) Dai, J.; Light, J. C. Six dimensional quantum dynamics study for dissociative adsorption of H_2 on Cu(111) surface. *J. Chem. Phys.* **1997**, *107*, 1676–1679.

(40) Dai, J.; Zhang, J. Z. Quantum adsorption dynamics of a diatomic molecule on surface: four-dimensional fixed-site model for H_2 on Cu(111). *J. Chem. Phys.* **1995**, *102*, 6280–6289.

(41) Hammer, B.; Scheffler, M.; Jacobsen, K. W.; Nørskov, J. K. Multidimensional potential energy surface for H_2 dissociation over Cu(111). *Phys. Rev. Lett.* **1994**, *73*, 1400–1403.

(42) Wijzenbroek, M.; Klein, D. M.; Smits, B.; Somers, M. F.; Kroes, G.-J. Performance of a non-local van der Waals density functional on the dissociation of H_2 on metal surfaces. *J. Phys. Chem. A* **2015**, *119*, 12146–12158.

(43) Füchsel, G.; Cao, K.; Er, S.; Smeets, E. W. F.; Kleyn, A. W.; Juurlink, L. B. F.; Kroes, G.-J. Anomalous dependence of the reactivity on the presence of steps: dissociation of D_2 on Cu(211). *J. Phys. Chem. Lett.* **2018**, *9*, 170–175.

(44) Kroes, G.-J.; Pavanello, M.; Blanco-Rey, M.; Alducin, M.; Auerbach, D. J. Ab initio molecular dynamics calculations on scattering of hyperthermal H atoms from Cu(111) and Au(111). *J. Chem. Phys.* **2014**, *141*, 054705.

(45) Michelsen, H. A.; Auerbach, D. J. A critical examination of data on the dissociative adsorption and associative desorption of hydrogen at copper surfaces. *J. Chem. Phys.* **1991**, *94*, 7502–7520.

(46) Michelsen, H.; Rettner, C.; Auerbach, D.; Zare, R. Effect of rotation on the translational and vibrational energy dependence of the dissociative adsorption of D_2 on Cu(111). *J. Chem. Phys.* **1993**, *98*, 8294–8307.

(47) Berger, H.; Leisch, M.; Winkler, A.; Rendulic, K. A search for vibrational contributions to the activated adsorption of H_2 on copper. *Chem. Phys. Lett.* **1990**, *175*, 425–428.

(48) Kaufmann, S.; Shuai, Q.; Auerbach, D. J.; Schwarzer, D.; Wodtke, A. M. Associative desorption of hydrogen isotopologues from copper surfaces: characterization of two reaction mechanisms. *J. Chem. Phys.* **2018**, *148*, 194703.

(49) Anger, G.; Winkler, A.; Rendulic, K. Adsorption and desorption kinetics in the systems H_2/Cu(111), H_2/Cu(110) and H_2/Cu(100). *Surf. Sci.* **1989**, *220*, 1–17.

(50) Hou, H.; Gulding, S.; Rettner, C.; Wodtke, A.; Auerbach, D. The stereodynamics of a gas-surface reaction. *Science* **1997**, *277*, 80–82.

(51) Comsa, G.; David, R. The purely "fast" distribution of H_2 and D_2 molecules desorbing from Cu(100) and Cu(111) surfaces. *Surf. Sci.* **1982**, *117*, 77–84.

(52) Rettner, C.; Michelsen, H.; Auerbach, D. Quantum-state-specific dynamics of the dissociative adsorption and associative desorption of H_2 at a Cu(111) surface. *J. Chem. Phys.* **1995**, *102*, 4625–4641.

(53) Rettner, C.; Auerbach, D.; Michelsen, H. Dynamical studies of the interaction of D_2 with a Cu(111) surface. *J. Vac. Sci. Technol. A* **1992**, *10*, 2282–2286.

(54) Rettner, C.; Michelsen, H.; Auerbach, D. Determination of quantum-state-specific gas—surface energy transfer and adsorption probabilities as a function of kinetic energy. *Chem. Phys.* **1993**, *175*, 157–169.

(55) Hodgson, A.; Samson, P.; Wight, A.; Cottrell, C. Rotational excitation and vibrational relaxation of H_2 (ν= 1, J= 0) Scattered from Cu(111). *Phys. Rev. Lett.* **1997**, *78*, 963–966.

(56) Michelsen, H.; Rettner, C.; Auerbach, D. On the influence of surface temperature on adsorption and desorption in the D_2/Cu(111) system. *Surf. Sci.* **1992**, *272*, 65–72.

(57) Okazawa, T.; Takeuchi, F.; Kido, Y. Enhanced and correlated thermal vibrations of Cu(111) and Ni(111) surfaces. *Physical Review B* **2005**, *72*, 075408.

(58) Lindgren, S.; Walldén, L.; Rundgren, J.; Westrin, P. Low-energy electron diffraction from Cu(111): subthreshold effect and energy-dependent inner potential; surface relaxation and metric distances between spectra. *Phys. Rev. B* **1984**, *29*, 576–588.

(59) Chae, K.; Lu, H.; Gustafsson, T. Medium-energy ion-scattering study of the temperature dependence of the structure of Cu(111). *Phys. Rev. B* **1996**, *54*, 14082.

(60) Andersson, S.; Persson, M. Sticking in the physisorption well: influence of surface structure. *Phys. Rev. Lett.* **1993**, *70*, 202.

(61) Cao, K.; Füchsel, G.; Kleyn, A. W.; Juurlink, L. B. Hydrogen adsorption and desorption from Cu(111) and Cu(211). *Phys. Chem. Chem. Phys.* **2018**, *20*, 22477–22488.

(62) Harten, U.; Toennies, J. P.; Wöll, C. Molecular beam translational spectroscopy of physisorption bound states of molecules on metal surfaces. I. HD on Cu(111) and Au(111) single crystal surfaces. *J. Chem. Phys.* **1986**, *85*, 2249–2258.

(63) Nattino, F.; Genova, A.; Guijt, M.; Muzas, A. S.; Díaz, C.; Auerbach, D. J.; Kroes, G.-J. Dissociation and recombination of D_2 on Cu(111): Ab initio molecular dynamics calculations and improved analysis of desorption experiments. *J. Chem. Phys.* **2014**, *141*, 124705.

(64) Cao, K.; van Lent, R.; Kleyn, A.; Juurlink, L. A molecular beam study of D_2 dissociation on Pt(111): testing SRP-DFT calculations. *Chem. Phys. Lett.* **2018**, *706*, 680–683.

(65) Luntz, A.; Brown, J.; Williams, M. Molecular beam studies of H_2 and D_2 dissociative chemisorption on Pt(111). *J. Chem. Phys.* **1990**, *93*, 5240–5246.

(66) Ghassemi, E. N.; Somers, M. F.; Kroes, G.-J. Assessment of two problems of specific reaction parameter density functional theory: sticking and diffraction of H_2 on Pt(111). *J. Phys. Chem. C* **2019**, *123*, 10406–10418.

(67) Pijper, E.; Kroes, G.-J.; Olsen, R. A.; Baerends, E. J. Reactive and diffractive scattering of H_2 from Pt(111) studied using a six-dimensional wave packet method. *J. Chem. Phys.* **2002**, *117*, 5885–5898.

(68) Kroes, G.-J.; Somers, M. F. Six-dimensional dynamics of dissociative chemisorption of H_2 on metal surface. *J. Theor. Comput. Chem.* **2005**, *4*, 493–581.

(69) Raff, L. M.; Karplus, M. Theoretical investigations of reactive collisions in molecular beams: K+CH_3I and related systems. *J. Chem. Phys.* **1966**, *44*, 1212–1229.

(70) Cardillo, M.; Balooch, M.; Stickney, R. Detailed balancing and quasi-equilibrium in the adsorption of hydrogen on copper. *Surf. Sci.* **1975**, *50*, 263–278.

(71) Shuai, Q.; Kaufmann, S.; Auerbach, D. J.; Schwarzer, D.; Wodtke, A. M. Evidence for electron–hole pair excitation in the associative desorption of H_2 and D_2 from Au(111). *J. Phys. Chem. Lett.* **2017**, *8*, 1657–1663.

(72) Perrier, A.; Bonnet, L.; Liotard, D.; Rayez, J.-C. On the dynamics of H_2 desorbing from a Pt(111) surface. *Surf. Sci.* **2005**, *581*, 189–198.

(73) Perrier, A.; Bonnet, L.; Rayez, J.-C. Dynamical study of H_2 and D_2 desorbing from a Cu(111) surface. *J. Phys. Chem. A* **2006**, *110*, 1608–1617.

(74) Perrier, A.; Bonnet, L.; Rayez, J.-C. Statisticodynamical approach of final state distributions in associative desorptions. *J. Chem. Phys.* **2006**, *124*, 194701.

(75) Díaz, C.; Perrier, A.; Kroes, G. Associative desorption of N_2 from Ru(0001): a computational study. *Chem. Phys. Lett.* **2007**, *434*, 231–236.

(76) Galparsoro, O.; Kaufmann, S.; Auerbach, D. J.; Kandratsenka, A.; Wodtke, A. M. First principles rates for surface chemistry employing exact transition state theory: application to recombinative desorption of hydrogen from Cu(111). *Phys. Chem. Chem. Phys.* **2020**, *22*, 17532–17539.

(77) Perdew, J. P.; Chevary, J. A.; Vosko, S. H.; Jackson, K. A.; Pederson, M. R.; Singh, D. J.; Fiolhais, C. Atoms, molecules, solids, and surfaces: Applications of the generalized gradient approximation for exchange and correlation. *Phys. Rev. B* **1992**, *46*, 6671–6687.

(78) Murphy, M.; Hodgson, A. Translational energy release in the recombinative desorption of H_2 from Ag(111). *Surf. Sci.* **1997**, *390*, 29–34.

(79) Murphy, M.; Hodgson, A. Role of surface thermal motion in the dissociative chemisorption and recombinative desorption of D_2 on Ag(111). *Phys. Rev. Lett.* **1997**, *78*, 4458–4461.

(80) Jiang, B.; Guo, H. Six-dimensional quantum dynamics for dissociative chemisorption of H 2 and D 2 on Ag (111) on a permutation invariant potential energy surface. *Physical Chemistry Chemical Physics* **2014**, *16*, 24704–24715.

(81) Jiang, B.; Guo, H. Permutation invariant polynomial neural network approach to fitting potential energy surfaces. III. Molecule-surface interactions. *J. Chem. Phys.* **2014**, *141*, 034109.

(82) Lee, G.; Plummer, E. Interaction of hydrogen with the Ag(111) surface. *Phys. Rev. B* **1995**, *51*, 7250.

(83) Sprunger, P.; Plummer, E. Interaction of hydrogen with the Ag(110) surface. *Phys. Rev. B* **1993**, *48*, 14436.

(84) Avouris, P.; Schmeisser, D.; Demuth, J. Observation of rotational excitations of H_2 adsorbed on Ag surfaces. *Phys. Rev. Lett.* **1982**, *48*, 199.

(85) Healey, F.; Carter, R.; Worthy, G.; Hodgson, A. Endothermic dissociative chemisorption of molecular D2 on Ag (111). *Chemical physics letters* **1995**, *243*, 133–139.

(86) Parker, D. H.; Jones, M. E.; Koel, B. E. Determination of the reaction order and activation energy for desorption kinetics using TPD spectra: Application to D_2 desorption from Ag(111). *Surf. Sci.* **1990**, *233*, 65–73.

(87) Lee, G.; Sprunger, P.; Okada, M.; Poker, D.; Zehner, D.; Plummer, E. Chemisorption of hydrogen on the Ag(111) surface. *J. Vac. Sci. Technol. A* **1994**, *12*, 2119–2123.

(88) Asada, H. Specular reflection of helium and hydrogen molecular beams from the (111) plane of silver. *Surface Science* **1979**, *81*, 386–408.

(89) Horne, J. M.; Yerkes, S. C.; Miller, D. R. An experimental investigation of the elastic scattering of He and H2 from Ag (111). *Surface Science* **1980**, *93*, 47–63.

(90) Yu, C.-f.; Whaley, K. B.; Hogg, C. S.; Sibener, S. J. Selective Adsorption Resonances in the Scattering of n-H_2 p-H_2 n-D_2 and o-D_2 from Ag(111). *Phys. Rev. Lett.* **1983**, *51*, 2210.

(91) Yu, C.-f.; Whaley, K. B.; Hogg, C. S.; Sibener, S. J. Investigation of the spatially isotropic component of the laterally averaged molecular hydrogen/Ag(111) physisorption potential. *J. Chem. Phys.* **1985**, *83*, 4217–4234.

(92) Mattera, L.; Musenich, R.; Salvo, C.; Terreni, S. Hydrogen diffraction from the (110) surface of silver. *Faraday Discuss.* **1985**, *80*, 115–126.

(93) Maurer, R. J.; Zhang, Y.; Guo, H.; Jiang, B. Hot electron effects during reactive scattering of H_2 from Ag(111): assessing the sensitivity to initial conditions, coupling magnitude, and electronic temperature. *Faraday Discuss.* **2019**, *214*, 105–121.

(94) Zhang, Y.; Maurer, R. J.; Guo, H.; Jiang, B. Hot-electron effects during reactive scattering of H_2 from Ag(111): the interplay between mode-specific electronic friction and the potential energy landscape. *Chem. Sci.* **2019**, *10*, 1089–1097.

(95) Maurer, R. J.; Jiang, B.; Guo, H.; Tully, J. C. Mode specific electronic friction in dissociative chemisorption on metal surfaces: H 2 on Ag (111). *Physical review letters* **2017**, *118*, 256001.

(96) Muzas, A. S.; Juaristi, J. I.; Alducin, M.; Díez Muiño, R.; Kroes, G.-J.; Díaz, C. Vibrational deexcitation and rotational excitation of H_2 and D_2 scattered from Cu(111): adiabatic versus non-adiabatic dynamics. *J. Chem. Phys.* **2012**, *137*, 064707.

(97) Dion, M.; Rydberg, H.; Schröder, E.; Langreth, D. C.; Lundqvist, B. I. Van der Waals density functional for general geometries. *Phys. Rev. Lett.* **2004**, *92*, 246401.

(98) Lee, K.; Murray, É. D.; Kong, L.; Lundqvist, B. I.; Langreth, D. C. Higher-accuracy van der Waals density functional. *Phys. Rev. B* **2010**, *82*, 081101.

(99) Cowin, J. P.; Yu, C.-F.; Sibener, S. J.; Hurst, J. E. Bound level resonances in rotationally inelastic HD/Pt (111) surface scattering. *The Journal of Chemical Physics* **1981**, *75*, 1033–1034.

(100) Cowin, J. P.; Yu, C.-F.; Sibener, S. J.; Wharton, L. HD scattering from Pt(111): rotational excitation probabilities. *J. Chem. Phys.* **1983**, *79*, 3537–3549.

(101) Cowin, J. P.; Yu, C.-F.; Wharton, L. HD scattering from Pt(111): Rotationally mediated selective adsorption. *Surf. Sci.* **1985**, *161*, 221–233.

(102) Yu, C.-F.; Hogg, C. S.; Cowin, J. P.; Whaley, K. B.; Light, J. C.; Sibener, S. J. Rotationally mediated selective adsorption as a probe of isotropic and anisotropic molecule—surface interaction potentials: HD (J)/Ag(111). *Israel J. Chem.* **1982**, *22*, 305–314.

(103) Perreau, J.; Lapujoulade, J. Selective adsorption of He, H_2 on copper surfaces. *Surf. Sci.* **1982**, *122*, 341–354.

(104) Kaufhold, A.; Toennies, J. P. An optical potential for rotationally mediated selective adsorption (Feshbach) resonances in scattering of molecules from smooth crystal surfaces. *Surf. Sci.* **1986**, *173*, 320–336.

(105) Andersson, S.; Wilzén, L.; Persson, M. Physisorption interaction of H_2 with noble-metal surfaces: A new H_2-Cu potential. *Phys. Rev. B* **1988**, *38*, 2967.

(106) Lennard-Jones, J. E.; Devonshire, A. F. Diffraction and selective adsorption of atoms at crystal surfaces. *Nature* **1936**, *137*, 1069–1070.

(107) Hoinkes, H.; Wilsch, H. In *Helium Atom Scattering from Surfaces*; Springer: 1992, pp 113–172.

(108) Bertino, M. F.; Hofmann, F.; Toennies, J. P. The effect of dissociative chemisorption on the diffraction of D_2 from Ni(110). *J. Chem. Phys.* **1997**, *106*, 4327–4338.

(109) Nieto, P.; Pijper, E.; Barredo, D.; Laurent, G.; Olsen, R. A.; Baerends, E.-J.; Kroes, G.-J.; Farías, D. Reactive and nonreactive scattering of H_2 from a metal surface is electronically adiabatic. *Science* **2006**, *312*, 86–89.

(110) Bertino, M.; Miret-Artés, S.; Toennies, J.; Benedek, G. Observation of rotationally mediated focused inelastic resonances in D_2 scattering from Cu(001). *Phys. Rev. B* **1997**, *56*, 9964.

(111) Poelsema, B.; Lenz, K.; Comsa, G. The dissociative adsorption of hydrogen on defect-free Pt(111). *J. Phys. Condens. Matter* **2010**, *22*, 304006.

(112) Hamada, I. van der Waals density functional made accurate. *Phys. Rev. B* **2014**, *89*, 121103.

(113) Hammer, B. H. L. B.; Hansen, L. B.; Nørskov, J. K. Improved adsorption energetics within density-functional theory using revised Perdew-Burke-Ernzerhof functionals. *Phys. Rev. B* **1999**, *59*, 7413–7421.

(114) Perdew, J. P.; Ruzsinszky, A.; Csonka, G. I.; Constantin, L. A.; Sun, J. Workhorse semilocal density functional for condensed matter physics and quantum chemistry. *Phys. Rev. Lett.* **2009**, *103*, 026403.

(115) Klimeš, J.; Bowler, D. R.; Michaelides, A. Chemical accuracy for the van der Waals density functional. *J. Phys. Condens. Matter* **2009**, *22*, 022201.

(116) Perdew, J. P.; Burke, K.; Ernzerhof, M. Generalized gradient approximation made simple. *Phys. Rev. Lett.* **1996**, *77*, 3865–3868.

(117) Madsen, G. K. Functional form of the generalized gradient approximation for exchange: the PBEα functional. *Phys. Rev. B* **2007**, *75*, 195108.

(118) Perdew, J. P.; Ruzsinszky, A.; Csonka, G. I.; Vydrov, O. A.; Scuseria, G. E.; Constantin, L. A.; Zhou, X.; Burke, K. Restoring the density-gradient expansion for exchange in solids and surfaces. *Phys. Rev. Lett.* **2008**, *100*, 136406.

(119) Zhang, Y.; Yang, W. Comment on "Generalized gradient approximation made simple". *Phys. Rev. Lett.* **1998**, *80*, 890.

(120) Perdew, J. P.; Yue, W. Accurate and simple density functional for the electronic exchange energy: generalized gradient approximation. *Phys. Rev. B* **1986**, *33*, 8800.

(121) Busnengo, H.; Salin, A.; Dong, W. Representation of the 6D potential energy surface for a diatomic molecule near a solid surface. *J. Chem. Phys.* **2000**, *112*, 7641–7651.

(122) Füchsel, G.; del Cueto, M.; Díaz, C.; Kroes, G.-J. Enigmatic HCl + Au(111) reaction: a puzzle for theory and experiment. *J. Phys. Chem. C* **2016**, *120*, 25760–25779.

(123) Stoer, J.; Bulirsch, R., *Introduction to numerical analysis*; Springer Science & Business Media, New York: 2013; Vol. 12.

(124) Kosloff, R. Time-dependent quantum-mechanical methods for molecular dynamics. *J. Phys. Chem. C* **1988**, *92*, 2087–2100.

(125) Kosloff, R. In *Time-Dependent Quantum Molecular Dynamics*; Springer: 1992, pp 97–116.

(126) Balint-Kurti, G. G.; Dixon, R. N.; Marston, C. C. Grid methods for solving the Schrödinger equation and time dependent quantum dynamics of molecular photofragmentation and reactive scattering processes. *Int. Rev. Phys. Chem.* **1992**, *11*, 317–344.

(127) Wijzenbroek, M.; Kroes, G. The effect of the exchange-correlation functional on H2 dissociation on Ru(0001). *J. Chem. Phys.* **2014**, *140*, 084702.

(128) Groot, I.; Ueta, H.; Van der Niet, M.; Kleyn, A.; Juurlink, L. Supersonic molecular beam studies of dissociative adsorption of H_2 on Ru(0001). *J. Chem. Phys.* **2007**, *127*, 244701.

(129) Zare, R. N.; Harter, W. G. Angular momentum: understanding spatial aspects in chemistry and physics. *Phys. Today* **1989**, *42*, 68–72.

(130) Kresse, G.; Hafner, J. Ab initio molecular-dynamics simulation of the liquid-metal–amorphous-semiconductor transition in germanium. *Phys. Rev. B* **1994**, *49*, 14251–14269.

(131) Kresse, G.; Hafner, J. Ab initio molecular dynamics for liquid metals. *Phys. Rev. B* **1993**, *47*, 558–561.

(132) Kresse, G.; Furthmüller, J. Efficient iterative schemes for ab initio total-energy calculations using a plane-wave basis set. *Phys. Rev. B* **1996**, *54*, 11169–11186.

(133) Kresse, G.; Furthmüller, J. Efficiency of ab-initio total energy calculations for metals and semiconductors using a plane-wave basis set. *Comput. Mater. Sci.* **1996**, *6*, 15–50.

(134) Lehtola, S.; Steigemann, C.; Oliveira, M. J.; Marques, M. A. Recent developments in libxc — A comprehensive library of functionals for density functional theory. *SoftwareX* **2018**, *7*, 1–5.

(135) Blöchl, P. E. Projector augmented-wave method. *Phys. Rev. B* **1994**, *50*, 17953–17979.

(136) Klimeš, J. ř.; Bowler, D. R.; Michaelides, A. Van der Waals density functionals applied to solids. *Phys. Rev. B* **2011**, *83*, 195131.

(137) Román-Pérez, G.; Soler, J. M. Efficient implementation of a Van der Waals density functional: application to double-wall carbon nanotubes. *Phys. Rev. Lett.* **2009**, *103*, 096102.

(138) Vanderbilt, D. Soft self-consistent pseudopotentials in a generalized eigenvalue formalism. *Phys. Rev. B* **1990**, *41*, 7892–7895.

(139) Haas, P.; Tran, F.; Blaha, P. Calculation of the lattice constant of solids with semilocal functionals. *Phys. Rev. B* **2009**, *79*, 085104.

(140) Statiris, P.; Lu, H.; Gustafsson, T. Temperature dependent sign reversal of the surface contraction of Ag(111). *Phys. Rev. Lett.* **1994**, *72*, 3574–3577.

(141) Soares, E.; Leatherman, G.; Diehl, R.; Van Hove, M. Low-energy electron diffraction study of the thermal expansion of Ag(111). *Surf. Sci.* **2000**, *468*, 129–136.

(142) Nichols, R.; Nouar, T.; Lucas, C.; Haiss, W.; Hofer, W. Surface relaxation and surface stress of Au(111). *Surf. Sci.* **2002**, *513*, 263–271.

(143) Ohtani, H.; Van Hove, M.; Somorjai, G. LEED intensity analysis of the surface structures of Pd(111) and of co adsorbed on Pd (111) in a $(\sqrt{3} \times \sqrt{3})$ R30 arrangement. *Surf. Sci.* **1987**, *187*, 372–386.

(144) Adams, D. L.; Nielsen, H.; Van Hove, M. A. Quantitative analysis of low-energy-electron diffraction: application to Pt(111). *Phys. Rev. B* **1979**, *20*, 4789.

(145) Wijzenbroek, M.; Helstone, D.; Meyer, J.; Kroes, G.-J. Dynamics of H_2 dissociation on the close-packed (111) surface of the noblest metal: H_2 + Au(111). *J. Chem. Phys.* **2016**, *145*, 144701.

(146) Patra, A.; Bates, J. E.; Sun, J.; Perdew, J. P. Properties of real metallic surfaces: effects of density functional semilocality and Van der Waals nonlocality. *Proc. Natl. Acad. Sci.* **2017**, *114*, E9188–E9196.

(147) Cottrell, C.; Carter, R.; Nesbitt, A.; Samson, P.; Hodgson, A. Vibrational state dependence of D_2 dissociation on Ag(111). *J. Chem. Phys.* **1997**, *106*, 4714–4722.

(148) Kaufmann, S. personal communication.

(149) Wei, C. Y.; Lewis, S. P.; Mele, E. J.; Rappe, A. M. Structure and vibrations of the vicinal copper (211) surface. *Phys. Rev. B* **1998**, *57*, 10062–10068.

(150) Shakouri, K.; Behler, J.; Meyer, J.; Kroes, G.-J. Accurate neural network description of surface phonons in reactive gas-surface dynamics: N_2+ Ru(0001). *J. Phys. Chem. Lett.* **2017**, *8*, 2131–2136.

(151) Gerrits, N.; Chadwick, H.; Kroes, G.-J. Dynamical study of the dissociative chemisorption of CHD_3 on Pd(111). *J. Phys. Chem. C* **2019**, *123*, 24013–24023.

(152) Gerrits, N.; Shakouri, K.; Behler, J.; Kroes, G.-J. Accurate probabilities for highly activated reaction of polyatomic molecules on surfaces using a high-dimensional neural network potential: CHD_3 + Cu(111). *J. Phys. Chem. Lett.* **2019**, *10*, 1763–1768.

(153) Schimka, L.; Harl, J.; Stroppa, A.; Grüneis, A.; Marsman, M.; Mittendorfer, F.; Kresse, G. Accurate surface and adsorption energies from many-body perturbation theory. *Nature materials* **2010**, *9*, 741–744.

(154) Lee, K.; Berland, K.; Yoon, M.; Andersson, S.; Schröder, E.; Hyldgaard, P.; Lundqvist, B. I. Benchmarking van der Waals density functionals with experimental data: potential-energy curves for H_2 molecules on Cu(111),(100) and (110) surfaces. *J. Phys. Condens. Matter* **2012**, *24*, 424213.

(155) Darling, G.; Holloway, S. Resonance-mediated dissociative adsorption of hydrogen. *J. Chem. Phys.* **1990**, *93*, 9145–9156.

(156) Juaristi, J.; Alducin, M.; Muiño, R. D.; Busnengo, H. F.; Salin, A. Role of electron-hole pair excitations in the dissociative adsorption of diatomic molecules on metal surfaces. *Phys. Rev. Lett.* **2008**, *100*, 116102.

(157) Mondal, A.; Wijzenbroek, M.; Bonfanti, M.; Díaz, C.; Kroes, G.-J. Thermal lattice expansion effect on reactive scattering of H_2 from Cu(111) at T_s = 925 K. *J. Phys. Chem. A* **2013**, *117*, 8770–8781.

(158) Bonfanti, M.; Somers, M. F.; Díaz, C.; Busnengo, H. F.; Kroes, G.-J. 7D quantum dynamics of H_2 scattering from Cu(111): the accuracy of the phonon sudden approximation. *Z. Phys. Chem.* **2013**, *227*, 1397–1420.

(159) Mukherjee, S.; Libisch, F.; Large, N.; Neumann, O.; Brown, L. V.; Cheng, J.; Lassiter, J. B.; Carter, E. A.; Nordlander, P.; Halas, N. J. Hot electrons do the impossible: plasmon-induced dissociation of H_2 on Au. *Nano lett.* **2012**, *13*, 240–247.

(160) Hasselbrink, E. Non-adiabaticity in surface chemical reactions. *Surf. Sci.* **2009**, *603*, 1564–1570.

(161) Schindler, B.; Diesing, D.; Hasselbrink, E. Electronic excitations induced by hydrogen surface chemical reactions on gold. *J. Chem. Phys.* **2011**, *134*, 034705.

(162) Schindler, B.; Diesing, D.; Hasselbrink, E. Electronically nonadiabatic processes in the interaction of H with a Au surface revealed using MIM junctions: the temperature dependence. *J. Phys. Chem. C* **2013**, *117*, 6337–6345.

(163) Polanyi, J. C. Some concepts in reaction dynamics. *Science* **1987**, *236*, 680–690.

(164) Polanyi, J. C. Some concepts in reaction dynamics (Nobel lecture). *Angew. Chem.* **1987**, *26*, 952–971.

(165) Kroes, G.-J.; Díaz, C.; Pijper, E.; Olsen, R. A.; Auerbach, D. J. Apparent failure of the Born–Oppenheimer static surface model for vibrational excitation of molecular hydrogen on copper. *Proc. Natl. Acad. Sci.* **2010**, *107*, 20881–20886.

(166) Sun, J.; Ruzsinszky, A.; Perdew, J. P. Strongly constrained and appropriately normed semilocal density functional. *Phys. Rev. Lett.* **2015**, *115*, 036402.

(167) Gerrits, N.; Smeets, E. W. F.; Vuckovic, S.; Powell, A. D.; Doblhoff-Dier, K.; Kroes, G.-J. Density functional theory for molecule–metal surface reactions: When does the generalized gradient approximation get it right, and what to do if it does not. *J. Phys. Chem. Lett,* **2020**, *11*, 10552–10560.

(168) Yin, R.; Zhang, Y.; Libisch, F.; Carter, E. A.; Guo, H.; Jiang, B. Dissociative chemisorption of O_2 on Al(111): dynamics on a correlated wave-function-based potential energy surface. *J. Phys. Chem. Lett.* **2018**, *9*, 3271–3277.

(169) Gostein, M.; Parhikhteh, H.; Sitz, G. Survival probability of H_2 (ν= 1, J= 1) scattered from Cu(110). *Phys. Rev. Lett.* **1995**, *75*, 342.

(170) Watts, E.; Sitz, G. O. State-to-state scattering in a reactive system: H_2 (v= 1, j= 1) from Cu(100). *J. Chem. Phys.* **2001**, *114*, 4171–4179.

(171) Kroes, G.-J.; Wiesenekker, G.; Baerends, E.; Mowrey, R. Competition between vibrational excitation and dissociation in collisions of H_2 with Cu(100). *Phys. Rev. B* **1996**, *53*, 10397.

(172) Salin, A. Theoretical study of hydrogen dissociative adsorption on the Cu(110) surface. *J. Chem. Phys.* **2006**, *124*, 104704.

(173) Olsen, R.; Kroes, G.; Baerends, E. Atomic and molecular hydrogen interacting with Pt(111). *J. Chem. Phys.* **1999**, *111*, 11155–11163.

(174) Olsen, R.; Philipsen, P.; Baerends, E. CO on Pt(111): A puzzle revisited. *J. Chem. Phys.* **2003**, *119*, 4522–4528.

(175) Mills, G.; Schenter, G.; Makarov, D. E.; Jónsson, H. Generalized path integral based quantum transition state theory. *Chem. Phys. Lett.* **1997**, *278*, 91–96.

(176) Mills, G.; Jónsson, H.; Schenter, G. K. Reversible work transition state theory: application to dissociative adsorption of hydrogen. *Surf. Sci.* **1995**, *324*, 305–337.

(177) Mills, G.; Jónsson, H. Quantum and thermal effects in H_2 dissociative adsorption: evaluation of free energy barriers in multidimensional quantum systems. *Phys. Rev. Lett.* **1994**, *72*, 1124.

(178) Somers, M.; Kingma, S.; Pijper, E.; Kroes, G.; Lemoine, D. Six-dimensional quantum dynamics of scattering of ($\nu = 0$, j= 0) H_2 and D_2 from Cu(111): test of two LEPS potential energy surfaces. *Chem. Phys. Lett.* **2002**, *360*, 390–399.